THESIS FOR THE DEGREE OF DOCTOR OF PHILOSOPHY

Design and Verification of High Power Density Electrically Excited Synchronous Machine for Traction Applications.

Luca Boscaglia

Department of Electrical Engineering
Chalmers University of Technology
Gothenburg, Sweden, 2025

Design and Verification of High Power Density Electrically Excited Synchronous Machine for Traction Applications.

Luca Boscaglia
ISBN: 978-91-8103-156-0
Doktorsavhandlingar vid Chalmers tekniska högskola.
Ny series nr 5614

ISSN3.1415-9265
Department of Electrical Engineering

Chalmers University of Technology
SE-412 96 Gothenburg, Sweden
www.chalmers.se

Printed by Chalmers Reproservice
Gothenburg, Sweden, February2025

"Let your joy be in your journey, not in some distant goal." – Tim Cook

Design and Verification of High Power Density Electrically Excited Synchronous Machine for Traction Applications.

Luca Boscaglia

Department of Electrical Engineering
Division of Electrical Power Engineering

Abstract

The transportation sector accounts for 28% of U.S. greenhouse gas emissions and 16% globally, with electric drivetrains playing a crucial role in achieving climate goals. However, the shift to electric vehicles (EVs) has heightened demand for rare-earth magnets, raising environmental and geopolitical concerns. Electrically Excited Synchronous Machines (EESMs) offer a compelling alternative to Permanent Magnet Synchronous Machines (PMSMs) by eliminating rare-earth materials while delivering high starting torque, improved power factor, and effective field weakening for greater efficiency across broader speed ranges.

Designing EESMs involves significant challenges due to active conductors in the rotor, which complicate mechanical design under high centrifugal forces and demand efficient thermal management. The high power density required for DC field generation generates substantial heat, making innovative cooling solutions essential to address mechanical losses and rotor cooling complexities.

This thesis tackles the electromagnetic, mechanical, and thermal design challenges of EESMs for vehicle and truck drivetrain. A 60 kW concept machine is designed and prototyped, and its electromagnetic and mechanical design is validated through experimental testing. Following validation, the design scales up to a 200 kW prototype for trucks, focusing on direct oil cooling for the rotor and stator, and exploring oil splashing limitations. Experimental testing demonstrates the cooling system ability to maintain uniform temperature distribution, keeping components within the insulation class limits for reliable operation in the continuous operating region. These advancements position EESMs as viable solutions for EV applications, addressing critical performance and sustainability challenges.

Keywords: Electric Motors, Electrically Excited Synchronous Machine (EESM), Emotors, Oil Cooling, Wound Field Synchronous Machine (WFSM).

Acknowledgments

Completing this PhD thesis has been one of the most challenging and rewarding experiences of my life. I would like to take this opportunity to express my heartfelt gratitude to the individuals and institutions that have supported and inspired me throughout this journey.

First and foremost, I would like to thank my advisor, Yujing Liu. I am deeply grateful for your friendship, guidance, and for making me feel home from the very first moment we met in Sweden. Your mentorship has been invaluable, not only in helping me navigate the complexities of this research but also in shaping me as a researcher and professional.

I am immensely thankful to all my colleagues and collaborators at our division. A special thanks goes to my former co-supervisor Nimananda, who has also become a cherished friend, and to Junfei, whose guidance has been invaluable. My heartfelt appreciation extends to Daniel and Tati, whose companionship brightened every day, and thank you Bowen for sharing those countless nights and weekends at the office in Chalmers. A big thanks to Artem for hunting down typos in this thesis — I am sure a few still escaped.

To Ale, my second brother, your unwavering support from Italy always means the world to me. And to Jamie, thank you for believing in me, especially during moments when I doubted myself.

To my big extended family, which keeps growing bigger and bigger. To my mum, my brother, and my two sisters—you have always been my strongest foundation. As I often say, you are the best life companions I could ever have hoped for, and I am endlessly grateful for your love and unwavering support.

This thesis is dedicated to all those who dare to dream and work tirelessly to bring those dreams to life. To those who pour their hearts and souls into their aspirations, I stand with you—may we all continue to pursue our passions with courage and determination.

Acronyms

AC:	Alternating Current
CFD:	Computational Fluid Dynamics
CHT:	Conjugate Heat Transfer
DC:	Direct Current
EESM:	Electrically Excited Synchronous Motor
EM:	Electromagnetic
EMF:	Electro-Motive Force
EV:	Electric Vehicle
F:	Force
FEA:	Finite Element Analysis
FEM:	Finite Element Method
FVM:	Finite Volume Method
HTC:	Heat Transfer Coefficient
IM:	Induction Motor
L:	Inductance
MPS:	Moving Particle Semi-implicit Method
MTPA:	Maximum Torque Per Ampere
P:	Power
PF:	Power Factor
PMSM:	Permanent Magnet Synchronous Motor
P_{Cu}:	Copper Loss

P_{Fe}:	Iron Loss
R:	Resistance
RE:	Rare Earth (Magnets)
T:	Torque
v:	Velocity
$_d$:	Subscript for d-axis
$_q$:	Subscript for q-axis
$_{Cu}$:	Subscript for Copper
$_{Fe}$:	Subscript for Iron
η:	Efficiency
ρ:	Resistivity

Contents

CHAPTER 1

Introduction

1.1 Background

Global efforts to combat climate change depend on a decisive shift away from fossil fuels. Achieving this will require the widespread electrification of transportation, primarily by replacing combustion engine vehicles with electric drive trains.

Transportation is a significant contributor to global greenhouse gas (GHG) emissions. According to the U.S. Environmental Protection Agency (EPA) [1], the transportation sector accounted for 28% of total U.S. GHG emissions in 2022, making it the largest contributor among all sectors. In accordance with the European Environment Agency (EEA), the transport sector accounted for approximately 29% of the European Union's GHG emissions in the same year [2]. Globally, the transportation sector produced approximately 8.4 billion metric tons of carbon dioxide equivalent ($GtCO_2e$) in 2023, representing about 16% of total GHG emissions. This positions transportation as the second largest source of emissions worldwide [3].

The transition to electrified transportation is then necessary and this is reflected in the Energy Technology Perspective report of the International

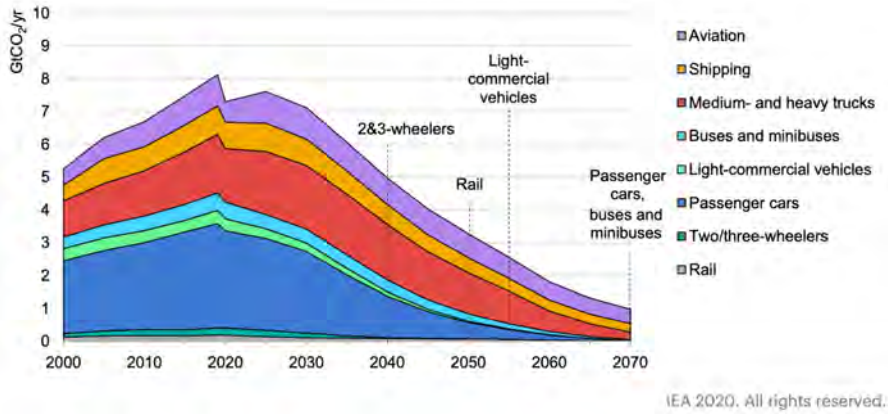

Figure 1.1: Global CO_2 emissions in transport by mode in the Sustainable Development Scenario, 2000-70. Dotted lines indicate the year in which various transport modes have largely stopped consuming fossil fuels and hence no longer contribute to direct emissions of CO_2 from fossil fuel combustion.

Energy Agency (IEA) [4], which describes its *Sustainable Development Scenario* goal of reaching net zero CO_2 emissions from global energy by 2070. The visualization in Fig. 1.1 shows the pathways for the different elements of the transport sector in this optimistic scenario. It can be seen that several sub-sectors are projected to achieve decarbonization within the coming decades through the adoption of electrification and hydrogen technologies. In the IEA's scenario, emissions from motorcycles are expected to be phased out by 2040, rail by 2050, and small trucks by 2060. However, emissions from cars and buses are anticipated to persist until at least 2070 before being fully eliminated.

This monumental transition will inevitably lead to a much higher demand for electric traction motors, nearly all of which rely on magnets containing rare earth elements.

The extraction and processing of rare earth elements (REEs) are associated with significant environmental harm due to several factors:

- Mining and Radioactive Waste: REE ores often contain radioactive elements like thorium and uranium. Extracting these elements generates

substantial waste, including radioactive materials. For instance, securing just one ton of rare earth elements produces 2,000 tons of toxic waste, devastating large regions of China [5].

- Chemical Processing and Toxic Byproducts: The separation of REEs from mined ore requires extensive chemical processing, involving strong acids that can leach into the environment. This process results in the acidification of aquatic environments and contamination of soil and water sources [6]. Significative is the Myanmar case study, in Kachin State, where heavy rare earth mining has led to severe environmental degradation. The use of chemicals such as oxalic acid in mining processes has resulted in high levels of arsenic in rivers, the destruction of biodiversity, and health issues among local populations [7].

- Greenhouse Gas Emissions: The energy-intensive nature of REE processing contributes to significant greenhouse gas emissions. For example, the production of neodymium magnets, essential for electric vehicle motors, involves processes that emit considerable amounts of CO_2 [8].

These environmental impacts highlight the urgent need for sustainable practices in rare earth element extraction and processing to reduce their harmful effects on ecosystems and human health.

A critical issue is the dominance of China in the rare earth magnet market. China controls about 90% of global REE processing capacity [9]–[11], posing significant risks for automakers outside of China, especially in the electric vehicle industry, which relies heavily on rare earth magnets. According to a 2023 U.S. Geological Survey report [12], China accounts for 63% of global mining output and for 95% of refining and processing.

The International Energy Agency [13] also warned of the risks from this dependency in its 2021 report, noting that China held 90% of global REE processing capacity in 2019. The IEA projects that demand for rare earth magnets in EVs will quadruple by 2040, exacerbating supply chain vulnerabilities if alternative sources are not developed. This concentration, shown by Statista [14] in Fig. 1.2, leaves automakers vulnerable to export restrictions, geopolitical tensions, and price volatility.

In 2010, China reduced its export quotas on rare earth elements (REEs) by 40%, citing the need for resource conservation and environmental protection. This substantial reduction in supply triggered a sharp surge in prices

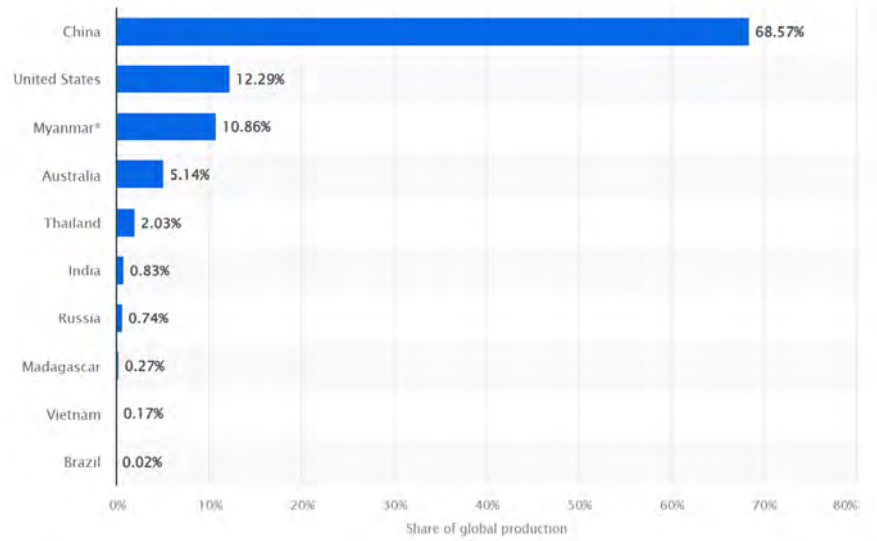

Figure 1.2: Distribution of rare earths production worldwide as of 2023, by country

and widespread disruptions across supply chains. For instance, the price of neodymium oxide soared from around $25 per kilogram in early 2010 to a peak of $340 per kilogram by July 2011, as illustrated by Statista in Fig. 1.3 [15].

In response, extensive initiatives are underway to design and develop advanced motors that either eliminate or significantly reduce the use of rare earth elements.

Government agencies, corporations, and universities across nearly all industrialized nations are tackling this challenge, often through collaborative efforts. In the United States, long-standing projects in national laboratories aim to create permanent magnets and motor designs without rare-earth materials. Additionally, a partnership announced on November 2023 between General Motors, Stellantis, and the startup Niron Magnetics focuses on developing EV motors based on Niron rare earth-free permanent magnets [16]. On March 2023, Tesla announced that its *next drive unit* would utilize a permanent magnet without any rare earth elements [17]. Meanwhile, in Europe, a consortium called *Passenger*, which includes 20 partners from both industry

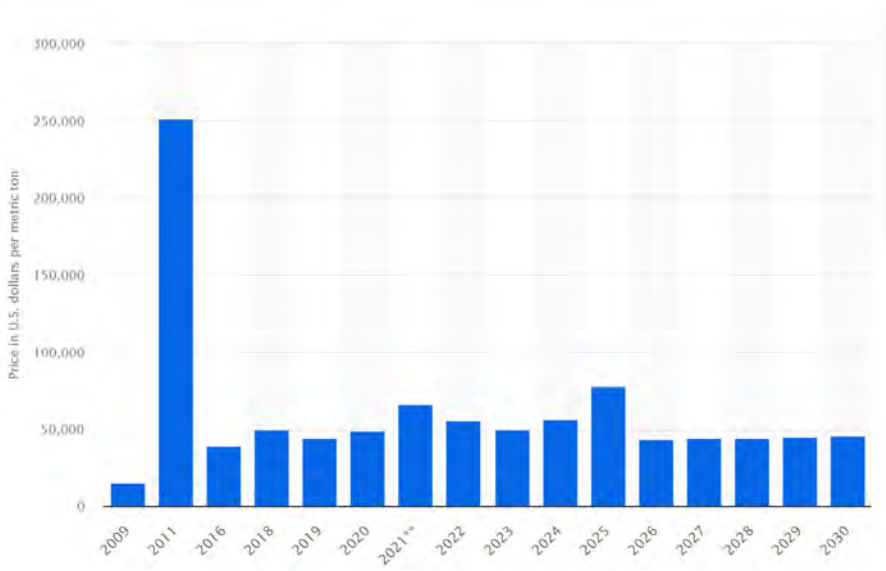

Figure 1.3: Neodymium oxide price worldwide from 2009 to 2020 with a forecast for 2021 to 2030

and academia, is working on rare earth-free permanent magnets for EVs [18].

To reduce or eliminate the use of rare earth materials in electric motors, several approaches can be explored, involving either the substitution of permanent magnets with alternative magnetic materials or the adoption of different motor topologies that do not rely on rare earth elements. Rare earth magnets, such as Neodymium-based magnets, are commonly used in PMSMs due to their high magnetic strength, which results in compact and efficient motor designs. However, the scarcity, high cost, and environmental impact of mining these materials have prompted the development of alternative solutions.

One approach is to replace rare earth magnets with other types of magnets like ferrite, Alnico, or Samarium Cobalt (SmCo). Ferrite magnets are a cost-effective and abundant option made from iron oxide. They offer good thermal stability and natural resistance to corrosion but suffer from lower magnetic strength. As a result, motors using ferrite magnets tend to be larger and less efficient, which can be a drawback for applications demanding high power density. Alnico magnets, made from aluminum, nickel, and cobalt, have ex-

cellent temperature stability and are resistant to demagnetization. However, they also exhibit weaker magnetic properties compared to rare earth magnets and may be expensive due to the use of cobalt. Samarium Cobalt (SmCo) magnets provide a middle ground, offering high magnetic strength and superior thermal stability, making them suitable for high-temperature applications. Despite these advantages, SmCo magnets are costly and brittle, posing challenges in manufacturing and handling.

In addition to exploring alternative magnet materials, motor designs that do not rely on permanent magnets are gaining traction, as shown in Table 1.1.

Table 1.1: Comparison of Alternative Motor Technologies to Reduce Rare Earth Usage

Technology	Advantages	Disadvantages
Fe Motor	Low cost, corrosion resistant	Lower magnetic strength, larger size
AlNiCo Motor	High temperature stability	Weaker magnetic strength, costly
SmCo Motor	High magnetic strength, good thermal stability	Expensive, brittle
Reluctance Motor	No magnets, simple and robust design	Torque ripple, complex control requirements, low power factor
Induction Motor	No magnets, mature and cost-effective technology	Lower efficiency, significant rotor heat generation
EESM	No magnets, dynamic field control	Complex rotor design, additional power losses, excitation system

Reluctance motors, such as switched reluctance motors and synchronous reluctance motors, operate based on the principle of magnetic reluctance, entirely avoiding the need for permanent magnets. These motors are robust, simple in construction, and cost-effective. However, they can suffer from torque ripple and lower efficiency and power factor, and their control systems tend to be more complex due to the need for precise torque management.

Induction motors represent another well-established alternative that avoids rare earth elements. Instead of using permanent magnets, induction motors rely on electromagnetic induction to generate torque. This technology is mature and widely used across various industries due to its simplicity and cost-effectiveness. However, induction motors generally have lower efficiency and power density compared to PMSMs, especially at low speeds. Additionally, they generate more heat in the rotor, which can necessitate extra cooling mechanisms.

Electrically Excited Synchronous Motors (EESM) offer a different approach by using an electromagnet in the rotor instead of permanent magnets. This

design allows for dynamic control of the magnetic field through the excitation current, providing flexibility in motor operation. EESMs can achieve high efficiency and eliminate the need for rare earth materials. Nevertheless, the use of field windings requires additional components like slip rings and brushes or a contactless excitation system, which introduces mechanical complexity. Moreover, the excitation current contributes to additional losses, which can affect the overall efficiency, particularly at higher speeds.

Examining the current state-of-the-art motor technologies used by leading automotive brands in Table 1.2, it can be observed that Permanent Magnet Synchronous Motors (PMSMs) still dominate the electric vehicle market, with most major brands opting for this motor type due to its high efficiency, compact size, and strong performance capabilities. Tesla, BMW, GM, Ford, Hyundai, Nissan, Audi, Jaguar, Volkswagen, Volvo, Porsche, Lucid Motors, and BYD all primarily utilize PMSMs in their electric drivetrains.

Nonetheless, there is a growing interest in alternative motor technologies aimed at reducing reliance on rare-earth materials. High-performance brands such as Lamborghini, Ferrari, and McLaren have incorporated axial-flux motors, which offer high power density and a compact design. However, axial-flux motors still depend on permanent magnets, limiting their ability to fully address sustainability concerns. Tesla has also explored induction motors and reluctance-based designs, while BMW has been developing EESMs as magnet-free alternatives.

Research Question

The Electrically Excited Synchronous Machine offers several advantages, particularly in applications requiring high efficiency and controllability. Below are the key benefits:

- *No Permanent Magnets:* Cost-effective and free from rare-earth material dependency, avoiding also demagnetization risks.
- *Wide Operating Range:* Flux adjustability allows for high efficiency over a broad speed range, making EESMs well-suited for variable-speed drives
- *Improved Power Factor:* The field current can be adjusted to achieve near-unity power factor, reducing reactive power demand and improving system efficiency.

Table 1.2: Summary of Electric Motors Used by Automotive Brands

Brand	Type of Motor(s)	References
Tesla	IM, PMSM, Reluctance Motor	[19]
BMW	PMSM, EESM	[20]
General Motors	PMSM	[21]
Mercedes-Benz	Axial-Flux Motor	[22]
Rivian	PMSM	[23]
Ford	PMSM	[24]
Hyundai	PMSM	[25]
Nissan	PMSM	[26]
Audi	PMSM	[27]
Jaguar	PMSM	[28]
Volkswagen	PMSM	[29]
Volvo	PMSM	[30]
Porsche	PMSM	[31]
Lucid Motors	PMSM	[32]
BYD	PMSM	[33]
Lamborghini	PMSM, Axial-Flux Motor	[34]
Ferrari	PMSM, Axial-Flux Motor	[35]
McLaren	PMSM, Axial-Flux Motor	[36]

- *High Power Density:* adjusting the field current the achieved power can be temporarily increased within the thermal limits imposed by the cooling system performance.
- *High Torque at Low Speeds:* Efficient field control enables high torque at low speeds.
- *Field Current Controllability:* The field current in the rotor can be dynamically controlled, allowing the machine to operate at optimal flux levels, improving the machine control for varying dynamic conditions.

Despite its advantages, the design of EESMs presents significant challenges across electromagnetic, mechanical, and thermal domains, primarily due to the integration of active conductors in the rotor. Focusing solely on the machine design aspects and excluding the excitation system and control considerations, the primary challenges from a design perspective are:

- *Electromagnetic Design Challenges.* Electromagnetic design in EESMs is strongly influenced and constrained by mechanical and thermal considerations. Achieving high electromagnetic performance often requires compromises in material selection, geometry, and winding layout to ensure mechanical integrity and manage thermal stresses. For example,

maximizing the rotor winding filling factor for improved flux density is limited by the need to withstand centrifugal forces and maintain insulation durability at elevated temperatures. Similarly, the choice of core materials with high magnetic permeability must balance mechanical strength and low thermal expansion to ensure reliable operation under high-speed and high-temperature conditions. Thus, electromagnetic design cannot be optimized in isolation and must be integrated with mechanical and thermal design requirements.

- *Mechanical Design Challenges.* Mechanical challenges in EESM design arise from the need to balance several conflicting requirements. First, rotor laminations must combine high magnetic permeability, mechanical strength, and low core losses, which can be difficult to achieve simultaneously. Second, the design must enable the proper placement of conductors in the rotor while maintaining structural integrity under the significant centrifugal forces generated during high-speed operation. These forces can cause displacement or deformation, necessitating a rotor structure that not only withstands these stresses but also maximizes the winding filling factor for optimal electromagnetic performance.

- *Thermal Design and Cooling Challenges.* Active rotor windings in EESMs generate significant heat due to I^2R losses, and the absence of direct external cooling poses a substantial thermal challenge. Elevated rotor temperatures can degrade the insulation system, reducing its longevity and impacting electrical performance. Designing an effective cooling system for a rotating rotor is particularly difficult, as it requires innovative solutions to manage heat dissipation while accounting for the dynamic nature of the rotor. This necessitates advanced thermal modeling and the development of efficient, robust cooling mechanisms such as integrated liquid channels, spray cooling systems, or optimized airflow paths.

Research Contribution and Thesis Outline

This thesis addresses the challenges associated with the electromagnetic, mechanical, thermal and cooling design of Electrically Excited Synchronous Machines, as well as their integration into traction drivetrains for vehicles and trucks.

In **Chapter 2**, a preliminary investigation is conducted using only simulations to evaluate the potential advantages of EESMs compared to PMSMs in a truck drivetrain. For this purpose, a generic 200 kW EESM is designed and simulated under steady-state conditions and during a driving cycle. The results are compared to those of a PMSM with an identical stator, differing only in the rotor design.

In **Chapter 3**, a 60 kW EESM is designed, analyzed, and prototyped as a scaled-down concept machine to evaluate the feasibility of deploying this motor type in the intended applications. The primary objective of this design is to focus on the electromagnetic performance, optimizing the machine parameters and validating the accuracy of electromagnetic models and simulations through experimental testing. Additionally, the study addresses the feasibility and manufacturability of the dovetail technology used in the machine construction. Comprehensive thermal analyses are also conducted on the concept machine, investigating its thermal behavior under both steady-state and transient operating conditions to ensure reliability and performance.

Once the 60 kW machine model is validated, **Chapter 4** introduces the full-size 200 kW EESM. The emphasis for this larger-scale machine is on addressing the thermal challenges associated with high-power-density EESMs. Specifically, the chapter focuses on the design and optimization of cooling strategies, with particular attention to rotor cooling. Detailed thermal analyses are performed to investigate and evaluate cooling techniques for the rotor, stator, and the effects of splashing mechanisms, ensuring effective heat dissipation and reliable performance under demanding operating conditions.

1.2 List of Publications

List of included publications:

1. G. Mademlis, Y. Liu, J. Tang, L. Boscaglia and N. Sharma, "Performance Evaluation of Electrically Excited Synchronous Machine compared to PMSM for High-Power Traction Drives," *2020 International Conference on Electrical Machines (ICEM)*, Gothenburg, Sweden, 2020, pp. 1793-1799, doi: 10.1109/ICEM49940.2020.9270852.

2. L. Boscaglia, N. Sharma, Y. Liu and G. Mademlis, "Balancing Peak-torque and Drive-cycle Efficiency with Magnet Dimensioning of Perma-

nent Magnet Synchronous Machines," *IECON 2020 The 46th Annual Conference of the IEEE Industrial Electronics Society*, Singapore, 2020, pp. 883-888, doi: 10.1109/IECON43393.2020.9255349.

3. L. Boscaglia, Y. Liu, H. Avsar, J. Tang and M. Galbiati, "Convective Heat Transfer Coefficients and Mechanical Loss Evaluation of Oil Splashing in Direct Cooled Electrically Excited Hairpin Motors," *2022 International Conference on Electrical Machines (ICEM)*, Valencia, Spain, 2022, pp. 496-503, doi: 10.1109/ICEM51905.2022.9910756.

4. L. Boscaglia, D. Chiappini, N. Sharma, Y. Liu, J. Tang and B. Jiang, "Thermal Modeling and Driving-cycle Critical Temperatures Estimation of Electrically Excited Synchronous Machine for Automotive Traction," *IEEE Energy Conversion Conference and Expo (ECCE)*, Nashville, USA, 2023.

5. L. Boscaglia, H. S. N. Sugumar, N. Sharma and Y. Liu, "Design and Verification of an Electrically Excited Synchronous Machine Rotor with Direct Oil Cooling for Truck Applications," *IEEE Transactions on Transportation Electrification*, doi: 10.1109/TTE.2024.3389506.

6. H. Chen, J. Tang, Y. Liu, B. Jiang and L. Boscaglia, "Electromagnetic Performance Investigation of A Brushless Electrically-Excited Synchronous Machine for
Long-Distance Heavy-Duty Electric Vehicles," *IEEE Transactions on Transportation Electrification*, doi: 10.1109/TTE.2024.3388430.

7. L. Boscaglia, H. S. N. Sugumar and Y. Liu, "Design and Verification of a Direct-Cooled Hairpins Stator with Oil Jacket and End Winding Self-Impingement." *IEEE Transactions on Transportation Electrification* (SUBMITTED).

Further author's contributions:

8. R. Liu, J. Tang, L. Boscaglia, B. Jiang, N. Sharma and Y. Liu, "Impacts of Stator Current Angle and Rotor Current on Solid Losses of Hairpin Windings in Traction Electrically Excited Synchronous Machines," *2024 International Conference on Electrical Machines (ICEM)*, Torino, Italy, 2024, pp. 1-7, doi: 10.1109/ICEM60801.2024.10700199.

9. J. Tang, B. Jiang, L. Boscaglia, H. Chen and Y. Liu, "Observations of Field Current and Field Winding Temperature in Electrically Excited Synchronous Machines with Brushless Excitation," *2022 International Conference on Electrical Machines (ICEM)*, Valencia, Spain, 2022, pp. 841-847, doi: 10.1109/ICEM51905.2022.9910595.

10. J. Tang, B. Jiang, L. Boscaglia, H. Chen, Y. Liu and S. Lundberg, "Comprehensive Dynamic Current Control of Electrically Excited Synchronous Machines With Magnetic Mutual Couplings," *IEEE Transactions on Industrial Electronics*, vol. 71, no. 11, pp. 13855-13866, Nov. 2024, doi: 10.1109/TIE.2024.3368104.

11. J. Tang, B. Jiang, L. Boscaglia, R. Liu, S. Lundberg and Y. Liu, "High-Frequency Brushless Excitation with Bi-Directional Power Flow for Electrically Excited Synchronous Machines,"
2024 International Conference on Electrical Machines (ICEM), Torino, Italy, 2024, pp. 1-7,
doi: 10.1109/ICEM60801.2024.10700252.

12. B. Jiang, J. Tang, Y. Liu and L. Boscaglia, "Active Balancing of Reconfigurable Batteries Using Reinforcement Learning Algorithms,"
2023 IEEE Transportation Electrification Conference & Expo (ITEC), Detroit, MI, USA, 2023, pp. 1-6,
doi: 10.1109/ITEC55900.2023.10187076.

CHAPTER 2

Preliminary Performance Comparison of EESM and PMSM Drivetrains for Truck Applications

The electric drive design for heavy-duty vehicles is challenging due to special requirements involved, such as high starting torque and operation at the peak power for a long time. The electrically excited synchronous machine is a suitable machine type for such application and a potential alternative to the permanent magnet synchronous machines due to the superior flexibility that the rotor excitation offers. The direct adjustment of the flux allows also to tune the best efficiency region of the machine close to the usual operating points of the vehicle achieving at the same time a better power factor compared to a PMSM, which can further increase the efficiency and the power capability of the stator inverter. A case study is presented comparing a drive system based on an Electrically Excited Synchronous Machine and one based on a Permanent Magnet Synchronous Machine for electric trucks. The two machines share an identical stator, and their rotors are designed to produce the same magnetomotive force (MMF) to ensure a fair comparison. Simulations of the entire vehicle drivetrain, conducted using the Finite Element Method and MATLAB over a representative driving cycle, highlight the advantages of the EESM for truck applications under the specified conditions.

2.1 Modelled Vehicle Drivetrain

The electric drive developed in this study has been designed to fit the specifications of a test-case electric truck, whose parameters are summarized in Table 2.1. The parameters of the vehicle model and the dimensions of the vehicle are referenced from [37], [38]. The rotating inertia of the truck converted to the machine side of the gearbox is equal to $J_{tr} = mr^2/\text{ gear }^2 = 27.89\text{ kg m}^2$. The operation requirements for the designed drive are listed in Table 2.1, which summarizes the most common operating conditions of a truck. Firstly, the *Start-up* condition of the drive require a high peak torque in order to be able to accelerate the vehicle from standstill while being on a road with slope. The *High Power Operation* corresponds to driving on an uphill road and the *Best Efficiency Operation* is the high-speed driving condition on a highway, which is the most common for long-haul trucks.

The forces that are applied on the vehicle and its motion are described by the following equations where the acceleration force of the truck is defined as below [38]:

Table 2.1: Technical Specifications of the Modeled Vehicle

Parameter	**Value**	**Unit**
Vehicle mass m	40	metric tonnes
Effective vehicle front area A	8.34	m^2
Air density ρ_{air}	1.2	kg/m^3
Aerodynamic drag coefficient C_d	0.53	-
Rolling resistance coefficient C_r	0.0051	-
Tire size	295/75 R 22.5	-
Wheel radius r	0.5	m
Gear ratio *gear*	19	-
Transmission system efficiency η_{gear}	0.94	-
Electric motor arrangement	2 motors	-
Maximum power of each motor P_{max}	250	kW
Maximum speed v_{max}	100	km/h

Table 2.2: Truck Electric Drive Operation Requirements (for a 2-Motor Drivetrain)

Parameter	Value	Unit
(1) Start-up Operation with Peak Torque		
Duration	5	min
Road slope	12	%
(2) High Power Operation		
Duration	20	min
Power	400	kW
Road slope	6	%
Vehicle speed	50	km/h
(3) Best Efficiency Operation		
Duration	long time	-
Power	100	kW
Road slope	0	%
Vehicle speed	80	km/h

$$F_{\text{acc}} = \frac{T_{\text{motor}}}{r} gear\ \eta_{\text{gear}} - F_{\text{road load}}$$

where $F_{\text{road load}}$ is the load of the wheels. The $F_{\text{road load}}$ consists of the air drag F_{air} , the rolling resistance F_{roll} and the grading force of the road F_{grade} . These are described as:

$$\begin{aligned} F_{\text{air}} &= \frac{1}{2}\rho_{air} C_d A \left(v_{tr} - v_{wind}\right)^2 \\ F_{\text{roll}} &= C_r mg\cos(\alpha) \\ F_{\text{grade}} &= mg\sin(\alpha) \end{aligned}$$

where v_{tr} and v_{wind} are the forward speed of the vehicle and of the wind respectively, $\alpha = \tan^{-1}(\text{ slope })$ is the road angle of inclination. For this study $v_{\text{wind}} = 0$ m/s has been considered. The load torque applied on the motor is calculated as:

$$T_{\text{load}} = \frac{r}{gear} F_{\text{road load}}$$

Two identical electric drives are needed to meet the operating requirements of the electric truck in Table 2.2. Therefore, the load torque applied on each machine is equal to $0.5T_{\text{load}}$, as shown in Fig. 2.1 (a).

Two types of electric drive with the same parameters, one with EESM and one with PMSM, have been designed and compared. The operation of the

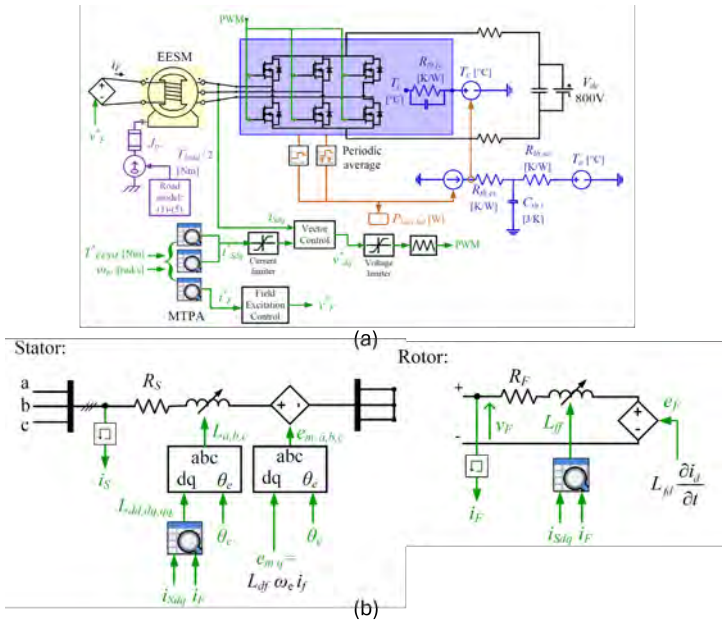

Figure 2.1: Schematic of the (a)EESM drive including the simplified thermal network model of the inverter and the loss calculation blocks and (b) the electric model of the look-up-table-based EESM

machine drive is modelled on Matlab/PLECS and the schematic diagram of the EESM drive is shown in Fig. 2.1 (a). The losses of the three-phase stator inverter are modelled by importing the loss model of the semiconductors, as provided by their manufacturer. The SiC power modules CAB450M12XM3 have been used in this application that have maximum AC current of 450 A peak and maximum blocking voltage of 1.2 kV. The same stator inverter is used also for the PMSM drive in order to have a fair performance comparison of the two machine types. More details regarding the design parameters of the inverter and its control are shown in Table 2.3.

Hysteresis control is used for the field excitation current regulation of the EESM. The schematic diagram of the rotorside converter with the high-frequency transformer for the wireless energy transfer is not included in this figure, but instead it is represented by a voltage-controlled source that pro-

Table 2.3: Stator Inverter Parameters

Parameter	Value	Unit
Nominal DC-link voltage V_{dc}	800	V
DC-link capacitance C_{dc}	480	μF
Maximum AC current (peak) $I_{S,\max}$	450	A
Switching frequency f_{sw}	10	kHz
External gate resistance R_G	1	Ω
Current controller bandwidth α_I	1000	rad/s
Inlet coolant temperature T_a	65	°C
Case-sink thermal resistance $R_{\mathrm{th,cs}}$	0.0043	K/W
Sink-coolant thermal resistance $R_{\mathrm{th,sa}}$	0.0073	K/W
Heatsink thermal capacitance C_{ths}	1238	J/K

duces the rotor voltage v_F.

A lumped-parameter thermal model of the stator inverter shown in Fig. 2.1 (a) is used for modelling the thermal performance of the SiC power modules and their liquid-cooled heatsink, in order to simulate more accurately the semiconductor losses and temperature. The combined Cauer and Foster network proposed in [39] is used and the thermal resistances and heatsink capacitance are reported in Table 2.3, which have been estimated through computational-fluid-dynamics (CFD) simulations of a real inverter heatsink.

A look-up-table-based model of both the EESM and the PMSM is used on PLECS where simulation results from the FEM analysis shown in the next section are utilized. Specifically for the EESM, the map of the flux linkages is imported as a function of the d- and q -axis stator currents i_{Sdq} and of the excitation current i_F. The inductance matrix of the machine is calculated as

$$\begin{bmatrix} L_{dd} & L_{dq} & L_{df} \\ L_{qd} & L_{qq} & L_{qf} \\ L_{fd} & L_{fq} & L_{ff} \end{bmatrix} = \nabla \begin{bmatrix} \psi_d\left(i_d, i_q, i_F\right) \\ \psi_q\left(i_d, i_q, i_F\right) \\ \psi_f\left(i_d, i_q, i_F\right) \end{bmatrix}$$

and the produced electromagnetic torque is equal to

$$T_{EESM} = \frac{3}{2} p \left(\psi_d i_q - \psi_q i_d\right)$$

The electric model of the EESM with the 3D look-up-tables of the stator and rotor inductances is shown in Fig. 2.1 (b). A similar look-up-table based simulation model is also used for the PMSM.

The stator inverter is controlled in torque control mode and the gains of the

current controller are dimensioned based on the Loop Shaping method. The current reference signals for the current controller are calculated through pre-calculated look-up-tables that have as input the machine torque and speed. These look-up-tables are derived by applying total copper loss (stator and rotor) minimization for the EESM [40] and stator copper loss minimization for the PMSM. The maximum speed of the specific machines is $n_{\max} = 10000$rpm and, therefore, the maximum speed in km/h that the vehicle can attain is approximately equal to $v_{\max} = 100$ km/h.

2.2 Machine Design for Comparative analysis

For the purpose of this study two electric machine models have been developed on Ansys Maxwell, a PMSM and an EESM.

Since the aim of the study is to compare the performance and efficiency of the two machines, the outer dimensions and the the stator geometry of both designs are kept as close as possible, as shown in Table 2.4. The stator slot area of both machines is determined by the slot copper area, fill factor and stator current density. The slot copper area is further decided by stator current, number of turns and number of parallel branches. A parametric sweep of these parameters is applied and the optimum values are then chosen for both machines, as seen in Table 2.4. The machine models have also been optimized by adjusting design dimensions, such the airgap diameter, stator slot width, stator slot height, rotor slot width and height. The target of both designs is to achieve peak torque of 800 Nm , while minimizing the iron core losses and the copper losses.

An important design constraint for the EESM is the sizing of the rotor excitation, in order to respect the specifications in terms of maximum produced torque and the inverter voltage limit. A fair comparison between the two machines should provide also the same magnetomotive force (MMF) produced by the rotor of the two machine types. To have the same amount of MMF from each pole in the EESM, the field windings under each pole are series-connected and the current properly dimensioned. To guarantee unity power factor at high speed operation range, the field MMF should be comparavle to the stator MMF within each pole pair. In this case 2120 A-turn is decided for each pole, which means totally 4240 A-turn flow through each rotor slot, since two coil sides are placed in each rotor slot. With 1 mm diameter wire

Table 2.4: Machine Design Parameters

Parameter	PMSM	EESM	Unit
Outer diameter of housing	300	300	mm
Length of housing	600	600	mm
Outer diameter of lamination OD_{stator}	270	270	mm
Shaft diameter ID_{rotor}	50	50	mm
Stack length L_{stack}	360	360	mm
Number of phases	3	3	-
Number of pole pairs p	4	4	-
Number of slots per pole per phase q	2	2	-
Number of layers r	2	2	-
Pole pitch τ	6	6	-
Coil pitch y	5	5	-
Number of stator slots Q	48	48	-
Stator: number of turns / parallel branches	5/4	5/4	-
Rotor winding number of turns	-	270	-
Winding factor k_w	0.933	0.933	-
Air-gap thickness g_{airgap}	1.5	1.5	mm
Stator and rotor fill factor k_{fill}	0.4	0.4	-
Peak power $P_{\text{em,max}}$	250	250	kW
Peak torque $T_{\text{em,max}}$	798	800	Nm
Maximum stator current (peak) $I_{S,\text{max}}$	450	450	A
Maximum field current $I_{f,\text{max}}$	-	7.854	A
Stator resistance (at 100°C) R_S	19.25	19.6	mΩ
Rotor resistance (at 100°C) R_f	-	54.71	Ω
No-load d-axis stator inductance L_{dd}	0.2759	1.3	mH
No-load q-axis stator inductance L_{qq}	0.2809	1.3	mH
No-load mutual inductance L_{df}	-	92.8	mH
No-load d-axis flux linkage ψ_d	0.2604	0	Wb

used and 10 A/mm^2 current density, the number of turns can be decided. Then the rotor slot area is determined by the total copper area and fill factor. Thereafter, a parametric sweep is applied to determine the shape of the rotor slot.

On the other side, the same scope can be achieved with the PMSM through a correct sizing of the permanent magnets. The V-shaped rotor geometry is chosen for the placement of the internal magnets with bridges and air barriers on the magnet sides. The reason of this choice is mainly the better flux weakening characteristic and lower losses compared to the surface-mounted PMSM, thanks to the iron between the airgap and magnets. Following this consideration and optimization studies on magnets dimensions, width of 48 mm and thickness of 6.8 mm are considered to meet the machine specifications. The final design of both machines is shown in Fig. 2.2, where the flux density

distribution is presented at peak torque and speed of 3000 rpm .

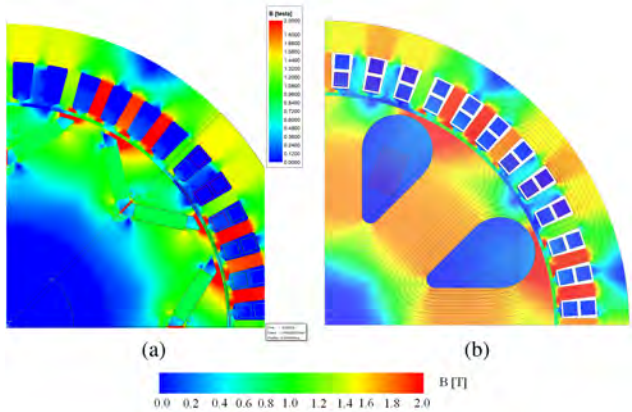

Figure 2.2: Flux density distribution at peak torque and 3000 rpm rotor speed of the PMSM (a) and the EESM(b).

The thermal model of the machines has not been carried out in this study. Therefore, the following rule of thumb has been used for the dimensioning of the current density based on the operating requirements of the modelled electric truck. For the stator windings a current density of 15 A/mm^2 is considered for the peak operation where the machine needs to operate for

maximum 5 minutes, while a current density of 10 A/mm^2 is used for the maximum continuous operation. A maximum current density of 10 A/mm^2 is also used for the rotor windings of the EESM, that corresponds to a maximum field current of 7.854 A. In general, the EESM rotor slots represent a thermal hotspots due to the presence of the DC winding while the PMSM rotor faces much lower temperature stress.

The efficiency of the two machines as a function of the produced electromagnetic torque and speed is shown in Fig 2.3, when total copper loss minimization is applied on the inverter control. The solid outer black line in the figures shows the torque boundary of the machine operating envelope. The mechanical and stray losses of the machines have not been considered for this study, where only the electrical losses are simulated. It can be seen that both machines can produce similar peak torque; however, their efficiency differs a lot with the PMSM having its highest efficiency close to its base speed while

the EESM has the highest efficiency at higher speed. This can be explained by the better power factor of the EESM in the high speed region, as shown also in Fig. 2.4. The higher efficiency of the EESM in the high-speed region will be proven beneficial for the operation of the electric truck, as will be verified with the simulation results in the following section.

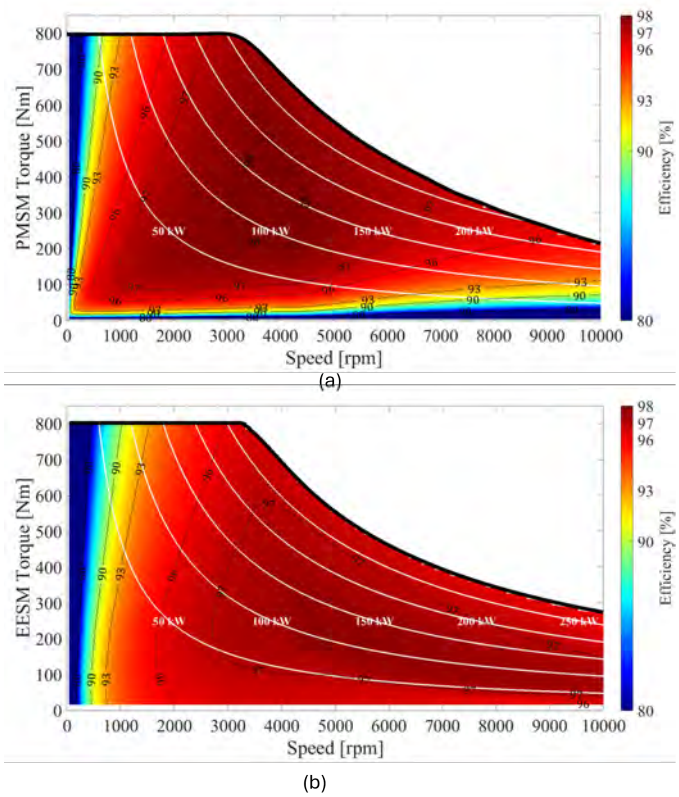

Figure 2.3: Efficiency contours along the torque-speed maps of PMSM (a) and EESM (b).

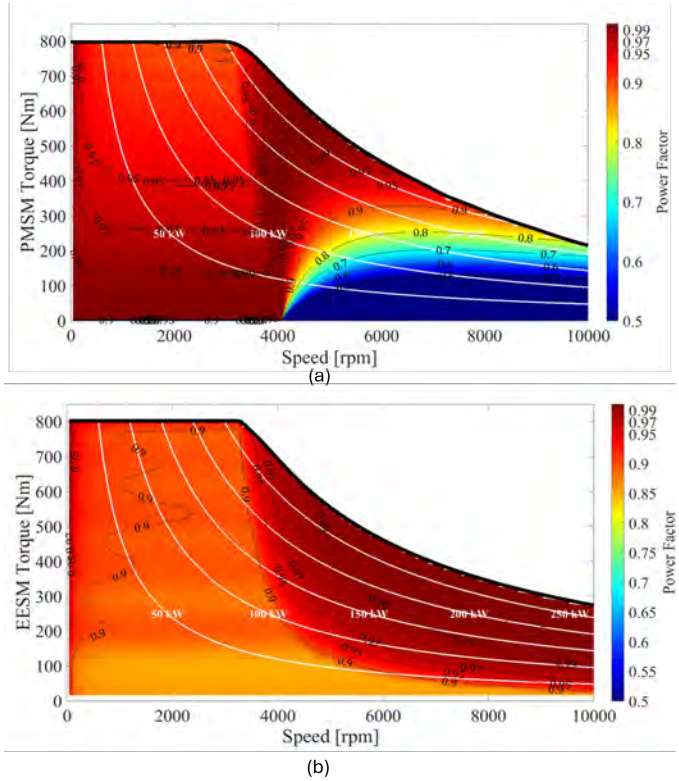

Figure 2.4: Power Factor contours along the torque-speed maps of PMSM (a) and EESM (b).

2.3 Simulation Results

The performances of the two machine drives are evaluated at the design points listed in Table 2.2. The start-up and an acceleration simulation of the truck at peak torque are presented. Subsequently, results from the Chinese Automotive Test Cycle (CATC) are shown. The official driving cycle, CHTC_TT, has been selected for this study, as it is a released standard designed for heavy trucks in China. The simulations are performed using a Matlab PLECS model, which evaluates the machine losses, and also calculates the losses and temperature of the stator inverter.

Evaluation of Critical Operating Points

The performance of both machine drives is evaluated at the critical operating points specified in Table 2.2. During the start-up operation on a road slope of 12%, a load torque of 24.48 kNm is applied to the wheels of the vehicle, corresponding to a mechanical torque of 685.22 Nm on the shaft of each motor in the drivetrain. Both the PMSM and the EESM can generate higher peak torque than the road load, allowing the vehicle to accelerate.

The operation of the machines at the other two critical points is summarized in Table 2.5. At *high power operation* both machines exhibit similar performance. However, in the *best efficiency operation* the EESM shows a 12.4% improvement in efficiency and a significantly higher power factor.

Table 2.5: Machine Operation at Critical Points

Parameter	PMSM	EESM	Unit
(1) High Power Operation			
Speed	5040	5041	rpm
Power	200	207	kW
Stator current amplitude	321.1	319.4	A
Stator voltage amplitude	443.2	443.4	V
Machine efficiency	97.1%	97.2%	%
Stator/Rotor copper loss	4.4/−	2.9/1.2	kW
Core loss	1.6	1.5	kW
Machine power factor	0.95	0.98	-
(2) Best Efficiency Operation			
Speed	8080	8064	rpm
Power	51	55	kW
Stator current amplitude	320.0	87.2	A
Stator voltage amplitude	443.3	443.4	V
Machine efficiency	86.6%	97.3%	%
Stator/Rotor copper loss	4.1/−	0.2/0.3	kW
Core loss	2.7	1.1	kW
Machine power factor	0.26	0.95	-

Simulation Results in Driving Cycle

The simulations for the CHTC_TT driving cycle are presented in the figures, with the cycle divided into two distinct segments. The first segment, lasting for 473 s, represents urban driving conditions characterized by low-speed and stop-and-go operations, depicted in red. The second segment, spanning 474−1800 s, models highway driving conditions with higher speeds and steadier operations,

shown in blue. The operating points during these segments are visualized as red and blue dots on the torque-speed operation map in Fig. 2.5 (c). In Fig. 2.5 (b) the requested torque from the dual motors configuration is shown for the considered driving cycle. A comparison in terms of efficiency and power factor reveals that the EESM operates more efficiently across most of the modeled operating points, underscoring its advantage over the PMSM. The simulation results in Fig. 2.6 for both motor drives under the CHTC_TT

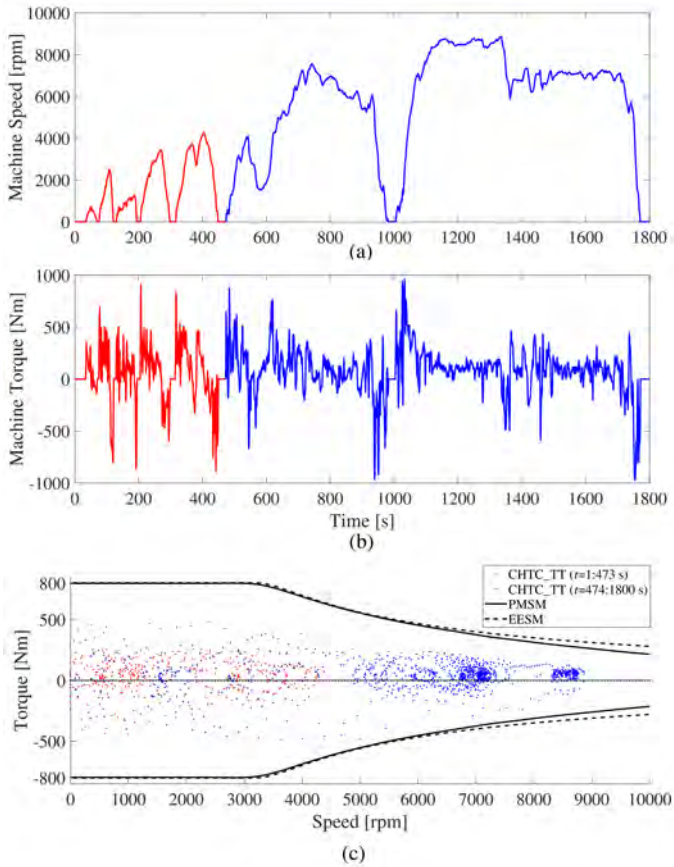

Figure 2.5: Driving cycle CHTCTT: (a) machine rotor speed, (b) total vehicle electromagnetic torque and (c) operating points along the machine torque-speed characteristic.

cycle demonstrate similar performance during the initial low-speed section. However, significant differences arise in the high-speed segment, particularly in terms of input power and losses. The PMSM requires a large amount of negative d-axis current when running with flux-weakening at high speed, increasing a lot the reactive power at the terminals of the machine. Contrary to that, a proper control of the excitation current in the EESM can maintain the reactive power quite low and relatively constant throughout the whole simulation period. Due to that reason, the stator copper losses of the PMSM are much higher than in the EESM. The core losses are also larger for the PMSM at the high-speed region of the driving cycle. The reason for this is that the PMSM operates having almost the maximum voltage for rotor speed higher than the base speed, while the EESM can have lower stator voltage, especially at the low-torque and high-speed operating points.

The energy consumption due to the electrical losses of the two machines can be calculated by integrating the curves in Fig. 2.6(c) and Fig. 2.6(f), resulting in 1420 Wh for the PMSM, and 606 Wh for the EESM. So, the EESM energy losses for the specific test cycle are 57% lower compared to the PMSM.

The comparison of input power profiles shows that the PMSM exhibits significant fluctuations, particularly during the high-speed flux-weakening region, whereas the EESM maintains a more consistent and efficient power profile. Similarly, the stator currents reveal that the PMSM negative d-axis current is a major contributor to increased losses, while the EESM achieves better current balance through its controlled excitation strategy. The rotor excitation current in the EESM remains consistent and contributes to its overall efficiency.

The energy consumption due to electrical losses further highlights the advantages of the EESM. Integrating the loss curves results in an energy consumption of 1420 Wh for the PMSM, compared to only 606 Wh for the EESM, indicating a remarkable 57% reduction in energy losses for the EESM under the CHTC_TT driving cycle. This demonstrates the superior efficiency of the EESM, particularly in high-speed and high-torque conditions, making it a more energy-efficient choice for this specific test cycle.

Inverter Results with the Driving Cycle

Similar results can be seen in Fig 2.7 (a) for the stator inverter losses, where they are higher when the inverter is used with the PMSM due to the higher

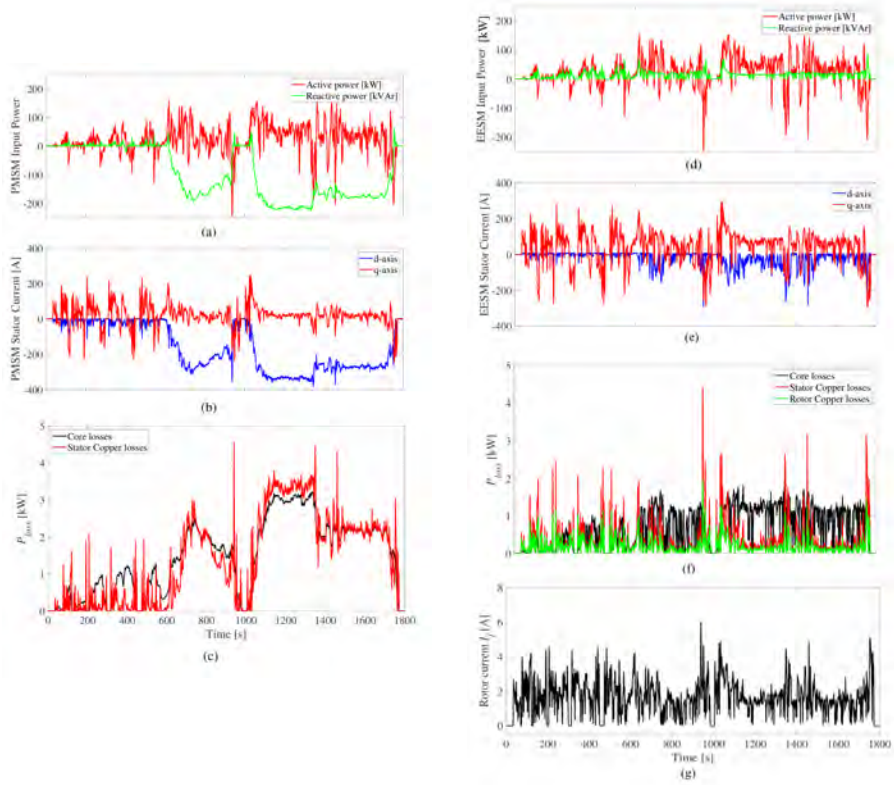

Figure 2.6: Simulation results of the PMSM (left) and EESM (right) drive with the CHTCTT cycle: (a), (d) machine input power; (b), (e) d-and q-axis stator current; (c), (f) machine losses and (d) EESM rotor excitation current.

reactive power at the high-speed operation. The semiconductor energy losses are equal to 808 Wh for the PMSM and 268 Wh for the EESM drive, showing a difference of 66.8%. This difference in the inverter losses can be explained with the use of SiC power modules, where the body diode of the MOSFETs experiences high losses when operated with lower power factor, as happens in the case of the PMSM drive. The large losses of the PMSM drive also cause higher inverter temperatures as seen in Fig. 2.7(b)-(c), which can have a negative impact on the long-term reliability of the SiC power modules.

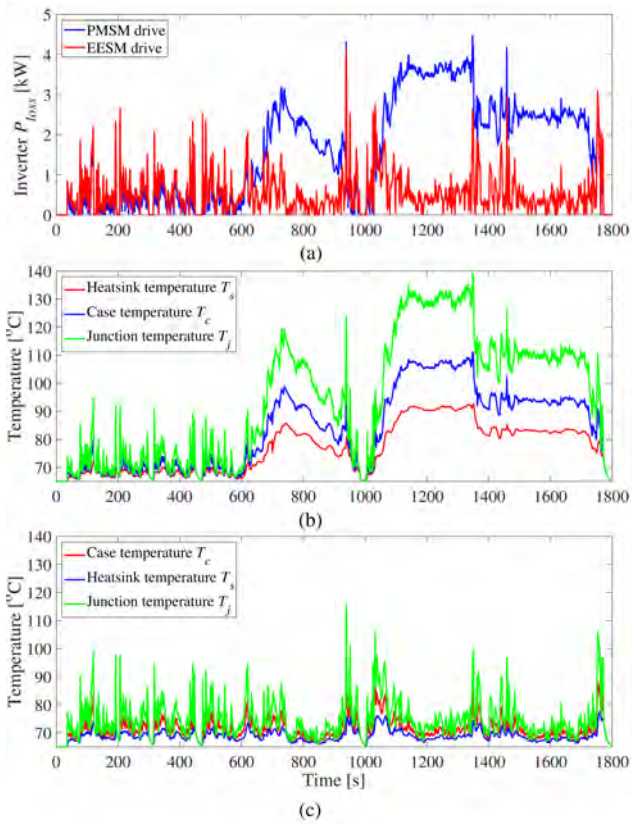

Figure 2.7: Simulation results of the three-phase inverter with the CHTCTT cycle:(a)inverter semiconductor losses; temperature of the power modules when operating with PMSM (b) and EESM (c).

Conclusions of the comparative study

The comparative analysis through driving cycle simulations has demonstrated the advantages of the EESM when used in motor drives for battery-driven trucks. The design and modelling process of an EESM drive and a similarly powered and sized PMSM drive have been presented. The performance of both systems have been compared with machine simulations on Ansys Maxwell and drive system simulations in Matlab/PLECS. The simulation results have

shown that both the motor drives can satisfy the vehicle specifications in terms of torque and power capabilities. However, due to the higher flexibility of the EESM during its design process and its better power factor at high speeds, it is easier to tune its best-efficiency region close to the most common operating points of an electric truck. These operating points are located at high speed and low torque, where the EESM shows superior efficiency compared to the PMSM. Therefore, simulation results of driving cycles for heavy trucks have shown a lower energy loss for the EESM drive, that can reach up to 57% reduction for the machine energy losses and 66.8% for the stator inverter compared to the PMSM results.

2.4 PMSM design optimization in Driving Cycle

In the previous section, the design of a PMSM for truck applications is explored to achieve performance comparable to that of an EESM with the same stator in terms of rotor MMF, maximum torque, maximum power, and maximum speed. The EESM demonstrated superior performance over the PMSM in driving cycles, particularly in terms of power factor and overall efficiency throughout the evaluated cycle.

However, it is important to note that if peak torque is not a critical requirement, the design of a PMSM can be optimized for driving cycles to enhance efficiency and power factor in the low-torque, high-speed region. This can be achieved through proper dimensioning of the permanent magnet thickness.

The methodology and findings of this optimization are detailed in ***Paper II: "Balancing Peak-Torque and Drive-Cycle Efficiency with Magnet Dimensioning of Permanent Magnet Synchronous Machines."***

CHAPTER 3

Design and Experimental Verification of 60 kW Concept EESM

In this chapter, the design and analysis of a 60 kW Electrically Excited Synchronous Machine (EESM) is presented. This machine serves as a scaled-down prototype of the full-size 200 kW design, allowing for initial experimental validation of electromagnetic modeling and simulations. The 60 kW EESM also evaluates the feasibility of the proposed dovetail rotor topology, which facilitates the formation of closed rotor slots and enables the insertion of rotor copper conductors.

Additionally, a comprehensive thermal analysis is performed to assess the temperature distribution within the machine components and identify potential hotspots under both steady-state and transient operating conditions. This evaluation is conducted using a simple water jacket cooling system.

Furthermore, the integration of the 60 kW EESM into a vehicle traction drive system is explored. Driving cycle simulations are employed to analyze machine performance in a vehicle drivetrain, assessing its viability for automotive applications.

3.1 Machine Model

The dynamic stator voltage equation of the machine in the d-q frame can be written as function of the d-axis and q-axis stator currents i_d and i_q:

$$\begin{aligned} \underline{u}_\mathrm{s} &= R_\mathrm{s} \cdot \underline{i}_\mathrm{s} + \frac{\mathrm{d}\underline{\psi}_\mathrm{s}}{\mathrm{d}t} + \mathrm{j}\omega_\mathrm{r} \cdot \underline{\psi}_\mathrm{s} \\ \Rightarrow u_\mathrm{d} + \mathrm{j}u_\mathrm{q} &= R_\mathrm{s} \cdot (i_\mathrm{d} + \mathrm{j}i_\mathrm{q}) + \frac{\mathrm{d}\left(\psi_\mathrm{d} + \mathrm{j}\psi_\mathrm{q}\right)}{\mathrm{d}t} + \mathrm{j}\omega_\mathrm{r} \cdot (\psi_\mathrm{d} + \mathrm{j}\psi_\mathrm{q}) \end{aligned} \tag{3.1}$$

where $\underline{u}_\mathrm{s}, \underline{i}_\mathrm{s}$ and $\underline{\psi}_\mathrm{s}$ are the stator voltage, current and flux linkage in the dq-frame. The d- and q-axis flux linkage ψ_d andψ_q as well as the rotor field flux linkage ψ_f can be expressed as:

$$\begin{aligned} \psi_\mathrm{d} &= L_\mathrm{d} \cdot i_\mathrm{d} + L_\mathrm{m} \cdot i_\mathrm{f} \\ \psi_\mathrm{q} &= L_\mathrm{q} \cdot i_\mathrm{q} \\ \psi_\mathrm{f} &= L_\mathrm{f} \cdot i_\mathrm{f} + \frac{3}{2} \cdot L_\mathrm{m} \cdot i_\mathrm{d} \end{aligned} \tag{3.2}$$

where L_d, L_q, L_f and L_m are respectively the d-axis inductance, the q-axis inductance, the rotor field inductance and the amplitude of the mutual inductance in the three-phases coordinate system. To be noticed that i_f is the rotor DC current.

In matrix format, the stator voltage equations together with the rotor field equation can be written as:

$$\begin{bmatrix} u_\mathrm{d} \\ u_\mathrm{q} \\ u_\mathrm{f} \end{bmatrix} = \begin{bmatrix} R_\mathrm{s} & 0 & 0 \\ 0 & R_\mathrm{s} & 0 \\ 0 & 0 & R_\mathrm{f} \end{bmatrix} \begin{bmatrix} i_\mathrm{d} \\ i_\mathrm{q} \\ i_\mathrm{f} \end{bmatrix} + \begin{bmatrix} 0 & -\omega_\mathrm{r} & 0 \\ \omega_\mathrm{r} & 0 & 0 \\ 0 & 0 & 0 \end{bmatrix} \begin{bmatrix} \psi_\mathrm{d} \\ \psi_\mathrm{q} \\ \psi_\mathrm{f} \end{bmatrix} + \frac{\mathrm{d}}{\mathrm{d}t} \begin{bmatrix} \psi_\mathrm{d} \\ \psi_\mathrm{q} \\ \psi_\mathrm{f} \end{bmatrix} \tag{3.3}$$

In order to simplify the relations, the inductance are considered constant:

$$\begin{bmatrix} u_\mathrm{d} \\ u_\mathrm{q} \\ u_\mathrm{f} \end{bmatrix} = \begin{bmatrix} R_\mathrm{s} & -\omega_\mathrm{r} L_\mathrm{q} & 0 \\ \omega_\mathrm{r} L_\mathrm{d} & R_\mathrm{s} & \omega_\mathrm{r} L_\mathrm{m} \\ 0 & 0 & R_\mathrm{f} \end{bmatrix} \begin{bmatrix} i_\mathrm{d} \\ i_\mathrm{q} \\ i_\mathrm{f} \end{bmatrix} + \begin{bmatrix} L_\mathrm{d} & 0 & L_\mathrm{m} \\ 0 & L_\mathrm{q} & 0 \\ \frac{3}{2} L_\mathrm{m} & 0 & L_\mathrm{f} \end{bmatrix} \begin{bmatrix} \frac{di_\mathrm{d}}{dt} \\ \frac{di_\mathrm{q}}{dt} \\ \frac{di_\mathrm{f}}{dt} \end{bmatrix} \tag{3.4}$$

where $-\omega_\mathrm{r} L_\mathrm{q} i_\mathrm{q}, \omega_\mathrm{r} L_\mathrm{d} i_\mathrm{d}$ and $\omega_\mathrm{r} L_\mathrm{m} i_\mathrm{f}$ represent the coupling terms, whereas the term $\omega_\mathrm{r} L_\mathrm{m} i_\mathrm{f}$ represent the back-EMF:

$$e_\mathrm{m} = \omega_\mathrm{r} \cdot L_\mathrm{m} \cdot i_\mathrm{f} \tag{3.5}$$

the EMF on d - and q -axis can be also defined:

$$e_{\mathrm{d}} = -\omega_{\mathrm{r}} \cdot L_{\mathrm{q}} \cdot i_{\mathrm{q}} = -x_{\mathrm{q}} \cdot i_{\mathrm{q}}, \tag{3.6}$$

$$e_{\mathrm{q}} = \omega_{\mathrm{r}} \cdot L_{\mathrm{d}} \cdot i_{\mathrm{d}} + \omega_{\mathrm{r}} \cdot L_{\mathrm{m}} \cdot i_{\mathrm{f}} = x_{\mathrm{d}} \cdot i_{\mathrm{d}} + e_{\mathrm{m}}. \tag{3.7}$$

where x is the reactance, e the EMF and m denotes the mutual terms. In steady state, the derivatives become zero, giving:

$$\begin{bmatrix} U_{\mathrm{d}} \\ U_{\mathrm{q}} \\ U_{\mathrm{f}} \end{bmatrix} = \begin{bmatrix} R_{\mathrm{s}} & -\omega_{\mathrm{r}} L_{\mathrm{q}} & 0 \\ \omega_{\mathrm{r}} L_{\mathrm{d}} & R_{\mathrm{s}} & \omega_{\mathrm{r}} L_{\mathrm{m}} \\ 0 & 0 & R_{\mathrm{f}} \end{bmatrix} \begin{bmatrix} I_{\mathrm{d}} \\ I_{\mathrm{q}} \\ I_{\mathrm{f}} \end{bmatrix} \tag{3.8}$$

The saliency ratio is defined as the ratio of the inductances between the d-axis and q-axis:

$$k_{\mathrm{saliency}} = \frac{L_{\mathrm{d}}}{L_{\mathrm{q}}} \tag{3.9}$$

A machine is considered "non-salient" when $k_{\mathrm{dq}} = 1$, whereas it is classified as "salient" when $k_{\mathrm{dq}} \neq 1$.

Based on the representation in the dq-coordinate system, the electromagnetic power P_{em} can be expressed as:

$$\begin{aligned} P_{\mathrm{em}} &= \frac{3}{2} \cdot \mathrm{Re}\left\{e_{\mathrm{s}} \cdot i_{\mathrm{s}}^{*}\right\} \\ &= \frac{3}{2} \cdot \left(e_{\mathrm{d}} \cdot i_{\mathrm{d}} + e_{\mathrm{q}} \cdot i_{\mathrm{q}}\right) \\ &= \frac{3}{2} \cdot \left[e_{\mathrm{m}} + \left(x_{\mathrm{d}} - x_{\mathrm{q}}\right) \cdot i_{\mathrm{d}}\right] \cdot i_{\mathrm{q}} \end{aligned} \tag{2-33}$$

where e_{s}^{*} denotes the conjugate of the stator EMF vector in the dq-coordinate system. The electromagnetic torque T_{em} can be derived from the electromagnetic power as follows:

$$T_{\mathrm{em}} = \frac{P_{\mathrm{em}}}{\Omega_{\mathrm{r}}} = \frac{3}{2} \cdot p \cdot \mathrm{Im}\left\{\psi_{\mathrm{s}}^{*} \cdot i_{\mathrm{s}}\right\} = \frac{3}{2} \cdot p \cdot \left(\psi_{\mathrm{d}} \cdot i_{\mathrm{q}} - \psi_{\mathrm{q}} \cdot i_{\mathrm{d}}\right) \tag{2-37}$$

Here, p refers to the number of pole pairs, and Ω_{r} represents the mechanical angular speed. Assuming constant inductances in the d- and q-axes, the

expression simplifies to:

$$T_{\mathrm{em}} = \frac{3}{2} \cdot p \cdot [L_{\mathrm{m}} \cdot i_{\mathrm{f}} + (L_{\mathrm{d}} - L_{\mathrm{q}}) \cdot i_{\mathrm{d}}] \cdot i_{\mathrm{q}} \tag{2-38}$$

Regarding the losses, the total copper losses are composed of the stator copper loss and rotor copper loss:

$$P_{\mathrm{Cu,s}} = 1.5 \cdot R_{\mathrm{s}} \cdot \left(i_d^2 + i_q^2\right) \tag{3.10}$$

$$P_{\mathrm{Cu,\,r}} = R_{\mathrm{r}} \cdot i_{\mathrm{f}}^2 \tag{3.11}$$

where R_s and R_r denote the resistances of the stator and the rotor. To account for the dependence of the stator resistance on frequency and temperature, the following expressions are used:

$$R_{AC}(f) = a \cdot f^2 + b \cdot f + R_{DC} \tag{3.12}$$

$$R(T) = R_{AC}\left[1 + \alpha\left(T - T_0\right)\right] \tag{3.13}$$

where a and b are the frequency coefficients of stator resistance, α is the copper temperature coefficient, T and T_0 are the current and reference temperatures.

Core losses are derived from FEM for all d- and q-axis current values at one fixed frequency, then adjusted for other frequencies as described in [41]. The core losses are evaluated using the scaling method, which accounts for their dependence on rotor frequency using the following relationship:

$$P_{\mathrm{Fe}}(I_d, I_q, I_f, f_2) = \frac{k_h \cdot f_2 + k_c \cdot f_2^2}{k_h \cdot f_1 + k_c \cdot f_1^2} \cdot P_{\mathrm{Fe}}(I_d, I_q, I_f, f_1) \tag{3.14}$$

Here, $P_{\mathrm{Fe}}(I_d, I_q, I_f, f_1)$ represents a 3-D lookup table of core losses calculated at the rotor frequency f_1 using FEM simulations. The coefficients k_h and k_c describe the hysteresis and eddy current characteristics of the iron material, respectively. The term $P_{\mathrm{Fe}}(I_d, I_q, f_2)$ corresponds to the scaled core loss at the rotor frequency f_2. It is worth noting that this scaling method can be improved by considering a greater number of frequency/speed points, which enhances accuracy, particularly across wide speed ranges.

The efficiency is computed using the following formula:

$$\eta = \frac{P_{\mathrm{out}}}{P_{\mathrm{in}}} = \frac{T_{\mathrm{em}}\Omega_{\mathrm{mech}}}{T_{\mathrm{em}}\Omega_{\mathrm{mech}} + P_{\mathrm{Cu,s}} + P_{\mathrm{Cu,r}} + P_{\mathrm{Fe}}} \tag{3.15}$$

where P_{out} and P_{in} are the output and input power, respectively, and Ω_{mech} is the shaft speed. Mechanical losses are not included in this computation, since they are largely affected by the type of bearings as well as on the rotor topology.

Finally, the power factor can be calculated as:

$$PF = \frac{P_{\text{in}}}{S_{\text{in}}} = \frac{T_{\text{em}}\Omega_{\text{mech}} + P_{\text{Cu,s}} + P_{\text{Cu,r}} + P_{\text{Fe}}}{\frac{3}{2}U_{\text{s}}I_{\text{s}}} \tag{3.16}$$

3.2 Machine Specifications

The machine under study is a 60 kW EESM that can be considered suitable for automotive applications. The topology consists in a salient poles shaft-mounted rotor, where the rotor consists of 8 poles surrounded by the winding needed for the dc excitation. The specifications of the designed motor are summarized in Table 3.1. The motor features a stator outer diameter of 175 mm and an active length of 120 mm, with a total of 8 poles. The rotor and stator fill factors are 0.4 and 0.6, respectively, which reflect the effective utilization of the available winding space. Cooling is achieved using a water jacket with 8 channels, maintaining a coolant temperature of 60°C to ensure thermal stability under continous operation.

The motor is capable of delivering a maximum power output of 60 kW and a peak torque of 220 Nm. It operates at a base speed of 3500 rpm, with a maximum rotational speed of 10000 rpm. The DC-link voltage is 360 V and the peak stator current density reaches 30 A/mm^2 whereas the rotor current density is limited to 25 A/mm^2.

In this study, the primary focus is on optimizing the electromagnetic design in order to maximize the maximum torque and the power density of the EESM. As a result, the current densities are intentionally pushed to their limits. However, in the continuous operating region, the current densities remain within a reasonable range for a water-jacket cooling application, with values around 11 A/mm^2 for the stator and 5 A/mm^2 for the rotor.

Table 3.1: 60 kW EESM Specifications

Parameter	Value	Unit
Stator Outer Diameter	175	mm
Active Length	120	mm
Number of Pole Pairs p	8	
Rotor Fill Factor $k_{\mathrm{r,fill}}$	0.4	
Stator Fill Factor $k_{\mathrm{s,fill}}$	0.6	
Number of channels of water jacket	8	
Temperature of the coolant	60°	Celsius
Maximum Power $P_{\max}$	60	kW
Maximum Torque $T_{\max}$	220	Nm
Base Speed n_{base}	3500	rpm
Maximum Speed $n_{\max}$	10000	rpm
DC-Link Voltage V_{DC}	360	V
Peak Stator Current Density $J_{\mathrm{s,max}}$	30	$\mathrm{A/mm^2}$
Peak DC Rotor Current Density $J_{\mathrm{r,max}}$	25	$\mathrm{A/mm^2}$

3.3 Electromagnetic Design

The electromagnetic design of EESMs is intrinsically linked to the mechanical and thermal design. This connection arises due to the placement of active conductors within the rotor, which introduces significant mechanical and manufacturing challenges. These challenges have a profound impact on the electromagnetic performance of the machine, making a holistic design approach essential.

In this study, the electromagnetic design is driven by two primary objectives: achieving a unity power factor in the high-speed region near the torque-speed envelope and optimizing the rotor pole topology.

The Unity Power Factor criterion, as described in [42], is mostly affecting the machine electric design (windings design and configuration) and it is employed to ensure a unitary power factor during field-weakening operation in proximity of the torque-speed envelope. By neglecting resistive voltage drops and flux leakage, this criterion simplifies to achieving a balance between the rotor and stator magnetomotive forces (MMFs), as shown by the following equation:

$$Q{=}0 \Longrightarrow \mathrm{MMF}_s \approx \mathrm{MMF}_r \tag{3.17}$$

where Q is the input reactive power and MMF_s and MMF_r the stator and

rotor magentomotive force respectively. As a result, the rotor winding configuration is carefully determined to generate a rotor magnetomotive force capable of balancing the total MMF produced by the stator windings. The procedure for the machine electric design is shown in Fig. 3.1. The process represented in the flowchart outlines the systematic electrical design of the EESM, focusing on both the stator and rotor electric circuits. The process begins with the definition of key input parameters, which are determined by the green-colored system requirements from Table 3.1. These parameters include the maximum switching frequency ($f_{\mathrm{sw,\,max}}$), maximum power (P_{max}), maximum torque (T_{max}), and DC bus voltage (V_{DC}). Based on these inputs, the number of pole pairs (p) is determined. Additionally, the maximum switching frequency defines the maximum speed limit of the machine, which is critical for synchronous motor operation.

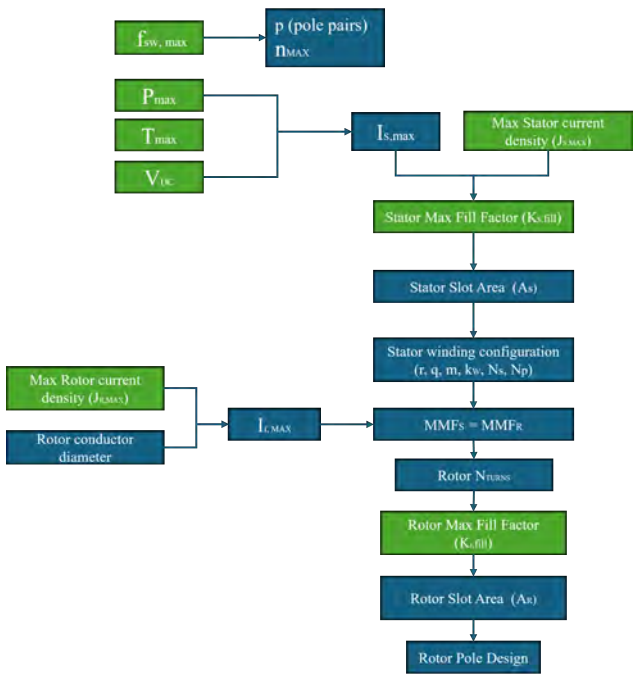

Figure 3.1: Flowchart illustrating the electrical design process for stator and rotor windings, highlighting key parameters and interdependencies.

The design then transitions to the stator, where the maximum stator current ($I_{S,\max}$) is calculated from the maximum power and voltage. Considering the maximum stator current density ($J_{S,\max}$) and the stator fill factor ($K_{S,\text{fill}}$), the effective utilization of the stator slot area (A_S) can be determined. This slot area is then used to define the stator winding configuration, which includes parameters such as the number of slots per pole per phase (q), the number of layers, the winding factor (k_w), the number of phases (m, typically three), the number of series turns (N_S), and the number of parallel branches (N_P).

Once the stator winding design is completed and the stator MMF is determined, the process shifts to the rotor. The maximum rotor current density ($J_{R,\max}$) is considered to ensure that the rotor conductors can handle the allowable current without exceeding thermal limits. The rotor conductor diameter is selected based on standard catalog availability, which allows for the calculation of the maximum rotor DC current amplitude ($I_{f,\max}$). Since the rotor magnetomotive force must balance the stator MMF, the number of rotor turns can be determined for placement within the rotor slots. The rotor winding configuration is then finalized to ensure this balance is achieved.

The rotor fill factor ($K_{R,\text{fill}}$) is introduced to quantify the percentage of copper that can fit within the rotor slot, accounting for manufacturing constraints, insulation, and air fillers. This fill factor is used to assess the effective utilization of the rotor slot area (A_R). Once the slot dimensions are determined, the rotor lamination can be designed, as it plays a critical role in shaping the magnetic circuit. The second criterion for the electromagnetic design involves the optimization of the rotor poles. The initial design decision revolves around whether to adopt open slots or closed slots for the rotor. Open slots are characterized by the presence of space between the termination of one pole shoe and the termination of the adjacent pole shoe. Typically, this spacing is designed to be equal to or greater than 3-5 times the diameter of the rotor conductors, allowing sufficient room for the insertion of conductors into the rotor slots formed between the poles.

In contrast, closed slots are created by extending the rotor poles until they touch each other, fully enclosing the rotor slots. This configuration, while maximizing the slot area for placing active conductors, poses challenges for winding the rotor conductors around the poles. To address this, alternative pole mounting techniques, such as the dovetail joint, must be adopted. Figure 3.2 illustrates both configurations, highlighting their respective advantages

and disadvantages in terms of the electromagnetic performance of the EESM.

In the case of closed slots, the rotor slot area is maximized, allowing for a higher fill factor and consequently reducing the field current density. However, the magnetic connection between adjacent poles results in increased leakage flux, as a portion of the flux produced by the rotor excitation leaks toward the adjacent pole shoe rather than crossing the air gap to the stator. This leakage flux leads to a reduction in average torque, power factor, and overall efficiency.

On the other hand, open slots minimize leakage flux, which is beneficial for maintaining electromagnetic performance. However, this configuration reduces the available slot area for placing copper conductors. To achieve an equivalent rotor slot area, additional components such as wedges and retaining sleeves are required to prevent conductors from being ejected during rotor rotation. Furthermore, open slots increase torque ripple due to the higher third and fifth harmonics in the stator induced back EMF, which correspond to an increase in the sixth and twelfth torque harmonics. The Fig. 3.3 compares the harmonic content and torque characteristics of the Prototype motor for two different slot configurations: closed slots (left) and a 5 mm slot opening (right). The main observation is the trade-off between peak torque and torque

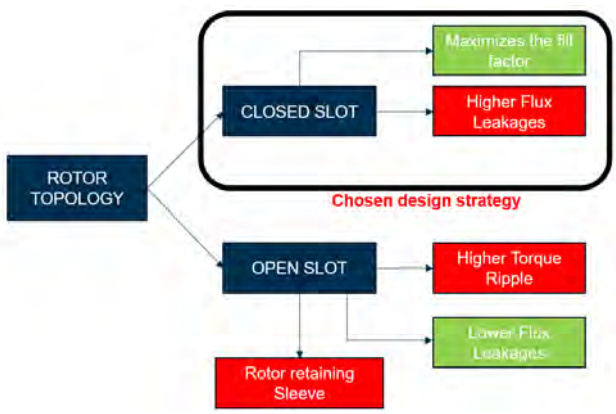

Figure 3.2: Comparison of rotor slot topologies highlighting design trade-offs: Closed slots maximize the fill factor but increase flux leakage, while open slots reduce flux leakage at the expense of higher torque ripple and require a rotor retaining sleeve.

ripple. For the closed slots configuration, the motor achieves a peak torque of 213.4 Nm with a torque ripple of 2.55%. In contrast, with a 5 mm slot opening, the peak torque increases to 220 Nm, but the torque ripple rises significantly to 13.45%, indicating a substantial degradation in torque smoothness. The 12th harmonic, highlighted in red, plays a critical role in this increase. Its amplitude grows from 2.89 Nm in the closed slot configuration to 15 Nm with the slot opening, showing that larger slot openings exacerbate harmonic distortions.

The rotor pole shape is also one of the keys factors in the electromagnetic design otpimization. The key design parameters for the optimization are represented in Fig. 3.4. This figure illustrates the geometric parameters of a pole used in the machine design, highlighting their impact on magnetic and mechanical performance. The pole shoe width represents the horizontal dimension of the pole shoe, which plays a crucial role in determining the flux distribution and the air-gap magnetic field. It is directly connected to the leakage flux and the corresponding average torque generated. The pole shoe height, defined as the vertical height of the shoe, influences the structural integrity and the flux-carrying capacity of the pole. At the edge, the pole shoe termination thickness governs magnetic saturation and edge effects. Also, the

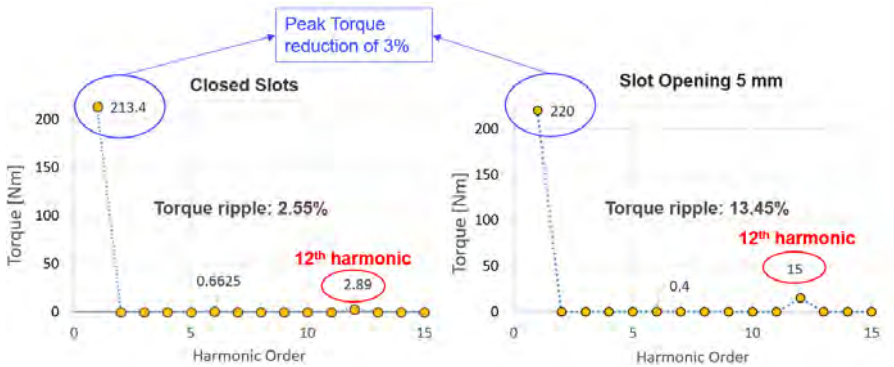

Figure 3.3: Comparison of torque harmonics and ripple for different rotor slot configurations: Closed slots exhibit a low torque ripple of 2.55% with a dominant first harmonic at 213.4 Nm, while a 5 mm slot opening increases torque ripple significantly to 13.45%, with a slightly higher first harmonic at 220 Nm.

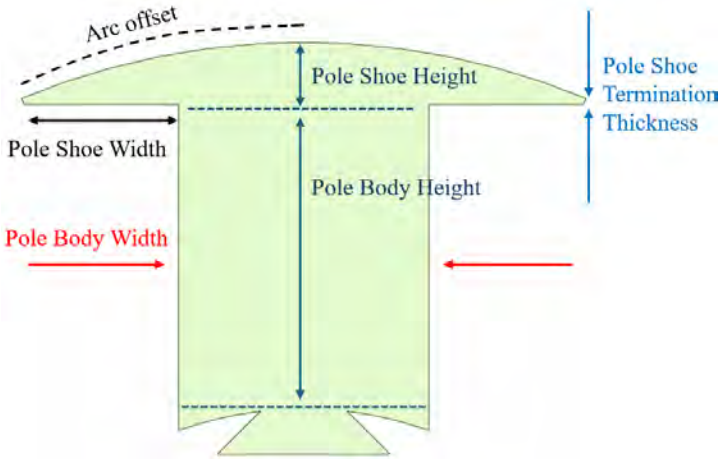

Figure 3.4: Illustration of pole geometry dimensions for rotor design: Key parameters include Pole Shoe Width, Pole Shoe Height, Pole Shoe Termination Thickness, Pole Body Width, and Pole Body Height, with the arc offset defining the curvature of the pole shoe.

pole shoe termination thickness is stronlgy dependent to mechanical stress and deformation as it will be explained in the next section. The arc offset, representing the curvature of the pole shoe, directly affects the air-gap magnetic field distribution and the overall efficiency of the machine. A more sinusoidal-shaped arc offset will lead to improved torque ripple but lower average torque. Moving to the body, the pole body width, which is the horizontal width of the pole body, carries the majority of the magnetic flux and prevents saturation, while the pole body height, or the vertical height of the pole body, is critical for mechanical integrity.

Together, these parameters form the basis for optimizing pole geometry in the machine, ensuring a balance between magnetic and mechanical performance. Fig 3.5 illustrates the iterative design process for optimizing the rotor pole geometry, integrating electromagnetic and mechanical design considerations. The process begins with the *Parameters Adjustment* stage, where key geometric dimensions such as pole shoe width, pole shoe height, pole body width, pole body height, arc offset, and pole shoe termination thickness are adjusted to influence machine performance.

The inner loop, labeled as *Electromagnetic Design*, evaluates the effects of these adjustments by analyzing critical performance metrics, including torque ripple, average torque, back electromotive force (back-EMF), and iron core losses. This feedback ensures that the design aligns with electromagnetic performance targets. Simultaneously, the inner loop for *Mechanical Design* ensures that the adjusted parameters meet structural and mechanical integrity requirements, such as maintaining a robust and manufacturable geometry.

Finally, the outer loop, labeled as *Final Design*, integrates both electromagnetic and mechanical results to achieve an optimized design. This iterative process ensures a balanced solution that meets both performance and structural criteria.

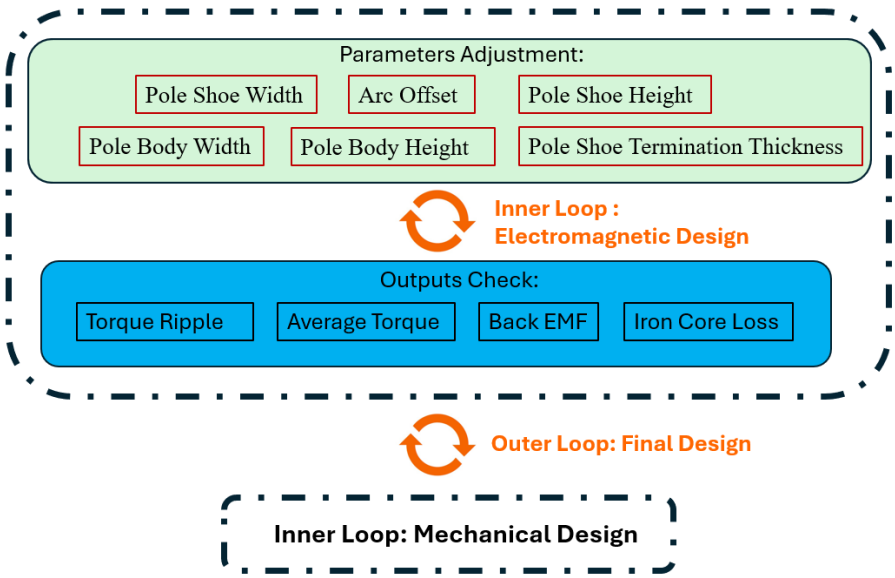

Figure 3.5: Flowchart of the iterative design process for rotor pole geometry optimization. The process starts with parameter adjustments, including pole shoe width, pole shoe height, pole body width, pole body height, arc offset, and pole shoe termination thickness. The electromagnetic inner loop evaluates design performance based on outputs such as torque ripple, average torque, back EMF, and iron core losses. Simultaneously, the mechanical inner loop ensures structural integrity. The outer loop integrates these results to finalize the optimized design.

Once the final design is selected, Maximum-Torque Per Ampere (MTPA) control is implemented alongside simulation work to generate output maps in the T-ω plane as shown in Fig. 3.6. The EESM is assumed to be current-controlled, and sinusoidal currents are therefore applied in the FEM analysis. The procedure for implementing the efficiency map consists of the following steps.

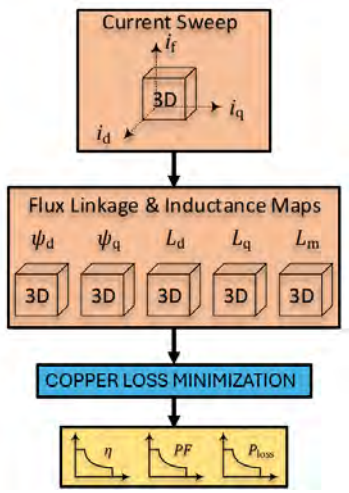

Figure 3.6: Flowchart of the algorithm for the generation of torque-speed maps of the optimized design consisting of four main steps: current sweep of the stator d- and q- axis currents as well as the rotor field current within the range of the requested maximun power and maximum torque; generation of the corresponding flux linkage map for each combination of currents; filtering of the obtained data to search for MTPA solutions; calculation and maps generation of the wanted output data (e.g. efficiency, power factor and losses).

First, a parametric sweep of transient FEM simulations is conducted by varying the current magnitude while maintaining the base speed. The currents involved in the sweeping process are three for EESM: d-axis stator current I_d, q-axis stator current I_q, and rotor field current I_f. This process generates a set of flux linkage and core loss values, which are subsequently tabulated. Next, the iterative optimization algorithm for copper loss minimization, as presented in [42], is applied using the flux linkage maps obtained from the

FEM calculations. This algorithm identifies the optimal operating points that minimize copper losses. Finally, the efficiency and power factor are calculated based on the points filtered by the optimization algorithm.

3.4 Mechanical Design

The salient poles structure with closed slot is chosen for the 60 kW EESM under study. To secure the active conductors without relying on wedges and sleeves, and to minimize torque ripple, dovetail joints are employed in the design of the Prototype EESM. This approach significantly simplifies the manufacturing process by enabling the conductors to be wrapped around the rotor salient poles prior to assembling the poles onto the shaft, thereby forming closed slots. This assembly method is illustrated in Fig. 3.7.

Integrating mechanical analysis into the design optimization process, as depicted in Fig. 3.5, is critical to ensure the mechanical integrity of the rotor poles, particularly the dovetail joints, under high-speed operation. At elevated rotational speeds, the stress, deformation, and potential displacement of the rotor components increase due to the rising centrifugal forces.

The relationship between the centrifugal force and rotational speed can be simplified as:

$$F_c = m\frac{v^2}{r}$$

where F_c is the centrifugal force (in Newtons, N), m is the mass of the object (in kilograms, kg), v is the tangential speed of the object (in meters per second, m/s), and r is the radius of the circular path (in meters, m). A robust mechanical design must account for the centrifugal forces under extreme operating conditions that corresponds to the maxmum speed. The torque (T) generated by the rotor also introduces forces on the dovetail joints. The tangential force (F_t) resulting from torque is given by:

$$F_t = \frac{T}{r}$$

where F_t is the tangential force (in Newtons, N) and T is the torque acting on the rotor (in Newton-meters, $N \cdot m$). Both the centrifugal and tangential forces must be included in the analysis to ensure that the dovetail joints and rotor poles can withstand the combined stress under high-speed and high-torque

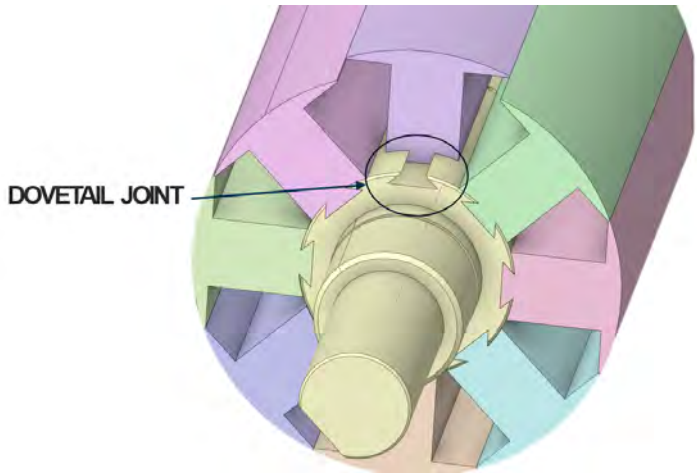

Figure 3.7: Illustration of the dovetail joint used in the rotor design of the Prototype EESM. The dovetail joint secures the active conductors, eliminates the need for wedges and sleeves, and facilitates assembly by allowing the conductors to be wrapped around the salient poles before mounting the poles on the shaft.

conditions. For this study, the worst case scenario for the mechanical analisys is considered the case where the machine is running at maximum speed with a value of torque close to the continuous torque, since the machine is supposed to survive in the high speed region (flux weaking region) for very long time. The point considered for the mechanical analysis is shown in Fig. **??** where the maximum speed of 10000 rpm and the continuous torque of 50 Nm are considered.

Extensive simulations are performed to verify that the design parameters obtained from the electromagnetic design optimization meet the necessary mechanical requirements, as outlined in the algorithm depicted in Fig. 3.9. The design process shown is structured into an outer loop and an inner loop for mechanical design, where the former coordinates the overall optimization process, and the latter ensures the mechanical integrity of the rotor. The electromagnetic design, which primarily focuses on optimizing performance parameters such as flux distribution and torque ripple, has been comprehensively discussed in the previous section. The focus here is on the mechanical

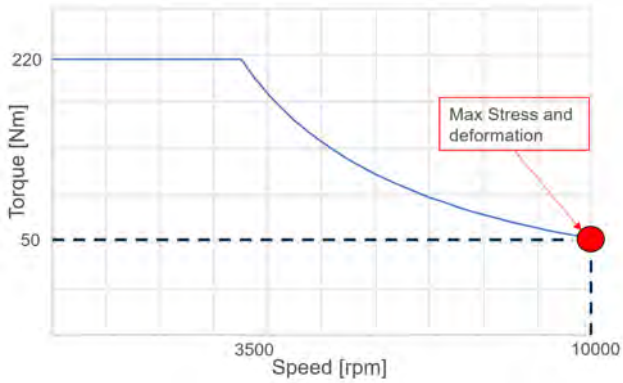

Figure 3.8: Mechanical requirements for the 60 kW Concept EESM.

design, which is critical for ensuring the structural viability of the system under operational stresses. The inner loop for mechanical design evaluates the mechanical behavior of the rotor using Finite Element Method (FEM) simulations. These simulations calculate the maximum Von Mises stress, which indicates the likelihood of yielding; the maximum displacement, representing the total movement of rotor components under operational forces; and the maximum deformation, which quantifies changes in the rotor geometry due to stress and strain. The results are assessed against material properties, including the tensile ultimate strength and tensile yield strength, to verify that the mechanical design can withstand the centrifugal and tangential forces arising during high-speed operation.

Part of the optimization is shown in Fig. 3.10 which evaluates the mechanical performance of the rotor under operational stresses for different dimensions of the dovetail. The analysis focuses on key regions, including the bottom side, upper neck (left and right), bottom neck (left and right) of the dovetail. Also the pole shoe termination are taken into account, each of which is critical from both stress and displacement prospective. The maximum Von Mises stress is plotted against variations in dovetail height and width to investigate their impact on the mechanical robustness of above-mentioned rotor parts. For the bottom side of the dovetail, the maximum Von Mises stress decreases significantly with an increase in dovetail height, stabilizing around 4 to 5mm. The relationship with dovetail width, however, shows a slight increase in stress be-

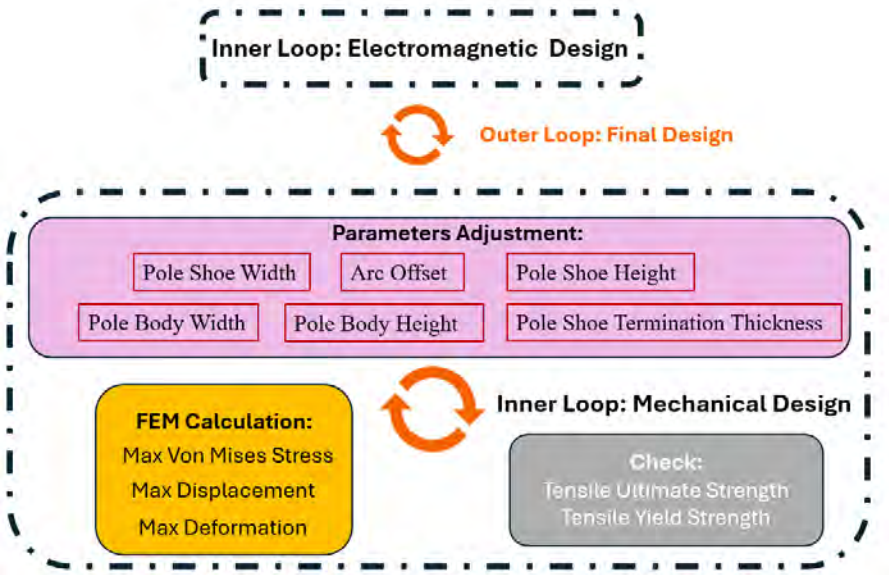

Figure 3.9: Algorithm for the mechanical optimization process.

yond an optimal range, indicating a trade-off that requires careful adjustment of width to maintain acceptable stress levels. In the upper neck regions of the dovetail, both left and right, the stress is highly sensitive to the dovetail height, with a sharp decline as height increases and stabilization observed at approximately 4 mm. The width in this region shows a moderate increase in stress after an initially stable range, suggesting the need for precise control of the geometric dimensions to avoid stress concentrations. Finally, the overall maximum stress along the entire rotor assembly is examined to identify the worst-case scenario for each combination of dovetail height and width. The results show that increasing the dovetail height consistently reduces the maximum stress, while the effect of dovetail width is more complex and varies depending on the specific region. The dovetail bottom neck regions, left and right, exhibit similar trends, where an increase in dovetail height leads to a notable reduction in stress levels. The width, however, displays a more complex and non-linear relationship with stress, requiring detailed analysis to determine an optimal configuration.

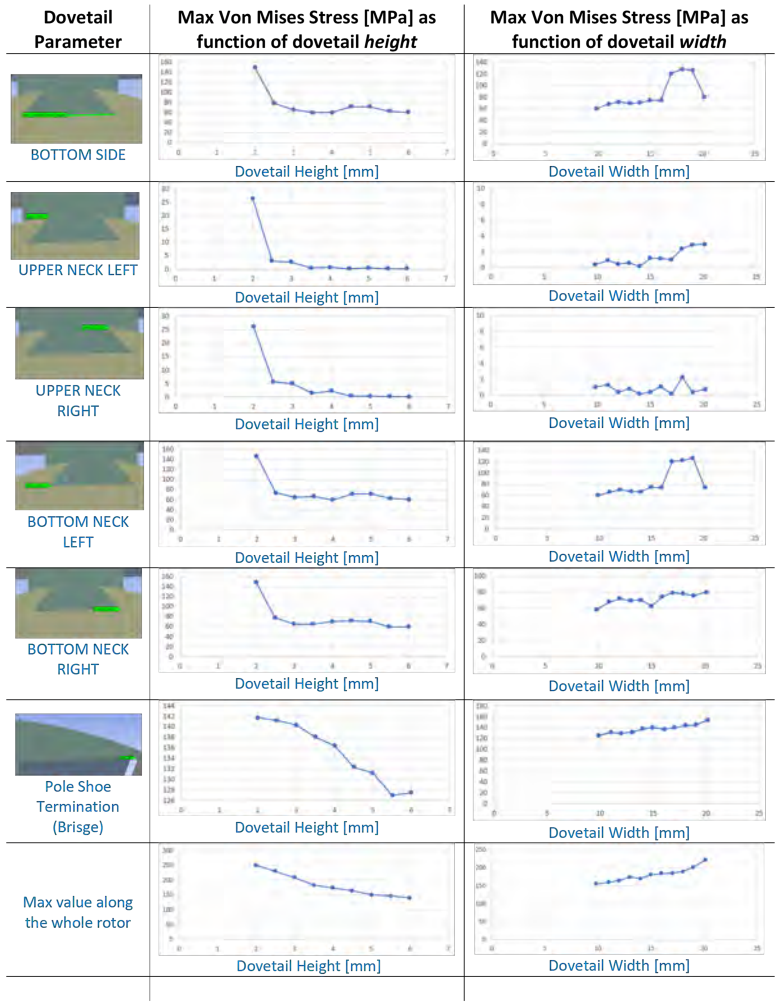

Figure 3.10: Dovetail optimization results showing the variation of maximum Von Mises stress across different parts of the rotor as a function of dovetail height and width.

In the pole shoe termination region, which plays a critical role in ensuring the structural stability of the rotor, the maximum stress decreases consistently with increasing dovetail height, while an increase in dovetail width leads to a steady rise in stress. These observations highlight the need for a balance between height and width to achieve a mechanically robust design.

3.5 Design Results

This section presents the simulation results of the electromagnetic and mechanical design of the Concept 60 kW EESM. Additionally, the experimental setup is described, and experimental results are provided to validate the electromagnetic model against the measurements.

Electromagnetic Results

The magnetic flux density distribution of the Concept 60 kW EESM is shown under two operating conditions in Fig 3.11: no-load with maximum excitation (a) and peak torque operation (b). In the no-load condition with maximum excitation, the motor operates without any applied load, and the flux is primarily established by the rotor excitation system. The saturation is most evident in the rotor poles and at the stator tooth tips, as indicated by the red regions where the flux density approaches 2 T. These regions demonstrate the limits of the magnetic material capability to carry additional flux. The flux is evenly distributed, with smooth contour lines radiating from the rotor poles to the stator teeth, reflecting the absence of armature reaction effects.

Under peak torque operation, the rotor excitation field interacts with the armature field generated by the stator to produce maximum electromagnetic torque. In this condition, saturation is more widespread compared to the no-load case. It is particularly evident in the rotor poles, especially at the edges near the air gap, and in the stator teeth, where significant localized saturation occurs at the tips. This is due to the combined effects of the rotor and stator magnetic fields. The flux contours are distorted in the air gap region, showing the impact of the armature reaction. This distortion highlights how the load influences the magnetic circuit and points to regions where the material is operating near its magnetic saturation point. In Fig. 3.12, the two graphs illustrate the electromagnetic torque characteristics as function of the stator

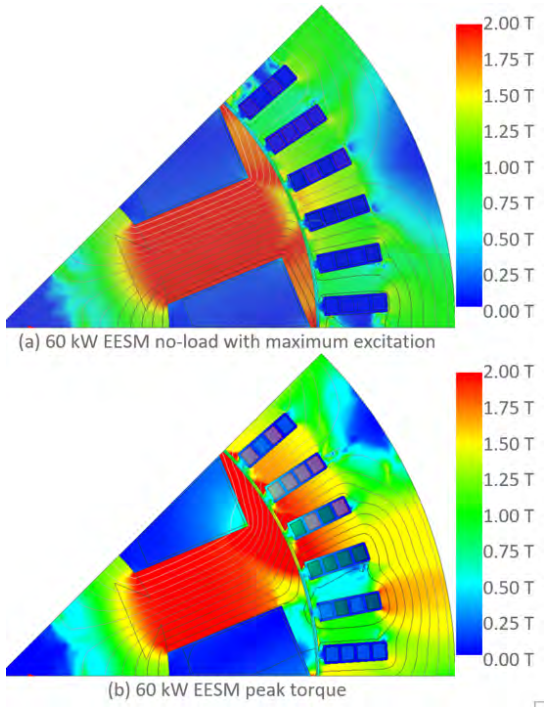

Figure 3.11: Magnetic flux density distribution of a 60 kW EESM: (a) no-load condition with maximum excitation, and (b) peak torque operation

current angle and rotor speed respectively. The first graph in in Fig. 3.12(a) shows the torque profile as a function of the current angle at maximum current. The current angle, measured in degrees, represents the angular position of the stator current relative to the rotor magnetic field. As the current angle increases from 0° to 90°, the electromagnetic torque rises, reaching its peak value around 90° (Maximum Torque per Ampere, MTPA). Beyond 90°, the torque starts to decrease, indicating that the alignment of the stator current with the rotor field becomes less optimal. The second graph (b) depicts the torque-speed envelope of the motor to check that the final design fully satisfy the initial requirements in terms of maximum torque and maximum power. At low speeds, the motor maintains a constant torque around 220 Nm, as evidenced by the flat portion of the curve. As the speed increases beyond the

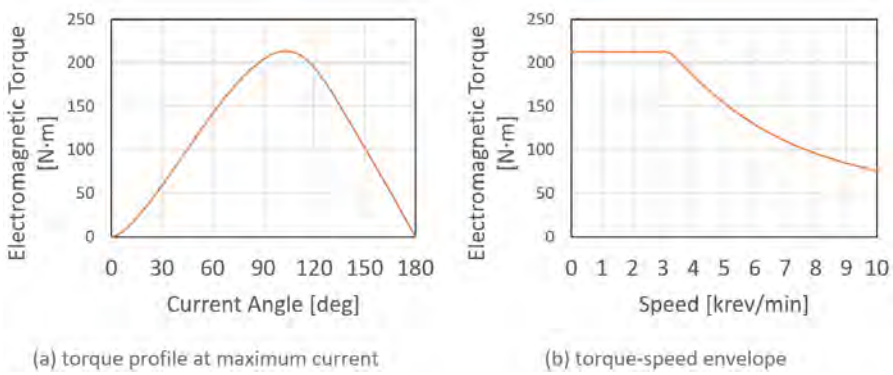

Figure 3.12: Electromagnetic torque characteristics: (a) torque profile as a function of the stator current angle; (b) torque envelope as function of the rotor mechanical speed.

base speed, the torque begins to decline, following an inverse relationship with speed. This region, known as the constant power region or field weakening, illustrates the motor ability to maintain constant power output by trading off torque for speed.

The set of four contour maps shown in Fig. 3.13 provides a comprehensive analysis of key performance metrics for an electric motor across its operational torque-speed range. The x-axis represents speed in revolutions per minute (rev/min), while the y-axis represents torque in Newton-meters (Nm). Each map focuses on a specific characteristic of the motor. Subfigure (a) illustrates the motor efficiency, highlighting regions where energy conversion is optimal. Subfigure (b) shows the total copper losses (sum of stator and rotor), which are primarily dependent on the motor current and torque levels. Subfigure (c) presents the power factor, demonstrating how effectively electrical input power is converted into useful mechanical power. Finally, subfigure (d) depicts the iron losses, which are largely influenced by the operating speed and magnetic saturation.

Efficiency in subfigure (a) is highest (above 95%) in regions where both copper and iron losses are minimal, such as at moderate speeds and torques. Subfigure (b) shows that copper losses dominate at high torque levels and increase slightly as speed rises, resulting in lower efficiency in those regions of subfigure (a). Conversely, subfigure (d) demonstrates that iron losses are

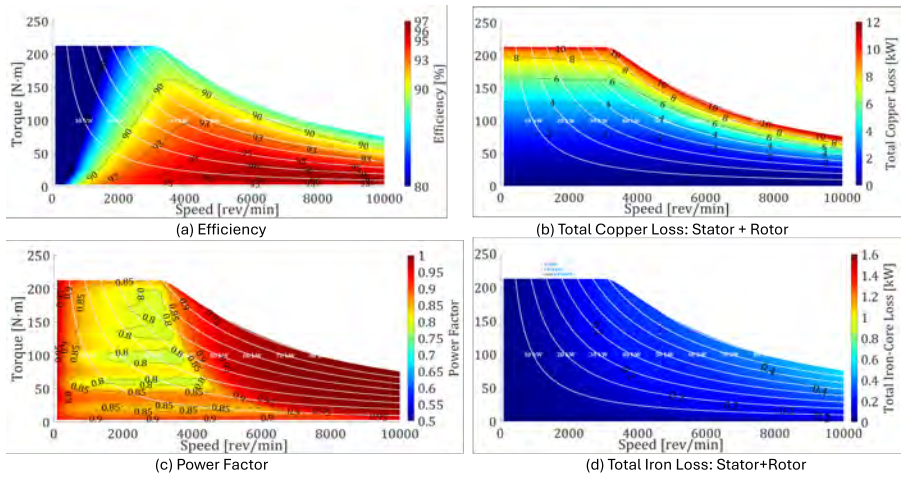

(a) Efficiency

(b) Total Copper Loss: Stator + Rotor

(c) Power Factor

(d) Total Iron Loss: Stator+Rotor

Figure 3.13: Performance torque-speed maps of Concept 60 kW EESM: (a) efficiency; (b) copper losses (stator + rotor); (c) power factor; (d) iron losses (Stator+Rotor).

relatively small across most of the operating range but become significant at higher speeds, contributing to the efficiency drop in subfigure (a) at high speeds and low torques. The iron losses are moslty caused by the operating frequency of the stator that at high speed generates iron losses in the stator core and harmonic losses on the rotor surface.

The power factor shown in subfigure (c) is highest (close to 1) at higher speeds and on the curve envelope as result of the Unity Power Factor criterion used at design phase. However, at high torques and low speeds, the power factor decreases reaching a minimum value around 0.8.

Mechanical Results

The results from the mechanical FEM analisys for the rotor final design are illustrated in Fig. 3.14 and 3.15. Fig. 3.14 presents the Von Mises Equivalent Stress contours for the 60 kW EESM rotor operating at 10,000 rpm and 50 Nm torque. The primary image provides a full view of the rotor, with stress levels represented by a gradient color scale ranging from blue (indicating low stress) to red (indicating high stress), covering values from 0 to 230 MPa. The

stress distribution highlights how mechanical loads are distributed across the rotor during operation, with areas of high stress clearly visible near critical structural regions. Two zoomed-in views focus on the specific rotor sections experiencing the most significant stress levels. The first zoom-in highlights the dovetail area, which connects the rotor to the shaft. This region shows elevated stress concentrations due to the combined effects of centrifugal forces at high speeds and the torque transmission between the rotor and shaft. The second zoom-in focuses on the pole shoe termination, a structural feature designed to retain the rotor active conducotrs. This area also experiences significant localized stresses, attributed to the pressure exerted by the copper conductors pushed by the centrifugal forces.

Fig. 3.15 shows a full view of the rotor with deformation levels represented by a color scale ranging from blue (minimal deformation) to red (maximum deformation). The deformation values are measured in meters and range from 9.23×10^{-7} m to 1.53×10^{-5} m, as indicated on the accompanying legend. As expected, the maximum deformation occurs in the rotor conductors, which are

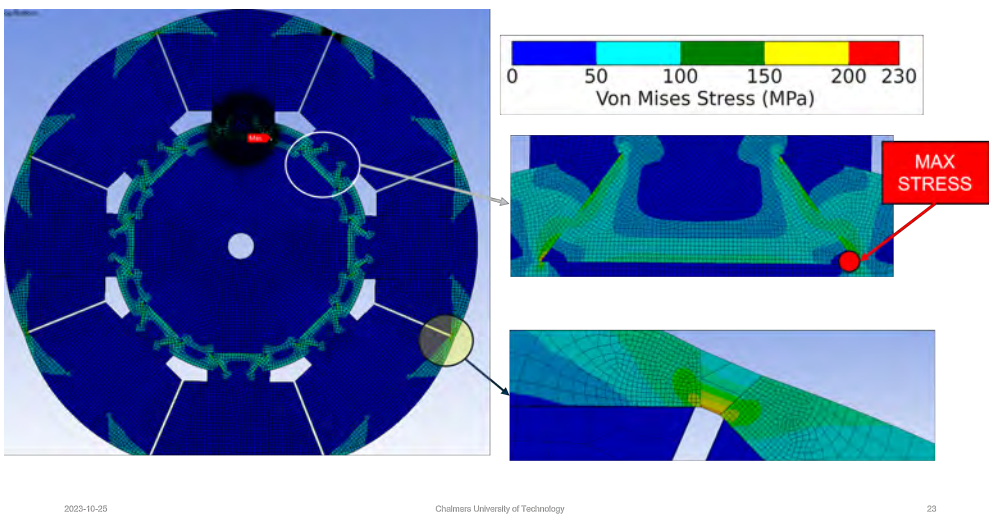

Figure 3.14: Von Mises Equivalent Stress contours of the 60 kW EESM rotor at 10000 rpm and 50 Nm Torque. The zoom-in show the two rotor parts with the highest stress values: the dovetail and the pole shoe termination.

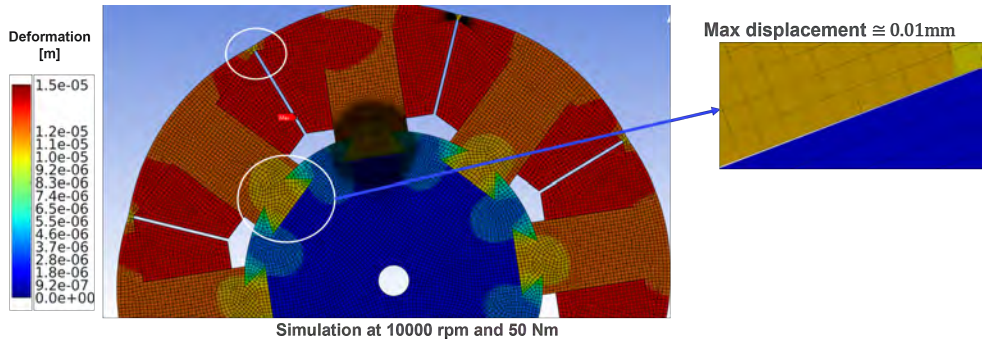

Figure 3.15: Deformation and displacement contours of the 60 kW EESM rotor at 10000 rpm and 50 Nm Torque. The zoom-in shows the maximum displacement due to the relative movement between the two parts of the dovetail joint.

subjected to significant centrifugal forces. These forces generate stress against the surrounding lamination, resulting in deformation of the rotor pole shoe. The zoomed-in view highlights the region of maximum displacement, measured at approximately 0.01 mm, caused by the relative movement between the two parts of the dovetail joint. This movement is driven by the high-speed operation, where the centrifugal forces attempt to separate the components of the joint.

Fig. 3.16 illustrates the evolution of stress components over time from the simulations, with reference lines indicating the rotor lamination material strength limits. The x-axis represents time in seconds, while the y-axis shows stress levels in MPa. The curves track three key stress metrics—Maximum Equivalent Stress, Maximum Shear Stress, and Normal Stress—alongside two critical thresholds: the Tensile Yield Strength at 300 MPa and the Tensile Ultimate Strength at 450 MPa. The Maximum Equivalent Stress, represented by the purple curve, increases rapidly during the initial 10 seconds before stabilizing around 300 MPa. This value aligns closely with the Tensile Yield Strength but remains safely below the Tensile Ultimate Strength, ensuring the rotor material does not reach the point of catastrophic failure. The Normal Stress, shown in yellow, follows a similar trend, rising sharply before stabilizing at approximately 200 MPa, well below both strength thresholds. The Maximum Shear Stress, represented by the red curve, increases more gradu-

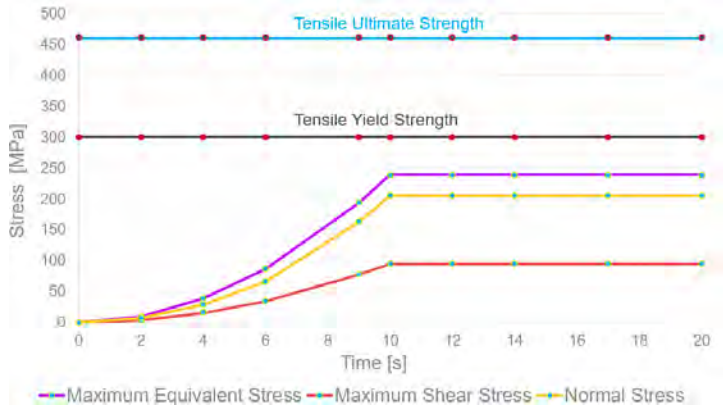

Figure 3.16: Stress simulation results over time at 10,000 rpm and 50 Nm, showing Maximum Equivalent, Shear, and Normal Stresses remaining below the Tensile Yield Strength (300 MPa) and Tensile Ultimate Strength (450 MPa), ensuring no plastic deformation or failure.

ally and stabilizes at around 100 MPa, remaining significantly lower than the material's yield and ultimate strength limits.

Importantly, all three stress components remain below both the Tensile Yield Strength and the Tensile Ultimate Strength of the lamination material throughout the operation. This confirms that the rotor operates without

Table 3.2: Von Mises Max Stress and Max Deformation of the final rotor design

Time [s]	T [Nm]	n [rpm]	Max Stress [MPa]	Max Def. [m]
2	50	2000	9.8	7.83E-07
4	50	4000	38.8	2.72E-06
6	50	6000	87.0	5.80E-06
8	50	8000	193.7	1.25E-05
10	50	10000	238.7	1.54E-05
12	50	10000	238.7	1.54E-05
14	50	10000	238.7	1.54E-05
17	50	10000	238.7	1.54E-05
20	50	10000	238.7	1.54E-05

exceeding its elastic limits, ensuring no plastic deformation or breakage occurs during high-speed operation.

The quantitative values of the maximum total equivalent stress and maximum deformation, obtained from the FEM mechanical simulations for the final rotor design, are presented in Table 3.2. It can be seen that the maximum value of Von Mises Stress across all the rotor lamination is equal to 238.7 MPa at 10000 rpm and 50 Nm whereas the maximum value of deformation for the lamination is equal to 1.54×10^{-5} mm.

Experimental Verification

The 60 kW EESM is manufactured to conduct experiments aimed at validating the electromagnetic model developed through simulations. The manufacturing process is illustrated in Fig. 3.17. In Fig. 3.17(a), the manufactured stator, which is based on a previous design, is shown. Fig. 3.17(b) depicts the shaft alongside the laminated rotor core, which is stacked to form the rotor poles. In Fig. 3.17(c), a completed rotor pole is displayed, showing the conductors wound around the rotor and the glass fiber bandage applied to secure the conductors during high-speed rotation, preventing them from flying out. Finally, Fig. 3.17(d) presents the fully assembled rotor, with the rotor poles mounted onto the shaft, completing the manufacturing process. The machine is tested back-to-back with another machine (PMSM) of similar size and similar maximum power. The layout of the complete test setup is shown in Fig. 3.18 where one EESM (on the left) and one PMSM (on the right) can be seen back-to-back connected. An analog torque transducer is assembled in the middle, measuring the shaft torque. The EESM and PMSM are driven by one three-phase converter respectively. The two converters are powered by the same DC-power supply. During the testing, one machine works under the motor mode, while the other machine works under the generator mode. In this way, the DC power supply only needs to provide the losses of the complete system.

First, the EESM is tested at no-load condition to verify a correct design and dimensioning of the excitation system. In Fig. 3.19 presents a comparison between experimental and simulation results of the no-load line-to-line back-EMF plotted as a function of the rotor position in electrical degrees. Two scenarios are shown, corresponding to two values of field currents equal to 2 A and 3 A. In subfigure (a), the back EMF waveforms for phases AB, BC, and CA are displayed with a field current of 2 A. The experimental results, represented by dashed lines, are compared to the simulated results shown as solid lines. The strong alignment between the two sets of waveforms validates the accuracy of the electromagnetic model in predicting the back EMF behavior of the motor. Subfigure (b) shows the back EMF waveforms for the same phases at a higher field current of 3 A. As expected, the amplitude of the back EMF increases with the field current, and the experimental and simulation results again exhibit close agreement, demonstrating the reliability of the model under another excitation conditions. In both subfigures, the

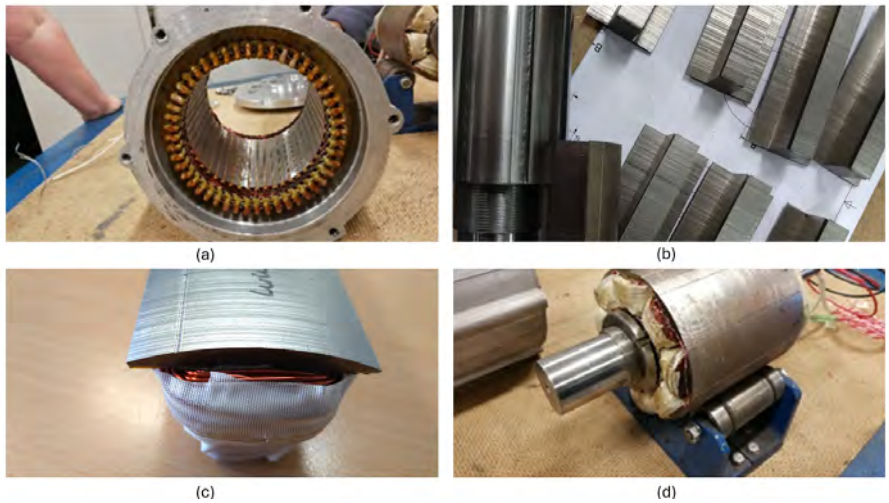

Figure 3.17: Manufacturing of the 60 kW EESM: (a) stator; (b) rotor lamination and shaft; (c) rotor pole; (d) rotor final assembly.

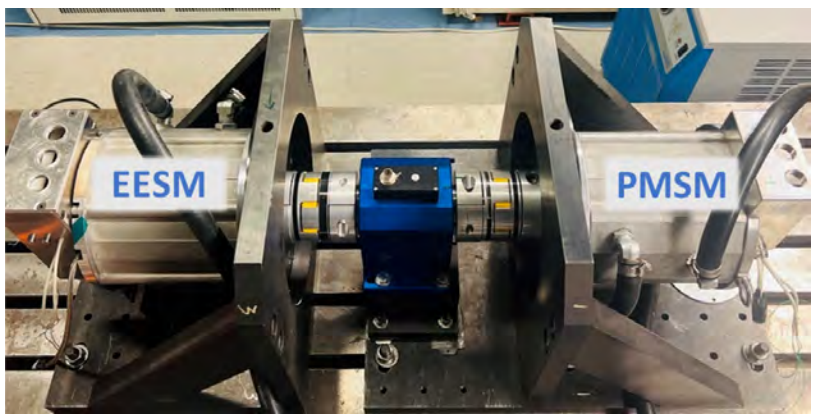

Figure 3.18: Back-to-back experimental setup

waveforms maintain symmetry and periodicity across a full electrical cycle, indicating a well-balanced and precise design.

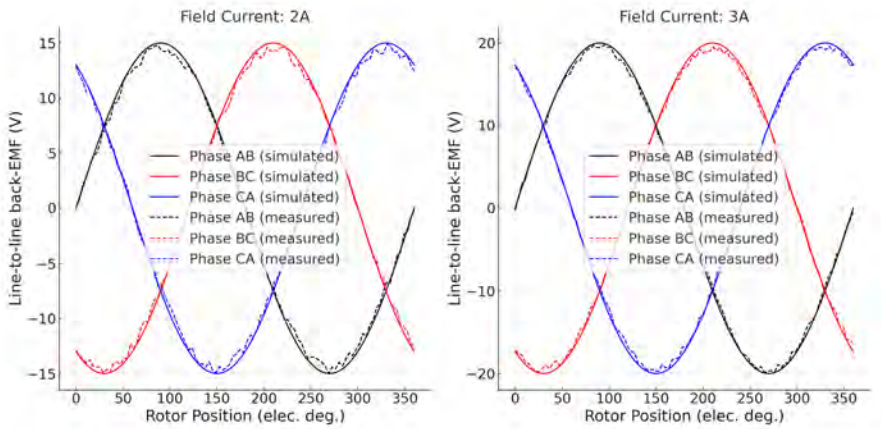

Figure 3.19: Comparison of no-load back EMF measurements between the three stator phases with simulation results for two different rotor current values.

Fig. 3.20 compares efficiency values obtained through simulation (blue line) and experimental measurements (orange crosses) across various operating points. The measured and calculated points are listed in Table 3.3, with the quantities defined as follows: T and n represent the imposed and measured torque and speed, respectively; P_{stator} denotes the input power to the stator as calculated from measurements; P_{rotor} indicates the input power to the rotor derived from experiments; P_{tot} represents the total input power determined from measurements; P_{out} refers to the output power obtained through measurements; η signifies the measured efficiency; η_{sim} describes the efficiency predicted by the simulation model; and T_{sim} corresponds to the torque calculated from the simulation.

While the general trend of the simulated results aligns closely with the experimental data, notable deviations are observed at certain points.

For operating points 1 to 4, the experimental measurements consistently fall below the simulated values, with a maximum deviation of approximately 5%. This discrepancy may be attributed to factors such as unmodeled losses (e.g., stray losses, friction, or windage) or inaccuracies in thermal modeling

that affect efficiency during experimental testing. At point 6, the experimental efficiency is higher than the simulated result, possibly indicating an overestimation of certain loss components, such as copper or core losses, in the simulation.

At higher operating points (e.g., 8 to 10), the simulation closely matches the experimental values, suggesting improved accuracy of the model in those regions. These observations underline the importance of refining the simulation model, particularly for lower operating points, to account for nonlinearities and unmodeled losses, thereby enhancing the prediction accuracy across the entire operating range.

After the manufacturing and the testing, Table 3.4 summarizes some of the final design parameters of the 60 kW EESM. This motor is designed for high performance, focusing on compactness and robust operation. The maximum stator current amplitude is 300 A, while the rotor current is limited to 25 A, ensuring sufficient excitation and torque generation during peak load conditions. The motor achieves a maximum torque of 210 Nm and a power output of 60 kW, making it suitable for applications requiring both high power and torque density. The design demonstrates a strong emphasis on compactness, as reflected in its power and torque density metrics. The calculated power

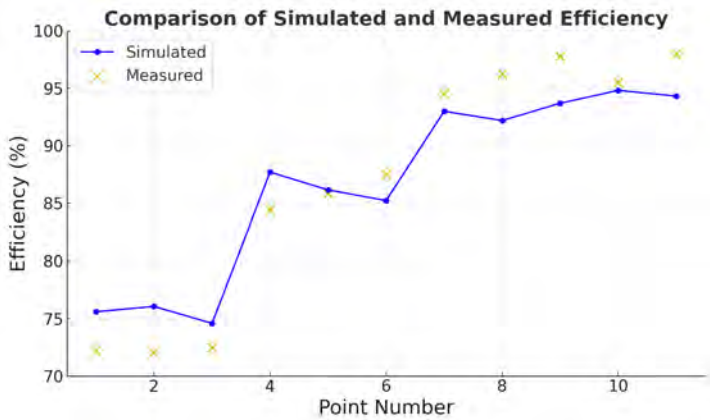

Figure 3.20: Comparison of simulated and measured efficiency values for a 60 kW EESM The simulated efficiency values (blue line) are compared against experimental data (orange crosses) across 10 operating points.

Table 3.3: 60 kW EESM Experimental and Simulation Results

Point	T (Nm)	n (rpm)	P_{stator} (kW)	P_{rotor} (kW)	P_{tot} (kW)	P_{out} (kW)	η (%)	η_{sim} (%)	T_{sim} (Nm)
1	20.0	500	1.36	0.09	1.45	1.05	72.22	75.60	20.0
2	30.0	500	2.01	0.17	2.18	1.57	72.05	76.07	30.0
3	39.6	500	2.64	0.22	2.86	2.07	72.50	74.59	40.0
4	20.0	1000	2.38	0.09	2.48	2.09	84.45	87.71	20.0
5	30.0	1000	3.50	0.17	3.66	3.14	85.84	86.16	30.0
6	39.6	1000	4.52	0.22	4.74	4.15	87.49	85.23	40.0
7	19.5	2000	4.23	0.09	4.32	4.08	94.54	93.01	20.0
8	29.5	2000	6.25	0.17	6.42	6.18	96.24	92.20	30.0
9	38.2	2000	7.96	0.22	8.18	8.00	97.81	93.71	40.0
10	19.1	3000	6.20	0.09	6.29	6.01	95.50	94.83	20.0
11	30.0	3000	8.97	0.17	9.14	9.42	98.01	94.33	30.0

density is 6.96 MW/m^3, showcasing the efficient utilization of motor volume for energy conversion. Furthermore, the torque density is 24.36 Nm/m^3, indicating the motor capability to deliver significant torque relative to its size.

Table 3.4: 60 kW EESM Final Design

Parameter	Value	Unit
Maximum Stator Current Amplitude	300	A
Maximum Rotor Current	25	A
Maximum Torque	210	Nm
Maximum Power	60	kW
Maximum Power density	6.96	MW/m^3
Maximum Torque density	24.36	Nm/m^3

3.6 Thermal Analysis in Steady State

Electrically Excited Synchronous Machines have drawn interest due to their exceptional performance attributes, though they pose notable thermal management issues. The rotor, equipped with active conductors, experiences a high density of loss and considerable heat generation, which has been a barrier to the broader use of this machine in various applications. This study explores the practicality of employing a 60 kW EESM in a commercial vehicle application, particularly by examining its thermal behavior. A steady-state 3D Conjugate Heat Transfer (CHT) analysis is utilized to assess the temperature distribution in different machine components over the torque-speed map. Following this analysis, thermal resistances are estimated from the CHT model to build a simplified Lumped Parameter Thermal Network (LPTN), aimed at forecasting the maximum temperatures during the Worldwide harmonized Light-duty vehicles Test Cycles (WLTC). MATLAB Simulink simulations reveal that temperatures stay within the safe bounds defined by the winding insulation class throughout the driving cycle, ensuring reliable and secure operation of the EESM for the intended application.

Loss Model

The electromagnetic motor losses serve as primary inputs for the CHT model. Key losses include the AC and DC copper losses in the stator winding, the DC copper loss in the rotor field winding, and the stator iron core losses. Electromagnetic simulations utilizing the Finite Element Method (FEM) are executed in ANSYS Maxwell to assess the losses across varying operating points along the machine torque-speed characteristic, as describer in the previous sections. The following steps outline the loss calculation:

- FEM transient electromagnetic simulations are conducted at various levels of stator and rotor current magnitudes while maintaining the motor at base speed. This generates a dataset of flux linkages and core losses.
- The optimization algorithm for minimizing copper losses (Maximum-Torque per Ampere) is implemented as explained in [41], utilizing the flux linkage map from the previous step. The output provides current and inductance values along the d- and q- axes for calculating the machine torque.

- The copper losses are computed as in equations (3.11) and (3.10).

Figure 3.21 illustrates the computed losses as contours on the EESM torque-speed map. The most prominent losses are in the stator copper, peaking at high power and speed levels, influenced by AC losses that rise with frequency. Rotor copper losses contribute significantly, peaking along the torque-speed envelope that matches the highest field current magnitude. The smallest losses are those in the stator iron core, purely dependent on frequency. Note that in this study, rotor core losses are disregarded due to their minimal impact and localization on the rotor surface, stemming from stator slot harmonics.

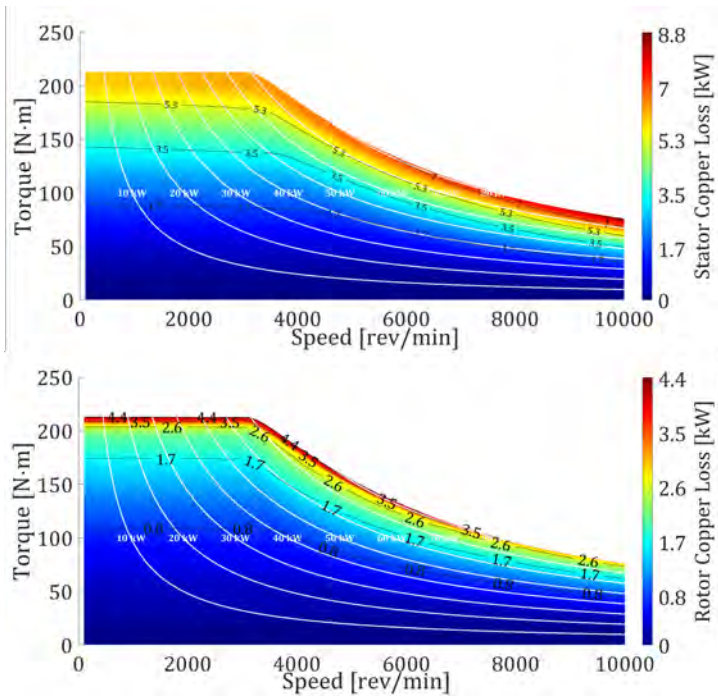

Figure 3.21: Stator and rotor copper loss calculated from FEM and used as inout for the CHT model.

CHT Model

The EESM model utilized for the CHT simulation is a 3D model that faithfully accounts for all primary components and insulating materials. To minimize the number of mesh cells, only one-eighth of the motor geometry is imported into Ansys Fluent, along with the fluid domains. The solid parts, illustrated in Fig. 3.22, include the stator lamination, rotor lamination, shaft, bearings, housing, rotor winding, and stator winding.

Each stator hairpin and rotor conductor is incorporated without simplifications in the model. To reduce mesh complexity, insulation is not represented as solid elements; instead, they are modeled as boundary conditions on the conductor surfaces via *Shell Conductions* in Fluent, specifying the material properties and thickness of the insulation, as detailed in [43]. The thermal conductivity and specific heat for each machine component are presented in Table 3.5. Beyond insulating materials, additional factors act as thermal barriers within the machine. The accuracy of thermal performance predictions depends significantly on estimating the other numerous thermal contact resistances present in electrical machines [44]. These resistances arise from surface imperfections and are influenced by factors such as material hardness, interface pressure, surface smoothness, and air gaps.

For the common material interfaces found in electric machines, air interface gap values range as follows: aluminum-aluminum between 0.0005 and 0.0025 mm, stainless-stainless from 0.007 to 0.015 mm, aluminum-stainless from 0.006 to 0.009 mm, and aluminum-iron between 0.0006 and 0.006 mm. These air gaps are included in this study using *Shell Conductions*.

The CHT model also includes Computational Fluid Dynamics (CFD), where all fluid domains are represented: the air inside the motor, the water cooling jacket, and the surrounding external air. To simulate rotation, the rotor lamination and winding surfaces in contact with the air are set in motion via the *Frozen Rotor* approach [43]. This method addresses Coriolis and centripetal accelerations when *Frame Motion* is enabled, allowing for rotor rotation in a steady-state simulation, thereby avoiding the need for costly transient simulations.

As an example, Fig. 3.23 presents results from the CHT model for a simulation with input losses at a torque of 50 Nm and a rotor speed of 10,000 rpm. The top image shows the axial temperature distribution across the machine cross-section, highlighting variations in temperature across the winding, stator

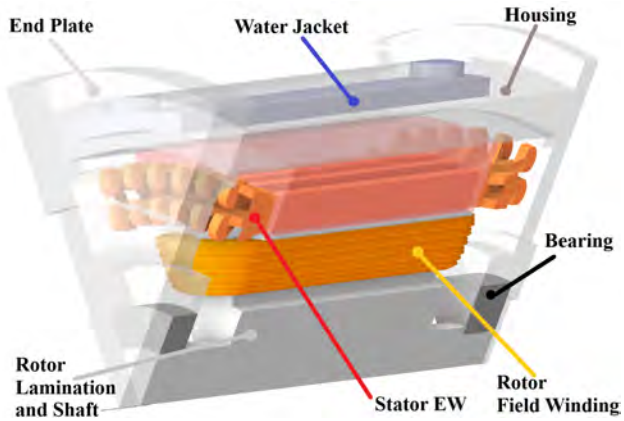

Figure 3.22: Tridimensional geometry representing one-eighth of the machine used for the CHT model.

Table 3.5: Thermal Properties of Machine Components

Component	Thermal Conductivity [W/mK]	Specific Heat [J/(kg K)]
Housing	168	833
Lamination (radial)	35	460
Lamination (tangential)	34	460
Shaft	50	460
Copper	387.6	381
Enamel	0.5	1700
Slot Liner	0.18	1000
Air Pockets	0.0242	1006.43

core, and housing. The bottom image displays the radial temperature distribution within the rotor and its surrounding components. The color gradients represent static temperatures in degrees Celsius, as indicated by the accompanying color bar. In both views, the highest temperature is observed within the rotor winding, which has the highest volumetric loss density. Specifically, the hotspot is located in the central section of the field end winding, where heat transfer through the lamination path is constrained, and convection is limited due to reduced airflow in this region.

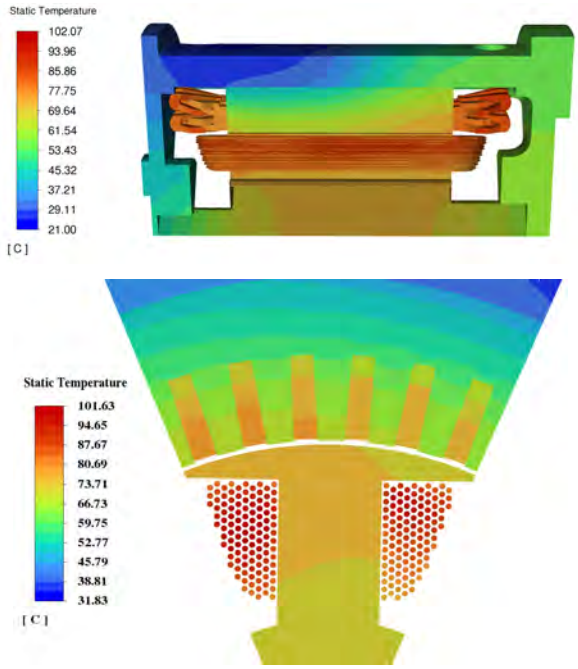

Figure 3.23: Temperature distribution contours inside the motor at 50 Nm and 10000 rpm in steady state, shown along axial and radial directions.

Moreover, the motor temperature distribution is asymmetrical for two main reasons. Firstly, the water jacket temperature remains near 60° closer to the inlet, where more fresh, temperature-controlled water is pumped. Secondly, the rotor rotational direction creates a temperature difference impacting in the temperature gradient of the rotor conductors.

3.7 Thermal Performance Evaluation in Driving Cycle

A lumped parameter thermal network (LPTN) is developed to obtain rapid temperature responses of the machine under transient conditions. A primary

challenge in implementing a thermal network is accurately estimating the thermal parameters, particularly the numerous contact resistances within the machine. The CHT model is utilized to estimate thermal resistances under steady-state conditions, which are then imported into the LPTN. The LPTN is then used to run driving cycle simulation in MATLAB Simulink in reasonable times to verify the feasibility in using the 60 kW Concept EESM for a vehicle drivetrain.

Lumped Parameters Thermal Network

A lumped parameter thermal network is constructed by simplifying the EESM numerous components into thermal nodes, each assigned a specific temperature. To incorporate the thermal inertia of each component, thermal capacitances are allocated, representing each component heat storage and release capacity, which can be calculated from the mass m and specific heat c_i of each i machine component:

$$C_i = m_i \cdot c_i \tag{3.18}$$

Additionally, to account for interfaces between materials with different thermal conductivities, contact resistances are assigned between all thermal nodes, as illustrated in the schematic in Fig. 3.24. The figure illustrates the cross-sectional view of an EESM, with annotations highlighting the primary structural and thermal components. The stator lamination (S) forms the core of the stator, while the stator active winding (SW) represents the active part of the stator conductors whereas the SEW denotes the stator end windings. Similarly, the rotor consists of the rotor lamination (R) and the rotor active winding (RW), with the rotor end winding (REW) extending beyond the main structure. Surrounding these active components is the housing (H) aided by the water jacket (WJ) for liquid indirect cooling and the shaft (SH) at the center of the motor. The thermal resistance paths $(R_1, R_2, \ldots, R_{12})$ illustrate the heat flow between these components whereas the ambient (A), represents the heat transfer towards the surrounding environment. These contact resistances represent heat flow barriers at the interfaces and are crucial for determining heat transfer between adjacent components. Complex geometries involve irregular shapes, multiple materials, variable contact areas, and non-uniform heat distribution, complicating accurate thermal resistance

determination. This study proposes estimating thermal resistances by utilizing the maximum temperatures of interfacing components and total heat flux across interface surfaces derived from the steady-state CHT model. Using this information, various thermal resistances can be calculated as follows:

$$R_{\mathrm{i},j} = \frac{T_{\mathrm{max},i} - T_{\mathrm{max},j}}{q_{ij}} \tag{3.19}$$

where $T_{max,i}$ and $T_{max,j}$ are the maximum temperatures of components i and j, while q_{ij} represents the total flux across the interface surface between i and j.

The thermal network used to estimate the maximum temperatures of the EESM components is shown in Fig. 3.25, while all thermal resistances caclulated from the CHT model and included in the LPTN are illustrated in Fig. 3.26 and Fig. 3.27 as function of motor speed and for different total input losses.

The cooling effect of rotor rotation on the air gap surface and terminal parts

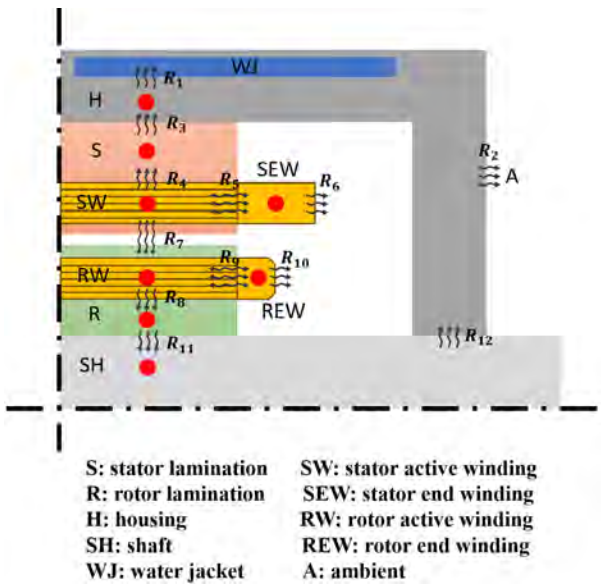

Figure 3.24: Schematic of the 60 kW EESM lumped parameter thermal network for one-fourth of the motor.

of the stator and rotor windings is incorporated into the thermal network using variable resistances, as their values depend on rotor speed, as shown in Fig. 3.27. Among these, the resistances that exhibit the most significant speed dependency are those related to the heat transfer between rotating surfaces and the surrounding air, specifically, the resistances associated with the air gap R_7 and the field winding R_{10}. These resistances show a decreasing trend following a hyperbolic curve. On the other hand, the resistance R_6, which accounts for the variable heat exchange between the air and the stationary end winding of the stator, is only indirectly affected by the rotation of the machine. As a result of this factor, there is only a slight variation observed when increasing the EESM speed. The other thermal resistances between solid components are shown in Fig. 3.26.

Theoretically, certain resistances, such as those at the interface between solid and stationary components, may not be expected to vary significantly with input losses or rotor speed alone. However, in a complex network of

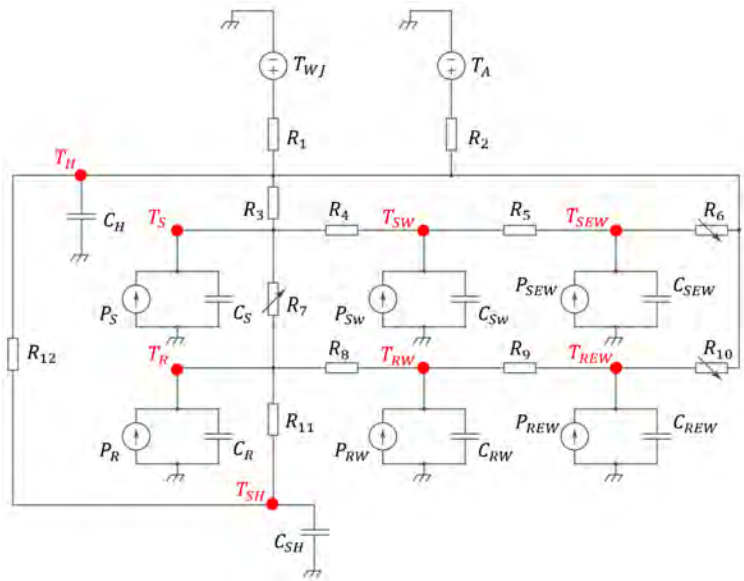

Figure 3.25: Simplified Lumped Parameter Thermal Network (LPTN) with thermal resistances derived from the CHT model for maximum temperature estimation (red dots).

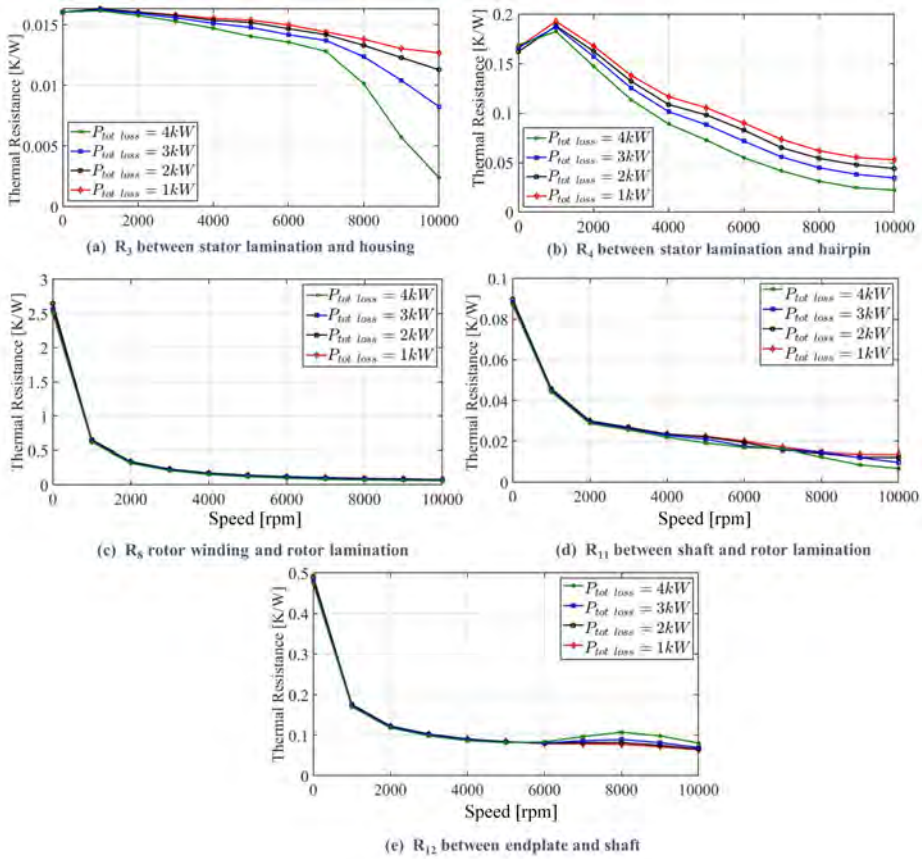

Figure 3.26: Thermal resistances at the interface between solid components of the 60 kW Concept EESM as function of rotor speed and for different values of total input losses.

interdependent components, any parameter variation can alter the heat flux and temperature distribution across the system. Notably, almost all resistances display significant rotor speed dependence, dropping over 85% from their maximum values as rotation increases. This speed dependency is most pronounced at low speeds and becomes less noticeable as speed reaches higher levels, eventually stabilizing. The resistances that show the highest variation

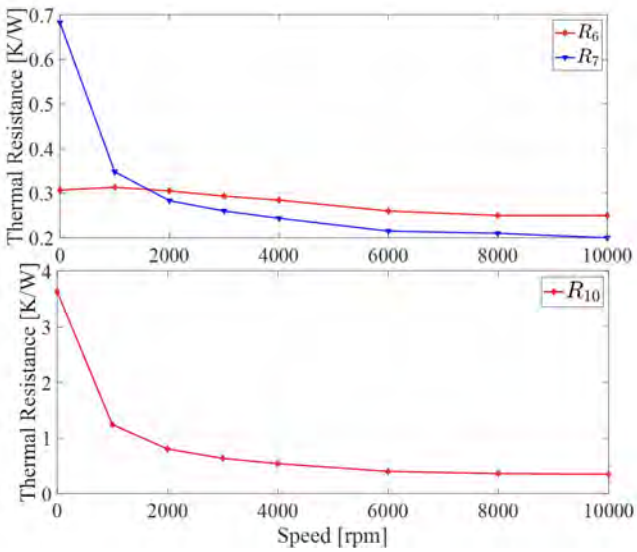

Figure 3.27: Thermal resistances at the interface between solid components and air of 60 kW EESM as function of rotor speed and for different values of total input losses.

include R_4, R_8, and R_{12} which represent the resistance between stator lamination and hairpin conductors, between rotor lamination and rotor winding, and between end plates and shaft.

Although input losses have minimal impact on resistance values, a slight decrease is observed with increasing losses. Of all resistances, R_8 stands out as the largest. This is due to the dovetail mounting of poles on the shaft, which creates a notable air gap between components, increasing resistance within the cooling system.

Vehicle Model and Machine Requirements

The motor that is analyzed in this study is a 60 kW EESM designed for a D-class vehicle. Vehicles in this category typically have an overall length of 4400-4800 mm, a top speed ranging from 180-210 km/h, and an acceleration time from 0 to 100 km/h of 8.5-13 s. A simplified vehicle model is applied to determine the machine torque and speed using the vehicle speed profile from

the WLTC. The resistive force exerted on the vehicle is defined as:

$$F_r = \frac{1}{2}\rho C_d A v^2 + mg\sin\alpha + mgC_r \tag{3.20}$$

where m denotes the vehicle mass, v is the speed of the vehicle, C_d is the aerodynamic drag coefficient, C_r is the rolling resistance coefficient, g represents gravitational acceleration, and α is the road gradient angle.

The traction force can be determined based on the resistive force as:

$$F_t = F_r + m\frac{dv}{dt} \tag{3.21}$$

The traction torque required by the drivetrain can be expressed as:

$$T_w = F_t r_w \tag{3.22}$$

where r_w is the radius of the wheel.

Using the vehicle model and the WLTC, the torque and speed requirements for the EESM in a D-class BEV are determined. The WLTC test cycle is known to vary depending on the vehicle class, which is defined by the Power-to-Weight Ratio (PWr) in W/kg. For this analysis, the chosen test cycle is Class 3, representing high-power vehicles with a PWr exceeding 34 W/kg.

In Fig. 3.28, the torque-speed characteristics of the reference 60 kW EESM in both the first and fourth quadrants are shown by the black line. The pink markers represent the torque and speed demanded by the machine of the D-class BEV during the WLTC. It can be observed that all the operating points required by the vehicle's drivetrain lie within a region where torque values are consistently below 100 Nm, in both motoring and braking modes. However, the speed range is extensive, covering the entire spectrum from minimum to maximum speed.

3.8 Thermal Analysis Results

The results from both the steady-state Conjugate Heat Transfer model and the transient Lumped Parameter Thermal Network are presented for the 60 kW machine under investigation. The steady-state results are depicted as temperature contour plots over the machine torque-speed map, providing a clear visualization of the thermal limits for various components during con-

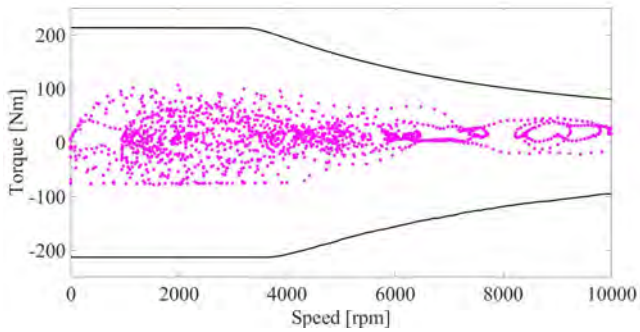

Figure 3.28: Reference machine specifications and requirements: the black line indicates the torque-speed characteristics of the reference 60 kW EESM, while the pink markers show the torque and speed demands during the WLTC for a D-class BEV.

tinuous operation. In contrast, the transient results are presented using the WLTC driving cycle, illustrating the estimated temperature evolution under realistic operating conditions over a 3500-second period. These complementary analyses provide valuable insights into the machine thermal performance under both steady and dynamic scenarios.

Steady-State Temperature Maps

A comprehensive set of simulations is conducted using the CHT model at various values of losses and rotor speeds corresponding to different points within the machine torque-speed characteristics. Figure 3.29 presents the simulation results as temperature maps, where the maximum temperatures of each of the machine components are shown for all the possible operating point. In each map, the colormap maximum temperature is set to 180°C, which aligns with the insulation class limit for the stator and rotor windings. Exceeding this temperature threshold for laminations or conductors could result in machine failure. Accordingly, all regions with temperatures reaching or surpassing 180°C are highlighted in red. The temperature maps also feature pink dots that mark the required operating points for the D-class vehicle during the WLTC test cycle. This enables a visual comparison between machine temperature limits and vehicle requirements on a single graph.

It is crucial to note that these temperature maps depict steady-state temperatures, signifying machine operation at a given point for extended durations, potentially lasting hours. In contrast, the WLTC points represent moments where the machine functions briefly, typically lasting from seconds to minutes. Unlike the steady-state temperatures, these points illustrate machine behavior during transient conditions that occur throughout the test cycle.

Among the maps, the rotor winding displays the largest red zone, indicating that it experiences the highest temperatures among all machine components. Following closely are the stator end winding and active conductors, which also exhibit notable high-temperature regions. The active portion of the stator winding benefits from direct contact with the stator lamination, which assists in heat dissipation and helps to moderate its temperature. In contrast, the end windings are surrounded by air, creating a heat flux barrier that limits

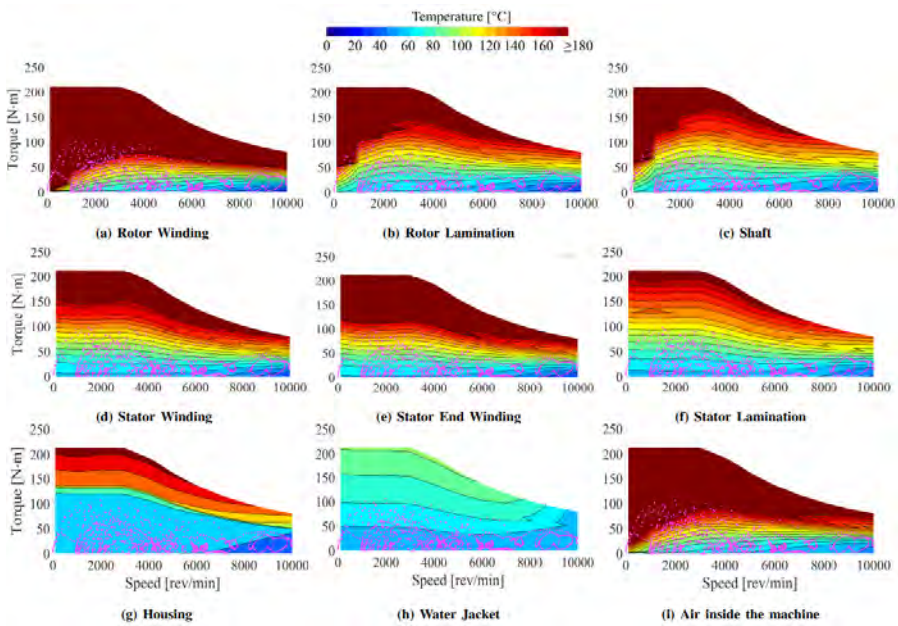

Figure 3.29: Contours of maximum temperature in steady-state of the machine components along the EESM torque-speed characteristics. The pink dots represent the required machine operating points for a D-class BEV during the standard WLTC test cycle.

efficient heat dissipation, resulting in elevated temperatures. Regarding the rotor lamination and shaft, their peak temperatures are similar, heavily influenced by the rotor winding temperature as the field conductors are wound around the rotor poles. However, a minor difference between rotor lamination and shaft temperatures exists due to the interface gap between them, which restricts heat transfer, yielding a slightly lower shaft temperature than the rotor lamination.

Most driving cycle points fall within the machine's permissible operating range, demonstrating the EESM's capability to continuously function at these points, underscoring its thermal reliability for this specific application.

Driving Cycle Simulations Results

The torque and speed profiles of the EESM obtained from the WLTC driving cycle are shown in Fig. 3.30. The top plot illustrates the torque demand over the 3500-second cycle, with values ranging from approximately -100 Nm to +100 Nm. The frequent and abrupt changes in torque reflect the varying load conditions experienced during real-world driving, with more pronounced torque spikes observed in the first half of the cycle, corresponding to acceleration phases. The bottom plot shows the rotor speed profile, which varies between 0 and a peak of nearly 10,000 rpm. The speed gradually increases throughout the cycle, with high-speed operation occurring intermittently after 1000 seconds. These torque and speed profiles provide realistic operating conditions for estimating the thermal behavior of the machine components through transient simulation.

Fig. 3.31 presents the maximum temperature results obtained from the Lumped Parameter Thermal Network LPTN for key EESM components over the 3500-second WLTC simulation. The stator winding and stator end winding temperatures are shown in the top plot, where the stator end winding exhibits a peak temperature of approximately 120°C, while the stator winding reaches a slightly lower peak of 100°C.

The stator end winding also experiences greater temperature fluctuations, indicating higher localized heat generation due to reduced heat dissipation efficiency. The middle plot shows the rotor winding and rotor end winding temperatures, where the rotor end winding reaches the highest temperatures in the machine, with brief spikes up to 175°C, while the rotor active winding follows closely, maintaining a temperature approximately 20°C lower than

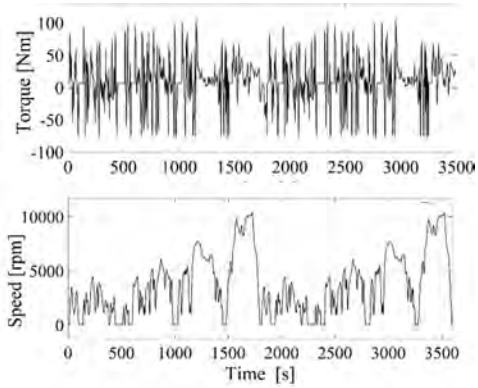

Figure 3.30: Torque and speed of EESM obtained from the WLTC test cycle.

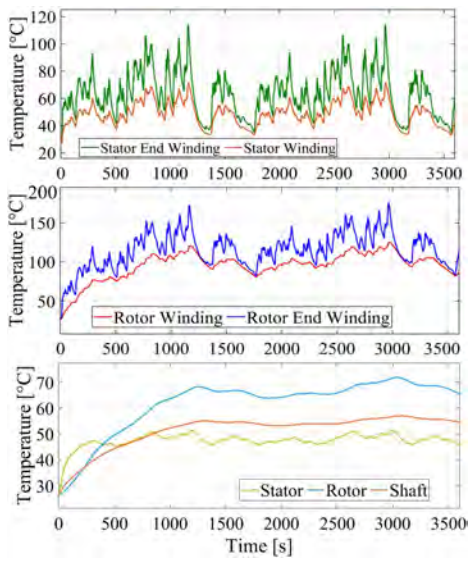

Figure 3.31: Maximum temperature results in transient condition obtained from the LPTN for various EESM components.

the rotor end winding throughout the cycle. These results emphasize that the rotor end winding is the most thermally stressed component. The bottom plot

shows the temperatures of the stator core, rotor core, and shaft. The stator core reaches a peak temperature of approximately 80°C, while the rotor core and shaft remain below 60°C. The rotor core shows minor fluctuations due to transient thermal loads, whereas the shaft maintains a relatively stable temperature, confirming its low thermal susceptibility.

Overall, the results demonstrate that the machine operates within the insulation class limit of 180°C. Despite transient high torque and current demands, temperature rises are brief and localized, particularly in the rotor end winding. This is attributed to the active sections of the conductors being connected to the lamination, which enhances heat dissipation. These findings validate the machine ability to maintain safe thermal performance under dynamic and realistic driving conditions.

CHAPTER 4

Cooling of 200 kW Prototype EESM

Once the 60 kW Concept EESM was successfully designed, manufactured, and tested, the same approach was adapted to design a full-scale machine: the 200 kW prototype EESM intended for long-distance heavy-duty trucks.

One of the primary challenges in designing an EESM for truck applications lies in meeting the high power demands over extended periods. For this reason, a key focus is maintaining the rotor conductors within a specified temperature range through an efficient cooling system. The presence of active conductors within the rotating part of the machine significantly increases the complexity of implementing both direct and indirect cooling systems. As a result, the design of the 200 kW prototype emphasizes the development and implementation of an advanced cooling system, alongside a thorough investigation of the machine thermal behavior.

The electromagnetic design of the 200 kW prototype follows the same principles and criteria established and validated for the 60 kW Concept EESM. For further details regarding the study, machine design, and experimental results, refer to **Paper VI: "Electromagnetic Performance Investigation of a Brushless Electrically-Excited Synchronous Machine for Long-Distance Heavy-Duty Electric Vehicles."**

4.1 Thermal Requirements for Truck Drives

The aim of this study is to explore the use of the 200 kW EESM in high-power-density applications, such as those required for trucks. In general, the torque-speed map of electric motors is divided into two primary regions, as illustrated in Fig. 4.1: the red region, referred to as *Peak Operation*, and the blue region, known as *Continuous Operation*.

The *Peak Operation* region represents the operating range where the machine is designed to deliver maximum torque at low speeds for a very short duration, typically from a few seconds to a few minutes. This region is characterized by exceptionally high stator and rotor currents, which can only be sustained briefly due to thermal and design limitations. Prolonged operation in this region is usually not feasible, as it cannot be extended significantly through design improvements or enhanced cooling systems. Conversely, the *Continuous Operation* region is the range in which the machine operates for extended periods during normal driving conditions. This region is characterized by relatively lower torque and higher speeds, ensuring the required power for sustained vehicle operation. In this mode, the stator and rotor currents are kept at moderate levels, allowing the machine to remain in this region

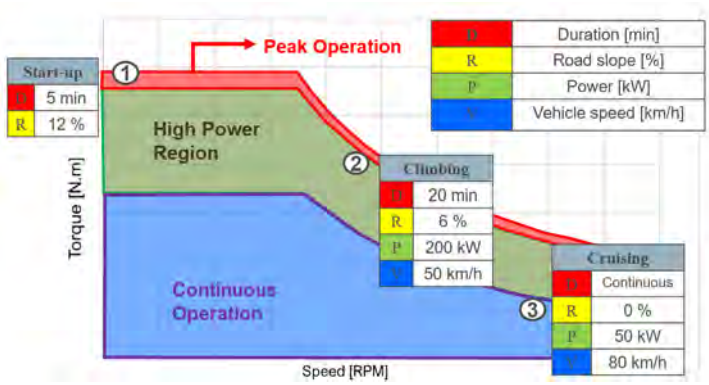

Figure 4.1: Torque-speed map highlighting typical thermal requirements for traction motors: the red region indicates *Peak Operation*, the green region represents the *High Power* range, and the blue region corresponds to *Continuous Operation*. Superimposed are numerical labels representing typical operating points for truck traction motors.

for prolonged durations. Unlike *Peak Operation*, the extent of the *Continuous Operation* region can be significantly expanded through optimal machine design and advanced cooling systems.

Recent advancements in direct oil cooling techniques have notably increased the size of the *Continuous Operation* region, enabling higher power levels, particularly for demanding applications such as trucks. In these scenarios, vehicles often operate in a *High Power* region, characterized by elevated current and voltage levels for extended durations, as shown in Fig. 4.1.

The previously introduced requirements for trucks are illustrated in Fig. 4.1, overlaid on the aforementioned regions. First, there is the *Start-Up* condition, which requires the maximum torque of the motor to accelerate the vehicle from a standstill while on a road with a slope of 12%. *Climbing* represents the maximum power operation and corresponds to driving uphill on a maximum slope of 6%. Finally, *Cruising* refers to highway driving at a constant speed, typical for long-haul trucks, where the vehicle is expected to achieve the best efficiency.

4.2 EESM Cooling Strategies

In EESM the maximum temperature tolerated by the system is imposed by the thermal class of the coil insulation in the stator and the rotor. Commonly, the windings cannot tolerate a higher temperature than 180°C [45] to avoid insulation damage. Inefficient cooling system causes faster insulation degradation reducing the expected life of the machine [46]. Typically, a useful indication is that the temperature rise of 10°C over the material data sheet threshold is expected to reduce the insulation life by half [47]. In order to ensure the temperature below the limits, a good thermal strategy should solve the main challenges from all aspects including the reduction of the heat sources, the choice of optimal materials and the use of high performance cooling system. Electrical machines can be cooled down in approximately 4 ways[48]: (1) air-cooling were the air is moved by an external blower or a shaft-mounted fan [49], [50]; (2) water-cooling [51], [52] in which the water inside ducts at the interface between stator and housing (e.g. water jacket) and kept below certain temperature through an heat exchanger; (3) direct oil-cooling [53] where the high insulation properties of the oil are used to wet directly the conductors enhancing the heat transfer; (4) combined oil- and water- cooling [54] in

which the water with the highest thermal conductivity is used to indirectly cool down the oil inside the motor. The best cooling performance are generally attributed to the combined oil- and water- cooling followed by direct oil-cooling, indirect oil-cooling and air-cooling. Although, the presence of two coolants requires more costs related to the installation and pressurization of two different cooling circuits.

For the above mentioned reasons, direct oil cooling is chosen for the 200 kW EESM in both stator and rotor. The use of oil presents in fact several advantages:

- Oil is already used in automotive to lubricate rotating parts (e.g. bearings, gearbox), so the same oil circuit can be used to supply coolant to the motor and lubricants to mechanical rotating parts such as in Tesla motors [55].
- Oil is a good electric insulator and can be used in direct contact with electric active parts where indirect water cooling is not sufficient due to the high thermal resistance between the winding and the water. In addition, oil can enhance insulation where insulants are damaged due to manufacturing process, e.g. hairpin bending for end winding realization [56], preventing problems like partial discharges.
- The boiling point of oil is higher than water, allowing for applications above 100°C.
- Cooling water should include a corrosion inhibitor, as it can be corrosive to the machine parts and insulation, whereas oil spontaneously prevents corrosion [57].

In this thesis, three distinct direct oil cooling methods are thoroughly investigated: Stator Oil Jacket with end winding Self-Impingement, rotor direct oil cooling, and oil splashing cooling.

Stator Oil Jacket with end winding Self-Impingement employs a hybrid approach. It utilizes indirect cooling via an oil jacket surrounding the active part of the machine, achieved through axial ducts positioned at the interface between the stator and the housing. Simultaneously, it incorporates direct oil cooling for the end windings. This is accomplished by allowing oil from the axial ducts to impinge directly on the hairpin end windings without requiring an additional external oil circuit.

Rotor direct oil cooling, as proposed in this thesis, enables direct contact between the cooling oil and the rotor active winding, lamination, and shaft simultaneously. In this design, the rotor is mounted on a hollow shaft, through which oil is actively pumped, ensuring efficient distribution of coolant throughout the rotor components. This approach operates independently of centrifugal force, maintaining effective cooling performance even at low rotational speeds.

The **oil splashing cooling** involves immersing the rotor either partially or fully in oil. During rotation, the high-speed motion of the rotor causes the oil to circulate dynamically, significantly enhancing heat dissipation. The method feasibility is investigated through detailed evaluation of the heat transfer coefficient and an analysis of mechanical losses caused by oil viscosity.

4.3 Rotor Oil Cooling

The rotor cooling in EESMs can be challenging due to several reasons. First, the rotor winding of EESMs is subjected to high current density, leading to significant heating and a temperature rise. The heat generated in the rotor is transferred to the rotor core and shaft, which are usually made of high-quality magnetic materials such as laminated iron and steel, which have low thermal conductivity and high thermal capacity. This makes it difficult to extract the heat from the rotor and dissipate it effectively.

Second, the rotation of the rotor generates a centrifugal force that tends to push any direct coolant away from the rotor surface, reducing the cooling effectiveness. Furthermore, the rotational motion of the rotor does not allow any level of coolant at the air gap, otherwise the mechanical loss increases exponentially with the machine speed. This chapter details the rotor cooling system design for the 200 kW EESM Prototype intended for truck applications. The system integrates direct cooling of the hollow shaft, rotor lamination, and rotor winding with mineral oil. The design is validated in simulations using the Conjugate Heat Transfer (CHT) approach to assess oil flow and temperature distribution. Experimental tests are conducted on an 8-pole prototype rotor under stationary conditions, with a maximum coil heat loss of 4.7 kW, achieving 8x190 Aturns magneto-motive force per pole at a 9.2 L/min oil flow rate. Results highlight the cooling method's effectiveness in doubling the current density feasible for continuous operation, from 5.05 A/mm^2 to 10.1 A/mm^2, maintaining the Startup condition for over 5 minutes and maximum power for 20 minutes, incorporating the rotor rotation ventilation effect in simulations.

Rotor Design

To achieve a reduction in torque ripple, enhance the fill factor, and prevent conductor displacement, the rotor design incorporates a closed slot configuration. Implementing this closed slot structure presents challenges when trying to fit a large number of conductors within the rotor. To overcome this, a dovetail joint is used to assemble the rotor poles onto the shaft, as illustrated in Fig. 4.2. In this approach, the rotor conductors are initially wound around the poles, which are then mounted onto the shaft using the dovetail joint.
The rotor cooling system is devised to improve heat dissipation from the con-

ductors by directing the oil flow along three main pathways, shown in Fig. 4.3.

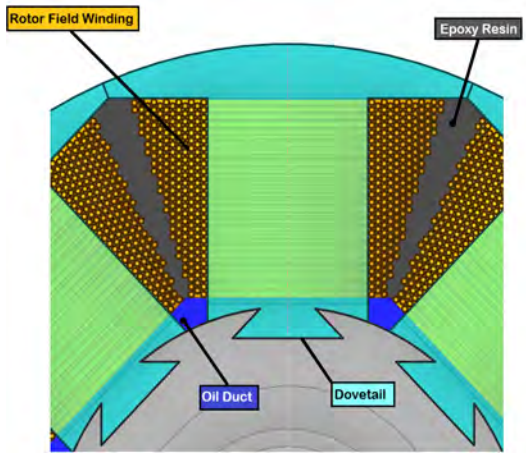

Figure 4.2: Cross section of the rotor slot: the field conductors are wound around the poles up to certain limits due to manufacturing constrains. After the the potting process with epoxy resin, the empty bottom part of the rotor slot is used to derive an axial oil duct.

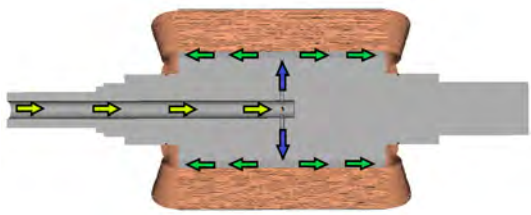

Figure 4.3: Path of the oil inside the rotor cooling system: the oil is pumped through the hollow shaft (yellow arrows), the shaft radial channels (blue arrows) and it flows along the axial channels formed by the empty space at the bottom part of the rotor slots (green arrows).

First, a pump pressurizes the oil, channeling it into the hollow shaft via a rotary joint, as indicated by the yellow arrows. At the shaft end, eight smaller radial channels are formed within the shaft to direct the oil outward, depicted

by blue arrows. This radial oil flow results from both pressurization and the centrifugal force during rotation. Due to manufacturing constraints, it is not possible to fill the space between rotor poles entirely with copper conductors, which leaves room for eight axial channels for oil flow, highlighted by green arrows. Here, the oil makes direct contact with the active conductors at the slots bottom, as shown in Fig. 4.2.

To prevent oil leakage toward the air gap, thermally conductive epoxy fills the rotor slot, aiding in channel shaping and maintaining uniform oil pressure and velocity across all ducts. After flowing through the rotor slot channels, the oil accumulates at the housing base and is directed to the heat exchanger using a suction pump.

Loss Model

Similar to the approach used for the 60 kW Concept EESM, the MTPA algorithm is also employed for selecting the field current in the 200 kW EESM prototype. This reference current selection strategy is designed to minimize total copper losses, encompassing both stator and rotor contributions, as detailed in **thesis**. Rotor losses are computed using a flux linkage-based model of the machine, where a parametric sweep of the rotor field current is conducted through a finite element model (FEM) in ANSYS Maxwell. An iterative optimization technique is then used to select the field current that minimizes total copper losses. The rotor total copper losses and field current across the full torque-speed operating range are illustrated in Fig. 4.4. Observing Fig. 4.1 and Fig. 4.4, it is evident that a maximum field current of 12 A is necessary to satisfy *Startup* and *Climbing* conditions, resulting in a rotor winding loss of 4.7 kW. For *Cruising*, a field current of 5 A suffices, with a corresponding loss of 0.8 kW, which is nearly six times lower.

Steady-State CHT Model

Owing to the geometric symmetry, only one-eighth of the rotor is imported for the analysis, including a single salient pole, one-eighth of the shaft, and all 190 field copper conductors with high-fidelity insulation. The oil channels are extracted from the solid structure and defined as fluid, with the following assumptions applied:

- Due to lamination, the rotor thermal conductivity is considered anisotropic,

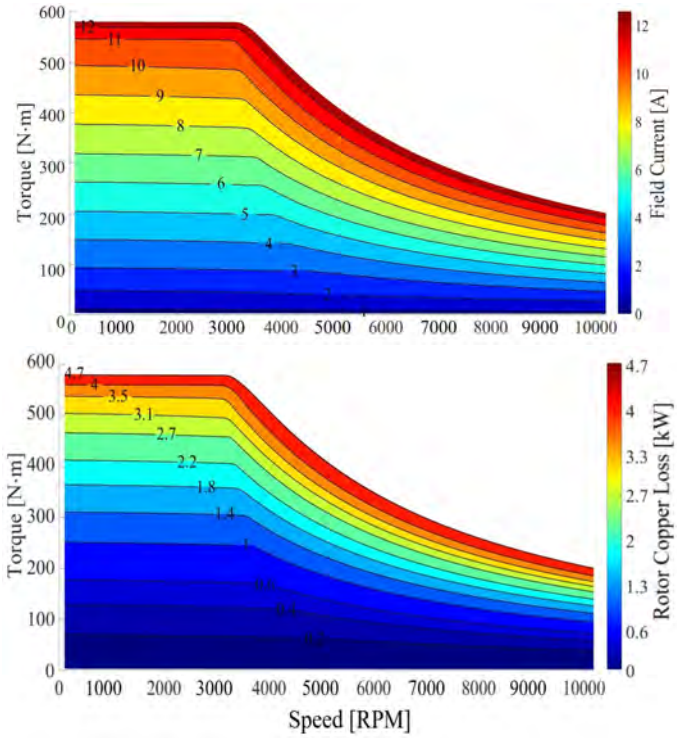

Figure 4.4: Rotor field current and copper loss on the torque-speed plane calculated using FEM and MTPA algorithm.

with all material thermal properties outlined in Table 4.1.

Table 4.1: Thermal Properties of the Machine components

Component	**Thermal Conductivity [W/mK]**	**Specific Heat [J/(kg K)]**
Lamination (radial)	45	460
Lamination (axial)	34	502
Shaft (Stainless Steel)	50	460
Copper	387.6	381
Winding Insulation	0.18	1000
Epoxy Resin	0.68	1138

- The oil kinematic viscosity and density are modeled as functions of local temperature, based on equations derived from the ExxonMobil® data sheet.

$$\rho = 864 - 44T, \tag{4.1}$$

$$\nu = -20 + 70T - 10T^2. \tag{4.2}$$

  where ρ represents the fluid density in kg/m^3, ν the kinematic viscosity in *cst*, and T the local oil temperature.

- The copper loss input, as illustrated in Fig. 4.4, is treated as a function of the local temperature, using the relationship:

$$P_{\mathrm{cu},T} = P_{\mathrm{cu},T_0} \left[1 + \alpha \left(T - T_0\right)\right] \tag{4.3}$$

  where $P_{\mathrm{cu},T}$ denotes the corrected copper loss, updated according to each temperature T derived from each steady-state simulation. The P_{cu,T_0} is the copper loss measured at the reference temperature T_0, and α is the thermal coefficient for copper.

- To simulate rotor rotation, the *Frozen Rotor* approach is applied by selecting the rotor winding and lamination surfaces in direct contact with air. This technique enables Coriolis and centripetal accelerations to be resolved when *Frame Motion* is activated on these surfaces, thus eliminating the need for costly transient simulations and allowing rotor rotation to be analyzed in steady-state.

- While rotating the rotor would enhance cooling on the end windings as it would expose some of them to oil, the impact of oil on the end windings is excluded in the steady-state simulations.

The pressure-velocity *coupled* solver in ANSYS Fluent is applied to enhance accuracy, particularly in rotating systems where pressure and velocity calculations are closely related. Additionally, the $k-\omega$ turbulence model is utilized to more accurately capture turbulent effects. In Fig. 4.5, simulation outcomes at 8A and 9.2 L/min show temperature contours along the axial and radial directions. Under standstill conditions, the highest temperature is observed in the outermost end winding, where the stationary surrounding air restricts

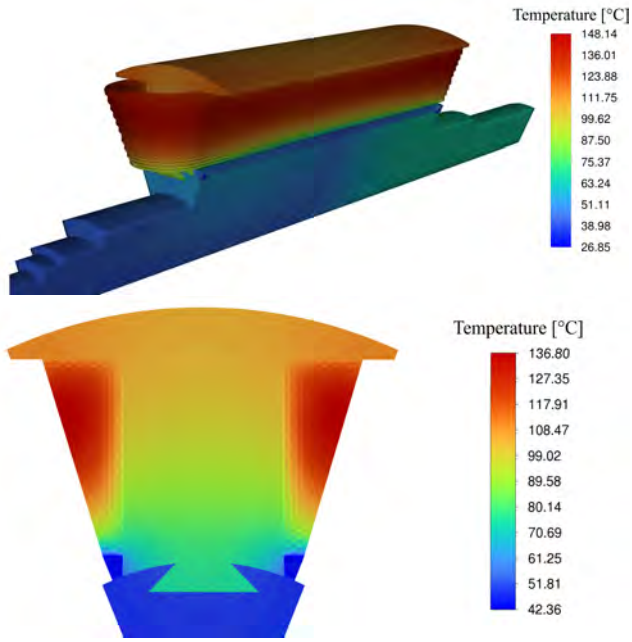

Figure 4.5: Temperature contours from the steady-state CHT model simulating one-eighth of the rotor in standstill condition with 8 A field current and 9.2 L/min oil flow rate.

heat dissipation. The bottom section of the field winding, which directly contacts the oil channels, undergoes significant cooling, cutting the temperature by half, from about 148°C to approximately 75°C. The oil channels also cause a non-uniform temperature distribution across the rotor lamination radially, resulting in a temperature gradient of around 30°C. Additionally, a noticeable temperature difference occurs due to the air gap within the dovetail joint linking the rotor lamination and shaft, where the temperature mainly reflects the oil influence.

In Fig. 4.6, the total dissipated power in the oil cooling system is estimated in ANSYS Fluent based on the average heat flux across the surfaces of the oil ducts. The cooling capacity is then compared with the total copper losses of the rotor and plotted as a function of the field winding current. It is clear that the oil can dissipate a peak power from the rotor just below 2.5

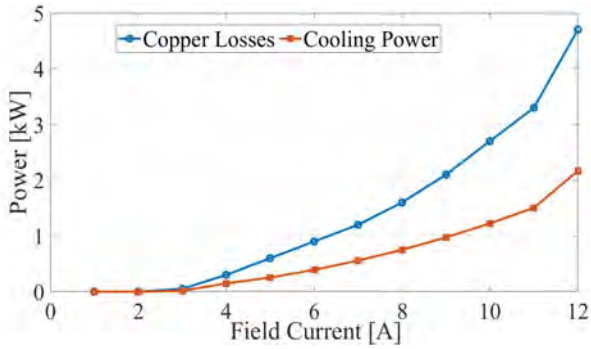

Figure 4.6: Copper losses and power dissipated by the cooling system for different values of the rotor field current.

kW, accounting for approximately half of the total rotor copper losses. This difference decreases as the rotor current is reduced.

Simulations and Experimental Results

In the laboratory, the prototyped rotor is tested under varying copper losses and flow rates, replicating the worst-case operational scenario. This scenario involves the rotor in a stationary state, with no ventilation or oil spread to assist in cooling the end windings. The pressure drop and temperature at various points on the rotor are measured and then compared with the simulation outcomes. The primary emphasis is on assessing the winding temperatures at three typical operating points relevant to an electric long-haul truck, as illustrated in Fig.4.1.

The EESM rotor consists of two main components: a stainless steel hollow shaft with cooling channels drilled in both axial and radial directions, as detailed in Fig. 4.3, and poles made of laminated electrical steel. The assembly of the rotor prototype involves three essential processes: field winding wrapping around the poles, poles mounting onto the shaft, and epoxy resin potting. Conductors are wound individually around each laminated rotor pole and connected in series. This approach allows for a high fill factor by utilizing closed slots before attaching the poles to the shaft, as depicted in Fig. 4.7.

After the rotor assembly is completed, a fiberglass bandage is wrapped around the rotor end winding to prevent conductor displacement at high

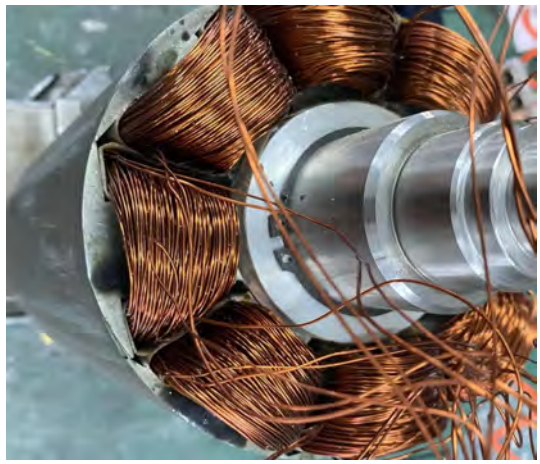

Figure 4.7: Image of the prototyped rotor during the winding of the field conductors around the poles.

speeds. Fiberglass is selected for its mechanical strength, effectively securing the rotor conductors during operation. The entire structure is then filled

Figure 4.8: Image of the prototyped rotor post-application of epoxy resin, fiberglass bandage, and extra material for balancing.

with epoxy resin to enhance compactness and define the oil cooling channels with greater accuracy, as shown in Fig. 4.8. The laboratory setup, depicted schematically in Fig. 4.9 and shown in Fig. 4.10, is used to evaluate the proposed cooling system effectiveness. The cooling circuit includes two gear pumps, an oil reservoir, a heat exchanger, an oil filter, and power supplies for the pumps and field excitation. The first pump delivers oil from the reservoir to the rotor shaft, while the second pump draws the oil through the oil filter and heat exchanger. The rotor is positioned inside a plastic enclosure and elevated on wooden supports to thermally insulate the lamination. During thermal tests, the oil flow rate is set to 9.2 L/min, and the water flow rate for cooling the oil in the heat exchanger is maintained at 7.5 L/min. The water temperature is held at 45°C during all the tests duration.

Various sensors are integrated into the setup: a pressure transducer to measure the oil pressure drop across the rotor cooling system, two Swissflow SF-800 flow rate sensors to ensure accurate oil and water flow rates, and temperature sensors to monitor the oil and water temperatures at the heat exchanger inlet and outlet, as well as at the rotor inlet, to maintain desired fluid temperatures.

Five thermocouples are used to measure the temperatures of the shaft, rotor lamination, and field winding at three distinct locations, as shown in Fig. 4.11. Sensor 1 is placed on the end winding, identified as the rotor hot spot based on Fig. 4.5. Sensors 2 and 3 are located on the coil side near the oil path, at

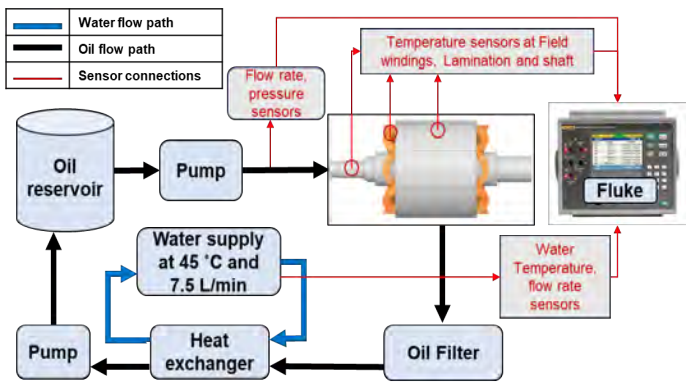

Figure 4.9: Schematic of the oil cooling setup used for experimental measurements.

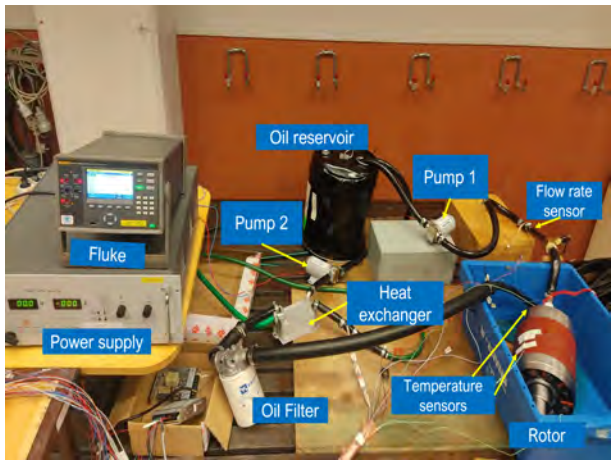

Figure 4.10: Picture of the oil cooling setup used for experimental measurements.

an axial depth of 20 mm from the rotor outer surface. Sensor 4 is positioned on the non-drive end of the shaft, while Sensor 5 is on the rotor outer surface.

The field excitation system is current-controlled to maintain a constant current value, simulating the machine actual operation under different copper loss conditions.

Several experimental tests are performed to validate the CHT model and evaluate the cooling method effectiveness. The fluid dynamics model is first verified by measuring the pressure across the rotor cooling system. This process involves recording the pressure at the rotor inlet while adjusting the oil flow rates. Since the pressure at the rotor outlet is zero, the inlet pressure represents the total pressure drop. In Fig. 4.12, the static pressure drop is shown as a function of the inlet oil flow rate. The results indicate a minimum pressure drop of 2.5 kPa at 1 L/min and a maximum of approximately 35 kPa at 15 L/min, with the oil temperature consistently maintained at 45°C. Notably, the experimental data aligns closely with the CFD simulation results, showing an error margin of less than 5%.

Thermal tests are then conducted by setting the rotor current at different values to simulate copper losses at various operating points of the machine.

In Fig. 4.13, the recorded temperatures for the end winding, which is expected to experience the highest temperatures, and the rotor lamination are

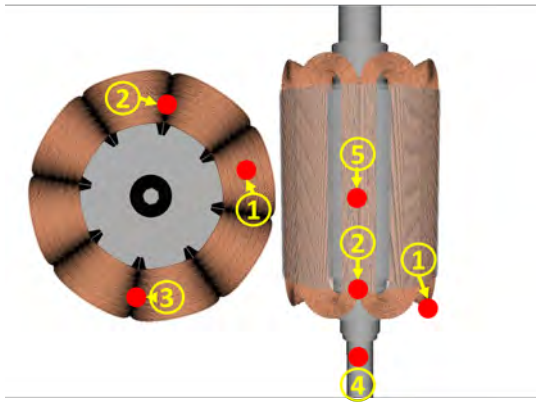

Figure 4.11: Location of temperature sensors: Sensor 1 is located at end winding (hotspot); Sensor 2 and Sensor 3 are located on the coil sides with an axial depth of 20 mm from the rotor outer face and respectively at rotor top side and bottom side; Sensor 4 is on the shaft, Sensor 5 is on the outer surface of the rotor lamination.

shown. These measurements were taken at three different rotor current levels: 3 A, 5 A, and 8 A, over a 60-minute testing period. The temperature profile reveals a characteristic first-order thermal response, stabilizing at a steady-state value after roughly 40 minutes.

Fig. 4.14 displays the steady-state temperatures of the field winding, rotor lamination, and shaft after 60 minutes of testing across a range of rotor current values, from 3 A to 8 A. This corresponds to rotor current densities ranging from 3.18 A/mm^2 to 11.4 A/mm^2. These temperature values are then compared to those from the CHT steady-state simulations in ANSYS Fluent.

As expected, Sensor 1 registers the highest temperature at the rotor end winding, since that part of the rotor circuit is completly surrounded by air that represents a barrier for the heat trasnfer. Conversely, Sensor 3 records the lowest temperature among the rotor winding, due to its proximity to the oil channel and its placement in the lower section of the rotor, where it also benefits from gravity-assisted oil flow from the upper channels.

Sensor 2, unaffected by these factors, records a comparatively higher temperature. Both the rotor winding and rotor lamination display a power-law

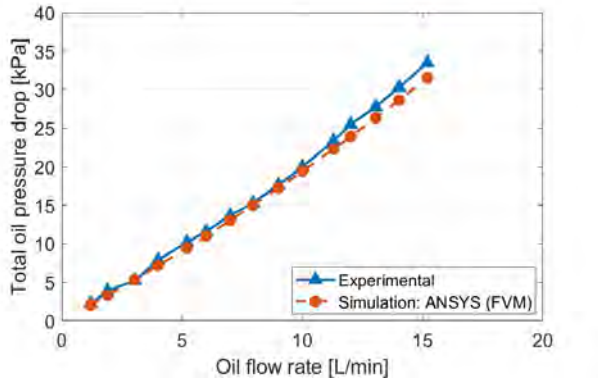

Figure 4.12: Total pressure drop along the rotor cooling system as function of the oil flow rate, while the rotor is not excited and the oil temperature is kept at 45°C . Both experimental measurements (blue) and simulations in ANSYS Fluent using FVM (red) are shown.

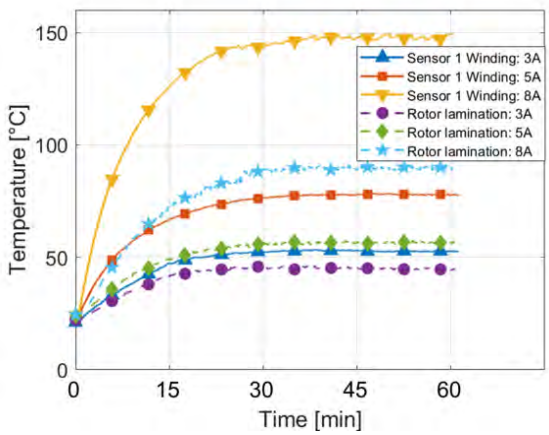

Figure 4.13: Temperature of the end winding (Sensor 1) and lamination after 60 minutes (steady state). Direct oil cooling is activated and field current is set at three different values of 3 A, 5A and 8 A.

relationship as the field current increases, leading to higher temperatures. In contrast, the hollow shaft temperature remains mostly stable, primarily influ-

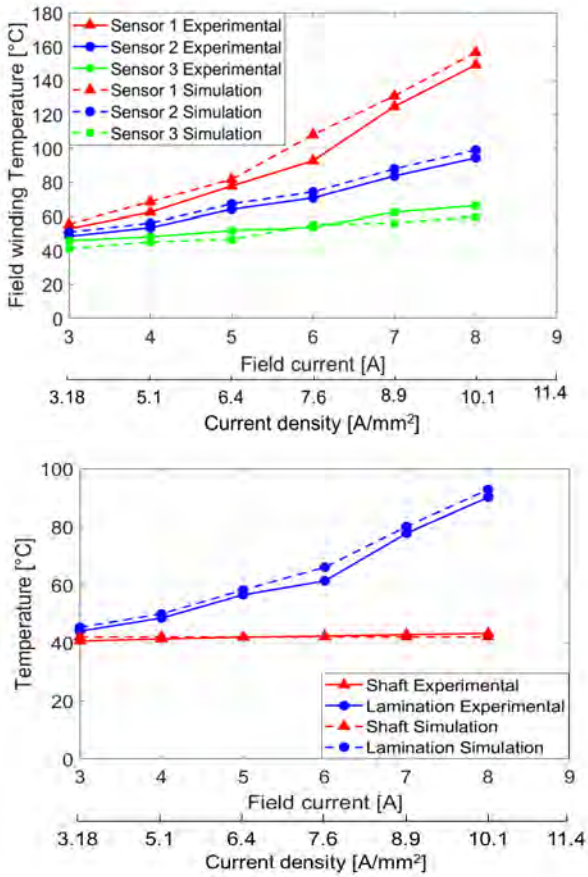

Figure 4.14: Comparison between experimental and simulation results of the steady-state temperatures with direct-oil cooling.

enced by the coolant temperature, which is maintained around 45 degrees.

A maximum deviation of 5% is observed between the experimental and simulated results. This discrepancy is primarily attributed to random factors such as variations in sensor placement, imperfections in the epoxy application, and inconsistencies in glue usage during the manufacturing and measurement processes.

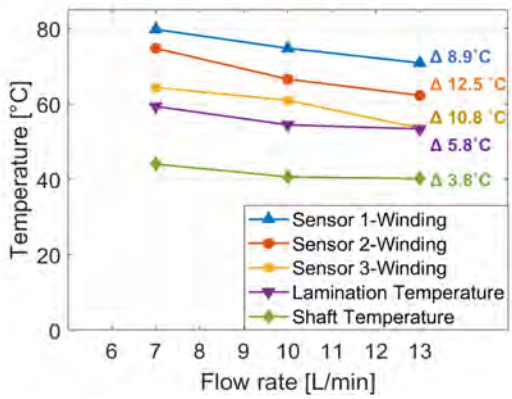

Figure 4.15: Temperature of the field winding, lamination and shaft varying the oil flow rate at constant field current of 5A. The Δ gives the temperature difference between the lowest and highest flow rate values.

An additional test is conducted to examine the influence of flow rates on the cooling system effectiveness. This test involves adjusting the inlet oil flow rate from 7 L/min to 13 L/min while keeping a constant field winding current of 5A. The temperature results from this test are presented in Fig. 4.15, along with the maximum temperature variations observed. Sensors 2 and 3, positioned near the cooling channels, are most affected by changes in flow rate, showing maximum temperature variations of 12.5°C and 10.8°C, respectively. Sensor 1 is also notably impacted, with a maximum temperature change of 10.8°C. In contrast, the flow rate has a minimal effect on the temperatures of the lamination and shaft, with maximum variations of 5.8°C and 3.8°C, respectively.

Heavy Duty Truck Requirements

Tests are performed at various rotor currents and test durations to verify compliance with heavy-duty truck (HDT) requirements, specifically at the three typical operating points outlined in Fig. 4.1: (1) *Startup*; (2) *Climbing*; (3) *Cruising*.

Experimental results along the torque-speed map for different scenarios are displayed in Fig. 4.16. In the figure, the colors indicate the maximum oper-

ational time at a specific operation before reaching the critical temperature of 180°C, which is determined by the insulation class of the rotor conductors. Each color corresponds to an operating region with a specific rotor current required to achieve the associated torque. For further context, in Fig. 4.16(a), tests are conducted without direct oil cooling, with the rotor held in a stationary state.

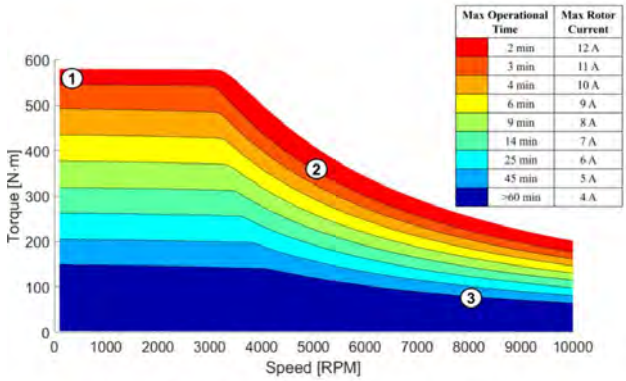

(a) **Experiments with no rotor cooling and no ventilation.**

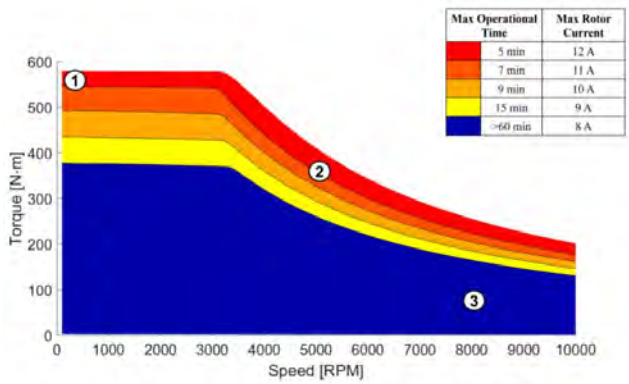

(b) **Experiments with rotor cooling and no ventilation.**

Figure 4.16: Maximum operational time before reaching the insulation class limit of 180°C along the torque-speed map from experimental measurements with: (a) no oil cooling activated; (b) oil cooling activated. In both cases, the rotor is stationary so no ventilation effect is achieved.

This scenario represents the worst-case condition, as the field current is kept constant with no oil cooling and no ventilation effects are achieved due to the stationary state. Under these conditions, only the *Crusing* (3) requirement is partially satisfied, allowing the truck to partially operate continuously at that point. In Fig. 4.16(b), tests are conducted but this time the direct oil cooling system is activated and again with the rotor at a standstill. Here, the blue region, representing an area where the truck can operate for an extended period, expands due to the effects of the direct oil cooling. Consequently, the continuous rotor current capacity doubles from 4A to 8A, effectively doubling the corresponding torque as well. This expansion enables compliance with the requirements for both *Startup* and *Cruising*. However, the *Climbing* requirement is not fully met: at point (3), the truck can run indefinitely with oil cooling, and it can operate for 5 minutes at point (1). In contrast, it cannot sustain operation for 20 minutes at point (3), as the field winding insulation would start to degrade after 7 minutes due to the high temperature.

In Fig. 4.17, the CHT model is used to conduct comprehensive simulations across the machine torque-speed map. In this scenario, both oil cooling and ventilation effects from rotor rotation are activated, with the color map representing the peak steady-state temperature of the field winding, the com-

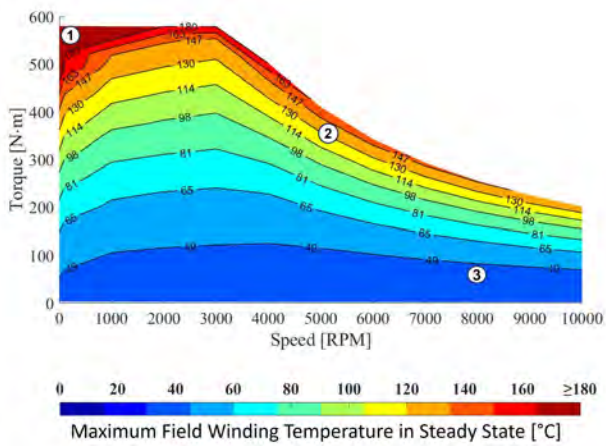

Figure 4.17: Maximum steady-state temperature of the field winding from CHT simulations.

ponent experiencing the highest temperatures. The red color marks regions where extended operation is infeasible (in steady state) due to rotor conductor temperatures exceeding the insulation class maximum threshold. Notably, the area where the truck can operate continuously expands considerably compared to Fig. 4.16(b), showing an increased rotor current capacity in the continuous region from 8A to 10A, along with a temperature reduction correlating with rising speeds. This improvement ensures that requirements are met, even for the *Climbing* condition. Therefore, the proposed cooling solution successfully meets all HDT requirements.

Rotor cooling conclusions.

This chapter introduces a novel design for an EESM rotor with direct oil cooling for heavy-duty trucks, validated through both simulations and experiments. Experimental tests confirm that the rotor can maintain stationary operation up to a current of 8 A, equivalent to a current density of 10.1 A/mm^2. This demonstrates that the proposed direct oil cooling system effectively doubles the allowable current density for continuous operation, from 5.05 A/mm^2 to 10.1 A/mm^2. Thanks to the enhanced cooling from oil circulation, the duration for *Startup* extends from 2 to over 5 minutes, and for *Climbing* from 4 to 7 minutes.

Although the tests were conducted with the rotor in a stationary state, rotor rotation was simulated using a CHT model, incorporating losses from FEM electromagnetic calculations. According to the CHT model, when the rotor is rotating, the continuous operating range expands, and the 20-minute requirement for *Climbing* is comfortably met. The model is validated against experimental data, with temperature predictions accurate within a 5% margin. This discrepancy primarily arises from factors such as the presence of glue and epoxy and from uncertainties in sensor positioning during manufacturing.

4.4 Oil Splashing

One of the most immediate solutions to direct cool an electric machine using oil is to partially fill the housing with the coolant, leveraging the thermal benefits from oil splashing. Even though the rotor mechanical losses are well-documented and pose a significant challenge, especially at elevated speeds

and higher oil levels, the prediction and quantification of these losses have not been thoroughly investigated, leaving a gap in current research. The Moving Particle Simulation (MPS) approach, implemented in Particleworks, is employed to estimate the mechanical losses induced by oil viscosity, with convective heat transfer coefficients (HTC) calculated for the 200 kW EESM Prototype across various speeds and oil levels.

MPS Method and Governing Equations

The Moving Particle Simulation (MPS), formerly the Moving Particle Semi-Implicit method, is a numerical method which deals with incompressible flow by discretizing continuum mechanics. The discretization of governing equations is handled with particle interaction models; therefore, mesh generation is not required and geometries are directly imported to the model for the creation of *Distance Funcions*. The MPS method is based on the Continuity Equation and the Navier-Stokes equations, defined respectively as:

$$\frac{\partial \rho}{\partial t} = 0 \tag{4.4}$$

$$\frac{\partial \vec{\mathrm{u}}}{\partial t} = -\frac{\nabla P}{\rho} + \nu \nabla^2 \vec{\mathrm{u}} + \vec{\mathrm{g}} \tag{4.5}$$

where $\vec{\mathrm{u}}, P, \rho, \nu$, and $\vec{\mathrm{g}}$ represent velocity, pressure, density, kinematic viscosity, and gravitational acceleration, respectively.

The Heat Transfer equation is derived from the energy conservation principle:

$$\frac{\partial e}{\partial t} = -\nabla(-\lambda_T \nabla T) \tag{4.6}$$

Here, e denotes the internal energy density, λ_T the thermal conductivity, T the absolute temperature, and $-\lambda_T \nabla T$ the heat flux.

Figure 4.18 presents a flowchart outlining the algorithmic steps of the Moving Particles Simulation method. The process begins by defining the initial conditions for particle positions, velocities, and physical properties. External forces and viscous effects are then calculated to update particle movement. The Poisson equation is solved to compute the pressure field, ensuring incompressibility, followed by corrections to particle velocities and positions based

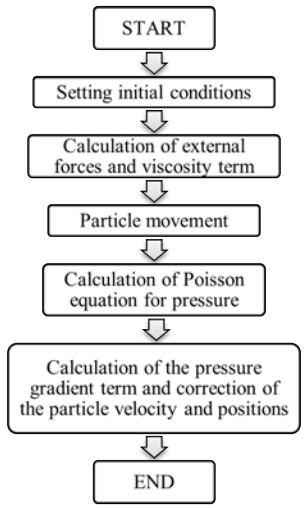

Figure 4.18: Algorithmic steps of the Moving Particles Simulation (MPS) method.

on the pressure gradient. These steps are iteratively repeated until the simulation reaches its conclusion. This method is widely used for accurately modeling complex fluid-particle interactions. The various components of the flowchart are explained in detail in the following subsections.

Effective Radius and Kernel (Weight) Function

Within the MPS method, particle interaction is defined by a distance known as the effective radius.

In Fig. 4.19 the red circle represents the interaction range for the central red particle. The orange and yellow particles lie within this interaction region and are thus considered neighboring particles. Conversely, the black particles are outside this range and do not influence the red particle due to their distance, which exceeds the effective radius. Therefore, the red particle, acting as a reference, only retains information about its neighboring particles. In this way, the effective radius is like a sphere of influence calculated for each particle in a 3D simulation.

The neighboring particles exert varying degrees of influence on the reference particle, decreasing exponentially as the distance increases. This behavior is

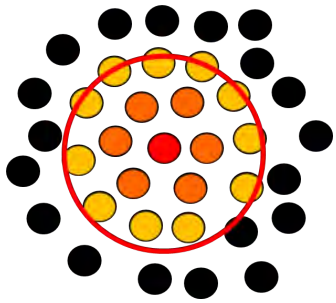

Figure 4.19: Illustration of the effective radius.

represented by the Kernel function. The interaction between the particles is weighted in accordance with the distance between two particles. The equation below is used for the weight function:

$$\omega(|\overrightarrow{r_{ij}}|)=\begin{cases}\frac{r_e}{|\overrightarrow{r_{ij}}|}-1 & 0\leq|r_{ij}|<r_e\\ 0 & |r_ij|\geq r_e\end{cases} \tag{4.7}$$

The subscripts i and j indicate particle indices. r_e denotes the effective radius; additionally, $\overrightarrow{r_{ij}}=\overrightarrow{r_i}-\overrightarrow{r_j}$, where $\overrightarrow{r_i}$ is the position vector of particle i.

Particle Number Density

The particle number density is a distinctive, dimensionless parameter within the MPS method, describing the concentration of particles. It is defined as:

$$n_i=\sum_{j\neq i}\omega\left(|\vec{r}_{ij}|\right) \tag{4.8}$$

This density parameter maintains the incompressibility condition and serves as a measure of fluid density. In the initial state, the particle number density, denoted n^0, is fixed at 54.32 for a three-dimensional simulation. Here, particles are initially arranged in an orthogonal grid with spacing matching the particle size.

Laplacian and Gradient Models

Viscosity and pressure terms are evaluated through the Laplacian differential operator, discretized as:

$$\left\langle \nabla^2 \phi \right\rangle_i = \frac{2d}{\lambda n^0} \sum_{j \neq i} \left(\phi_j - \phi_i\right) \omega \left(|\vec{r}_{ij}|\right) \tag{4.9}$$

$$\lambda = \frac{\sum_{j \neq i} |\vec{r}_{ij}|^2 \, \omega \left(|\vec{r}_{ij}|\right)}{\sum_{j \neq i} \omega \left(|\vec{r}_{ij}|\right)} \tag{4.10}$$

where ϕ is the generic function and d represents the spatial dimensionality; for instance, d=3 in a 3D simulation. Through the Laplacian model, the properties of particle i contribute to neighboring particles such as j. This conservation ensures the amount lost by particle i is transferred to particle j.

The gradient model is the second differential operator, primarily used for velocity correction. Like the Laplacian model, the gradient model utilizes a weight function:

$$\langle \nabla \phi \rangle_i = \frac{d}{n^0} \sum_{j \neq i} \frac{\left(\phi_j - \phi_i\right) |\vec{r}_{ij}|}{|\vec{r}_{ij}|^2} \omega \left(|\vec{r}_{ij}|\right) \tag{4.11}$$

Viscosity Calculation

The effect of the viscosity is computed through the Laplacian model and integrated over time as:

$$\vec{u}_i^* = \vec{u}_i^k + \frac{2d}{\lambda n^0} \Delta t \sum_{j \neq i} v_{ij} \left(\vec{u}_j^k - \vec{u}_i^k\right) \omega \left(\left|\vec{r}_{ij}^k\right|\right) \tag{4.12}$$

where ν_{ij} is the kinematic viscosity coefficient. The superscript k refers to the time step, and the asterisk (*) denotes a physical quantity at the explicit calculation stage.

Velocity and Pressure Calculation

In the MPS method, all terms in the Navier-Stokes equations, except for pressure, are solved explicitly. The explicit calculation follows:

$$\frac{\vec{u}^* - \vec{u}^k}{\Delta t} = v\nabla^2\vec{u}^k + \vec{g} \tag{4.13}$$

Since velocity and viscosity terms are explicitly solved, the pressure term is handled implicitly to satisfy incompressibility. The Poisson equation for pressure is:

$$\nabla^2 P^{k+1} = -\frac{\rho_{ij}}{\Delta t^2}\frac{n^* - n^0}{n^0} \tag{4.14}$$

After determining the pressure, the pressure gradient is calculated to correct velocity as:

$$\frac{\vec{u}^{k+1} - \vec{u}^*}{\Delta t} = -\frac{\nabla P^{k+1}}{\rho} \tag{4.15}$$

The final step of an iteration in the MPS method involves adjusting particle position and velocity with the pressure gradient.

Torque Calculation

A fluid particle, i, is accelerated by a rotating component of the geometry, generating a resistive force on the rotating component. The right-hand side of the Navier-Stokes equation below includes the pressure gradient force, viscous force, and surface tension:

$$\frac{D\vec{u}_i}{Dt} = -\frac{\nabla P_i}{\rho_i} + v_i\nabla^2\vec{u}_i + \vec{S}_i \tag{4.16}$$

The force on the rotating component is:

$$\vec{F}_i = -m_i\left(-\frac{\nabla P_i}{\rho_i} + v_i\nabla^2\vec{u}_i + \vec{S}_i\right) \tag{4.17}$$

where m_i is the mass of the fluid particle. Torque T is calculated as:

$$T = \sum_i \vec{r}_i \times \vec{F}_i \tag{4.18}$$

where $\vec{r}_i$ is the relative position vector of the contact point between the fluid particle and the rotating component, measured from the component's geometrical center.

Heat Transfer Coefficient Calculation

In the MPS method, the heat transfer coefficient is evaluated through forced convection. The local Nusselt number Nu_x, local Reynolds number Re_x, and Prandtl number Pr are given by:

$$Nu_x = hx/\lambda \tag{4.19}$$

$$Re_x = ux/v \tag{4.20}$$

$$Pr = \rho v c_p/\lambda \tag{4.21}$$

Where h, x, λ, u, v, ρ, c_p, and v represent the heat transfer coefficient, distance from the plate starting point, thermal conductivity, mean velocity, fluid density, specific heat, and kinematic viscosity, respectively. The relationship between the local Nusselt number and Reynolds number for both laminar and turbulent flow regimes is defined by the following expressions:

$$Nu_x = \begin{cases} 0.332\,\mathrm{Pr}^{1/3}\,Re_x^{1/2} & \text{Laminar flow} \\ 0.0296\,\mathrm{Pr}^{1/3}\,Re_x^{4/5} & \text{Turbulent flow} \end{cases} \tag{4.22}$$

Machine Modeling

The primary aim of this study is to examine the mechanical losses generated by the interaction between the rotor and oil flow, as well as the heat transfer resulting from the oil movement. For this purpose, a motor model is imported into Particleworks, where computational fluid dynamics (CFD) simulations are performed at various rotational speeds and oil levels using the Moving Particle Simulation method. The primary outputs of the MPS simulations include the viscosity torque, derived from the forces exerted by the liquid on the rotating components, and the heat transfer coefficients on wetted surfaces, calculated using the Nusselt correlation. Extensive simulations are conducted across different oil levels and motor speeds to determine the steady-state av-

erage values of these outputs. These results are subsequently analyzed and visualized through charts to illustrate the observed trends.

The primary advantage of this method is that it is meshless, eliminating the need for mesh generation. As a result, the entire CAD model of the machine, including all its intricate details, can be directly imported into the software environment. Unlike FEM-generated models, this approach will not impact the computational time.

The motor investigated in this study is the 200 kW EESM Prototype intended for truck applications. The rotor field windings are wound around the 8 salient poles, while the stator windings consist of 4 layers of hairpin. ExxonMobil supplies the oil coolant used in this setup. Machine dimensions and oil properties are summarized in Table 4.2 and Table 4.3, respectively.

Table 4.2: Machine Parameters

Parameter	**Value**	**Unit**
Stator Outer Diameter	258	mm
Stator Inner Diameter	173	mm
Rotor Outer Diameter	171	mm
Machine Length	200	mm
Number of Stator Hairpin Layers	8	-
Number of Rotor Poles	8	-
Machine Maximum Power	200	kW
Machine Maximum Speed	10000	rpm

Table 4.3: Oil Properties

Parameter	**Value**	**Unit**
Density	800	kg/m^3
Thermal Conductivity	0.145	W/mK
Specific Heat	1845	J/kgK
Kinematic Viscosity	1.28×10^{-6}	m^2/s
Surface Tension Coefficient	0.03	N/m

Model Strategy

Due to the significant symmetry between the drive-end and non-drive-end parts of the motor geometry, only half of the motor is imported and considered for the simulations. Consequently, all results are doubled to account for the full motor. The motor in the case study is filled with varying oil levels from the bottom to the top: 0.200 L, 0.300 L, 0.500 L, 0.700 L, and 1.100 L, as illustrated in Fig. 4.20.

To analyze the splashing phenomenon, it is essential to consider the impact of air on oil splashing. When the rotor rotates, air ventilation can influence the distribution of oil, which in turn affects the calculation of viscosity torque and heat transfer coefficients. Intuitively, the influence of air on viscosity torque and HTCs is expected to be most significant at high rotational speeds and low oil levels, where the interaction between air and oil is more pronounced. Therefore, air is simulated for oil levels of 0.200 and 0.300 liters only. At higher oil levels (above 0.300 liters), where oil contacts more of the rotor and field winding surfaces, oil movement is primarily influenced by the rotation of the solid parts, as demonstrated in upcoming subsections.

This model avoids meshing the solid parts, allowing the complex motor geometry, particularly the shape of the hairpin end windings, to be imported directly. To reduce computational time, explicit solvers are activated for both pressure and viscosity calculations. For pressure prediction, the speed of sound is estimated to be approximately five times the rotor's tangential velocity.

Time Step Estimation

A particle size of 1.2 mm is utilized in all simulations to ensure that particles can pass through the spacing between hairpin layers. To prevent divergence, the velocity limiter is enabled during simulations, and an appropriate initial time step is established. The maximum particle velocity is estimated as the rotor's maximum tangential velocity, calculated by multiplying the rotor radius r_r and its angular speed ω_r:

$$\mathrm{U_{max}} = \omega_\mathrm{r}\ \mathrm{r_r} \tag{4.23}$$

Based on the oil properties, three critical time steps are defined for simula-

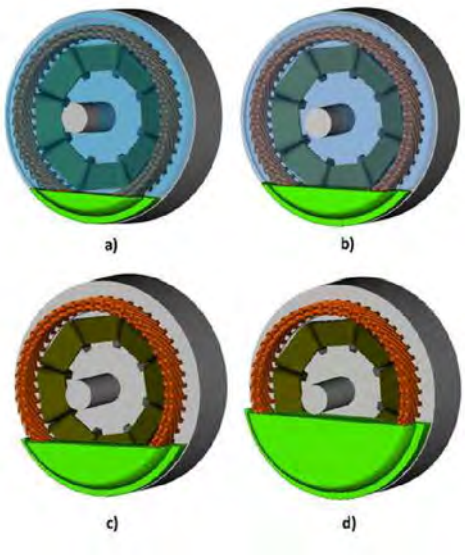

Figure 4.20: Oil levels inside the motor used in simulations: (a) 0.200L of oil + air; (b) 0.300L of oil + air; (c) 0.500L of oil; (d) 1.00L of oil

tion stability:

$$\Delta t = \begin{cases} \frac{l}{U_{\max}}, & \text{Inertial time step} \\ \frac{l^2}{2v}, & \text{Viscous time step} \\ \sqrt{\frac{\rho l^3}{2\pi\sigma}}, & \text{Surface tension time step} \end{cases} \tag{4.24}$$

where ρ is oil density, σ is the surface tension coefficient, ν represents kinematic viscosity, and l denotes particle size. For numerical stability, the global time step must be less than or equal to the smallest time step among those in (4.24).

Air Ventilation

To assess the impact of air ventilation on oil splashing, mechanical losses, and heat dissipation, simulations were conducted at 1000 rpm with 0.500 liters,

comparing three scenarios:

- Oil splashing simulated with the MPS method;
- Multiphase simulation with both oil and air using the MPS method for both the fluids;
- Multiphase simulation combining MPS for oil and Finite Volume Method (FVM) for air.

The simulation results for the three scenarios are presented in Fig. 4.21, showing images of the oil distribution at a specific time frame. It can be observed that the overall oil path remains largely consistent across the three cases, with only minor variations. In the oil-only simulation (a), the splashing is influenced solely by the rotor rotation. Conversely, in cases (b) and (c), where air effects are included using the MPS and FVM methods respectively, subtle differences in oil distribution can be noted. Specifically, small amounts of oil are observed on the housing, shaft, and rotor surfaces, which can be attributed to the interaction with the air.

Fig. 4.22 illustrates the time evolution of viscosity torque applied to the rotor under three simulation scenarios: (1) no air included, (2) air simulated using the Finite Volume Method (FVM), and (3) air simulated using the Moving Particle Simulation (MPS) method. While the viscosity torque exhibits

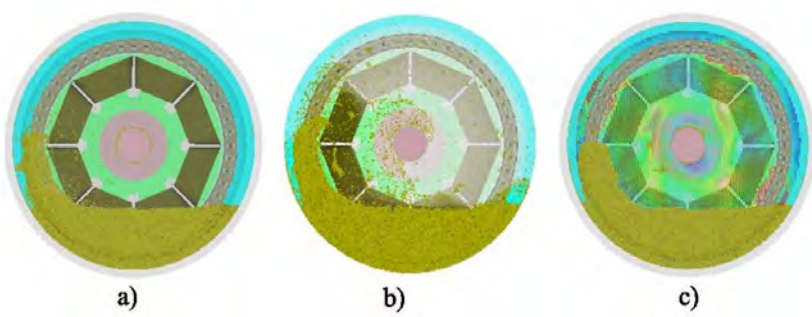

Figure 4.21: Oil splashing at 1000 rpm under three scenarios: (a) oil-only simulation with MPS; (b) oil and air simulated with MPS; (c) oil simulated with MPS and air with FVM.

oscillatory behavior in all cases, the nature of the oscillations differs among the three scenarios.

In the case without air (blue curve), the oscillations are larger in amplitude compared to the air-included scenarios. The FVM air (orange curve) and MPS air (gray curve) scenarios show reduced oscillation amplitudes, indicating that the presence of air affects the dynamic distribution of oil around the rotor. Despite these differences in oscillation patterns, the average viscosity torque values converge to the same level for all three scenarios once the system reaches steady-state conditions.

This result demonstrates that for high oil levels inside the machine air interaction impacts the transient oscillatory behavior of the system but it does not alter the steady-state average viscosity torque. This finding underscores the importance of air modeling for transient effects but also suggests that its influence on long-term torque averages may be negligible for high oil levels. As a result, air is only considered in simulations with very low oil levels, where the rotor lamination and field winding partially interact with the oil, and ventilation significantly affects oil spread.

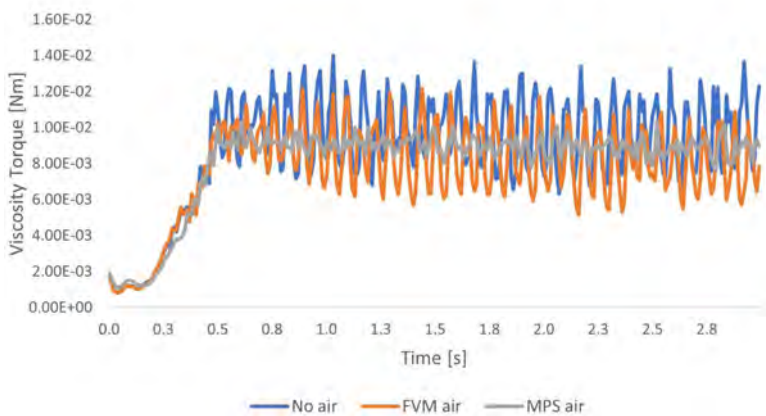

Figure 4.22: Viscosity torque applied to the rotor across three scenarios: with no air simulated; air simulated using FVM; air simulated with the MPS method.

Simulation Results

Extensive simulations were conducted for various oil levels and machine speeds to calculate the HTC and viscosity torque using MPS simulations. An example of the HTC evolution is shown in Fig. 4.23, which depicts the heat transfer coefficient calculated on the surface of the rotor field winding as a function of time. At the beginning of the simulation, when the rotor is stationary, the HTC is initially zero. This happens because there is no relative motion between the rotor and the oil, resulting in no significant heat transfer through convection. As the rotor starts accelerating, the interaction between the oil and the rotor surface intensifies, causing the oil to splash. This splashing effect increases the convective heat transfer, leading to a rapid rise in the HTC.

As the rotor reaches its operating speed, the oil flow stabilizes, and the splashing becomes more uniform. This results in the HTC gradually settling into a steady-state condition, characterized by minor oscillations around a constant average value. This steady-state HTC is critical for evaluating the heat transfer efficiency under specific operating conditions, as it reflects the thermal performance of the motor during continuous operation. The calculation shown in Fig. 4.23 is then repeated for a wide range of machine speed and oil levels as illustraed by the charts in Fig. 4.24. The charts illustrate the variation of surface heat transfer coefficient across various motor components

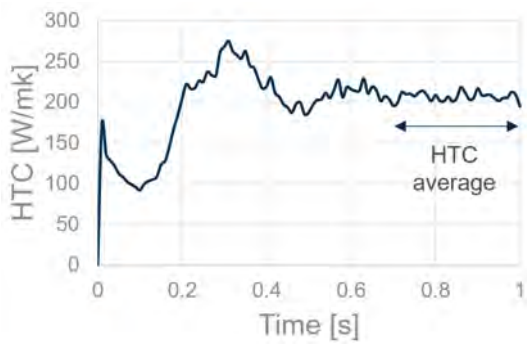

Figure 4.23: Evolution of HTC on the rotor field winding surface at 5000 rpm and 0.500 L oil, showing initial zero HTC at standstill, rapid increase during acceleration due to oil splashing, and stabilization at steady-state conditions.

as a function of rotational speed, evaluated for different oil levels (0.2 L, 0.3 L, 0.5 L, 0.7 L, and 1.0 L). Across all components (stator, shaft, housing, field winding, stator winding, and rotor) the HTC consistently increases with both rotational speed and oil level. For the shaft, field winding, rotor, and stator lamination, a pseudolinear trend in HTC can be seen, with slight saturation observed in some cases. This indicates that increased oil levels, especially 0.7 L and 1.0 L, and high rotor speed contribute to higher heat dissipation. An exception is noted for the stator winding and housing, where the HTC values are similar in the low and high oil volumes. This is explained by the accumulation of coolant in the peripheral area of the machine as a result of centrifugal forces from rotor rotation, regardless of the oil level.

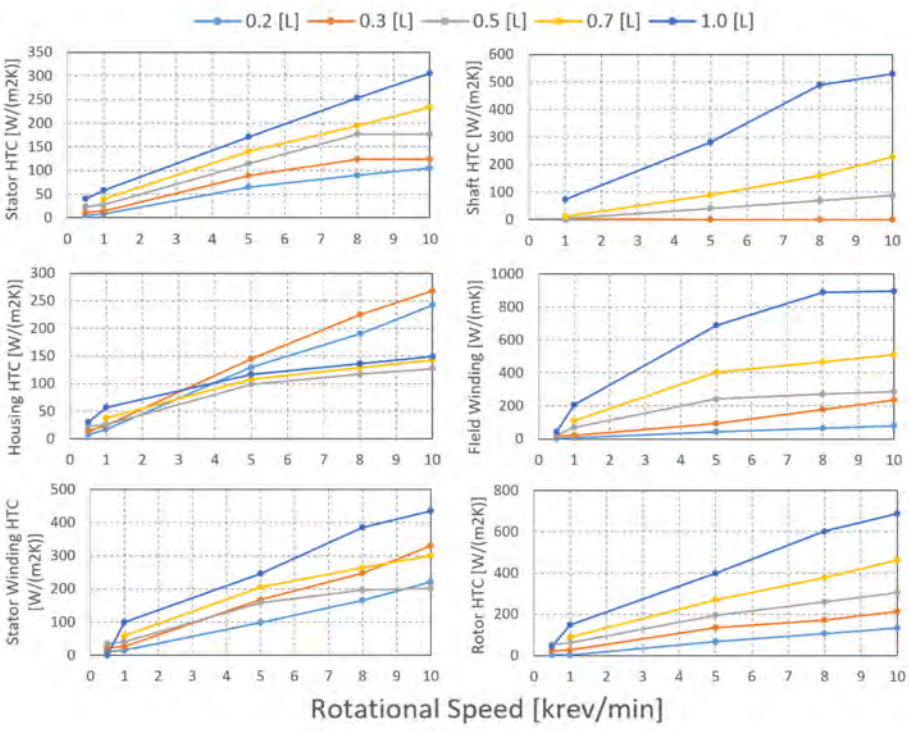

Figure 4.24: Convective heat transfer coefficients for various motor components at different oil level inside the machine.

Qualitative results from the simulations are presented in Fig. 4.25, which illustrates oil splashing behavior across a range of rotor speeds (500 rpm to 10,000 rpm) and oil levels (0.200 L to 1.00 L). The images depict oil distribution at 1,000 rpm, 5,000 rpm, and 10,000 rpm (from left to right) for increasing oil levels (top to bottom).

At the lowest oil level of 0.200 L, oil primarily accumulates at the bottom of the housing, with limited interaction with the rotor and stator components. However, at higher speeds, such as 5,000 rpm and 10,000 rpm, the increased turbulence enables oil to splash and reach the hairpin windings and lamination of the stator. This effect becomes more pronounced as rotor speed increases, where centrifugal forces caused by the rotor's tangential acceleration drive the oil toward the outer diameter of the stator. This phenomenon is observed even at low oil levels, such as 0.200 L, where the oil distribution extends to critical cooling areas, contributing to effective heat dissipation. Higher oil levels further enhance the coverage and cooling performance, demonstrating the interplay between oil volume, rotor speed, and the resulting oil dynamics within the motor.

In Fig. 4.26, the charts illustrate the torque produced by oil viscosity (top) and the resulting mechanical losses (bottom) across a range of machine speeds (500 rpm to 10,000 rpm) and oil volumes (0.200 L to 1.00 L). These results highlight the trade-off associated with using oil as a cooling medium, as the increase in rotor angular velocity leads to significant growth in mechanical losses due to viscosity effects.

At speeds below 1,000 rpm, mechanical losses remain relatively low for all oil levels, as the interaction between the rotor and the oil is minimal, and no substantial viscous load is generated. However, as the speed increases beyond this threshold, the differences between the oil volumes become more apparent. At higher speeds, such as 10,000 rpm, the viscosity torque grows substantially, particularly for higher oil levels. For an oil volume of 1.0 L, the viscosity torque reaches 32% of its maximum value at 10,000 rpm, indicating a significant contribution of oil friction to the system load.

The bottom chart demonstrates how these increases in viscosity torque translate directly into mechanical losses. Mechanical losses exhibit a parabolic dependence on rotor speed, escalating sharply at high rotational velocities. At 10,000 rpm, the mechanical losses for an oil volume of 1.0 L are considerably higher than for lower oil levels, confirming the additional energy demand im-

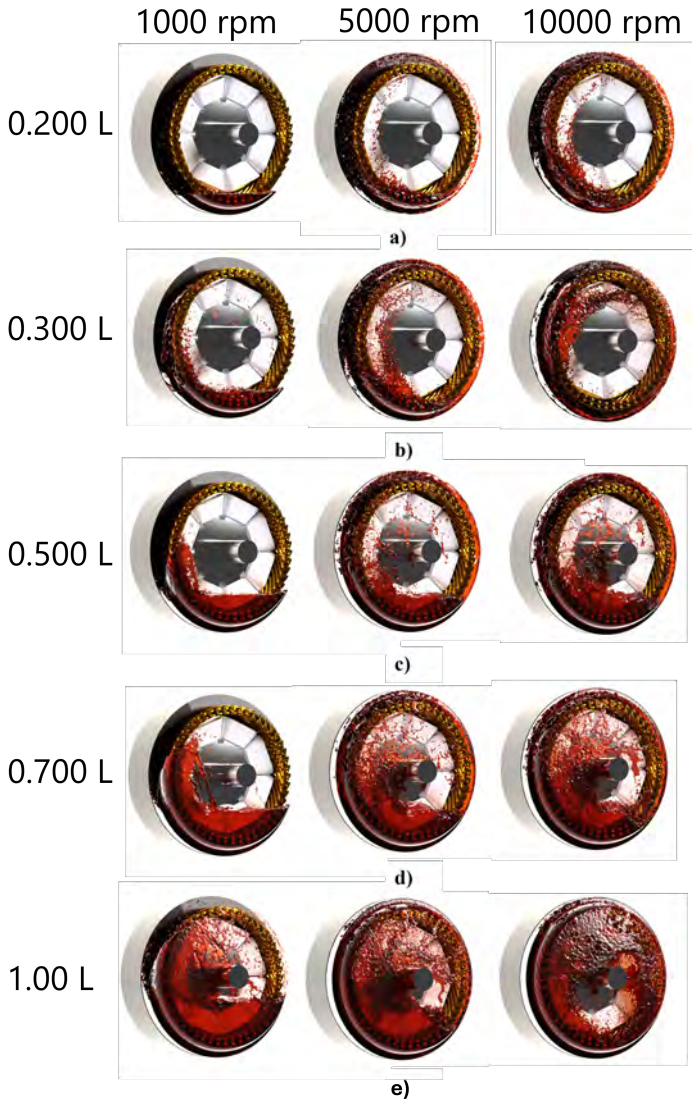

Figure 4.25: Qualitative simulation results of oil splashing within the motor at rotor speeds of 1000 rpm, 5000 rpm, and 10000 rpm (from left to right) across different oil levels: (a) 0.200 L; (b) 0.300 L; (c) 0.500 L; (d) 0.700 L; (e) 1.00 L.

posed by higher coolant volumes. This trend underscores a fundamental drawback of liquid cooling at elevated speeds, where the benefits of heat dissipation must be weighed against the cost of increased mechanical energy losses.

These results emphasize the need to optimize oil levels for balancing cooling performance and minimizing energy penalties, especially in applications where high rotational speeds are common.

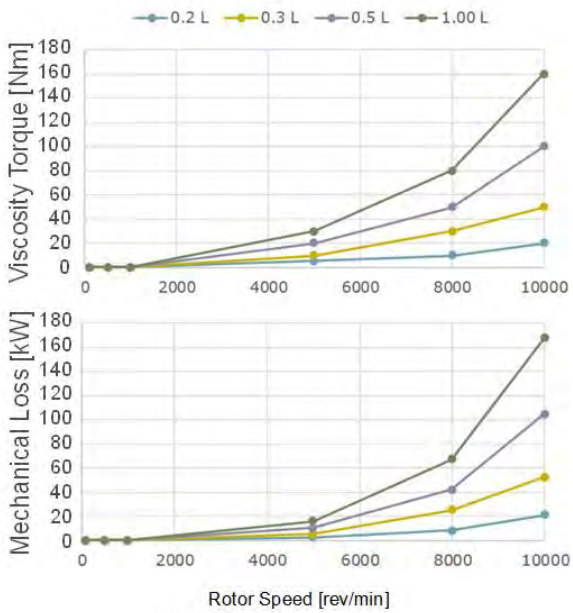

Figure 4.26: Viscosity torque and mechanical losses due to rotor-oil interaction at varying speeds and oil levels.

Oil Splashing Conclusion

This chapter investigated the impact of oil splashing on heat dissipation and mechanical losses in the 200 kW Electrically Excited Synchronous Machine Prototype. The Moving Particle Semi-implicit method proved to be highly computationally efficient, reducing transient fluid-dynamic simulation times from several days to just hours when executed on a commercial GPU. This performance represents a significant improvement compared to traditional FEM

transient simulations

The results demonstrated that oil splashing effectively enhances heat dissipation, with heat transfer coefficients increasing logarithmically with rotor speed until reaching saturation at approximately 9000–10,000 rpm. The oil level was also found to play a substantial role, particularly in cooling non-stationary components such as the rotor laminations, field windings, and shaft.

However, oil splashing introduces considerable mechanical losses, with the viscous torque exhibiting a parabolic relationship with rotor speed. These losses become particularly significant at higher speeds. To address this trade-off, a cooling strategy that actively regulates oil levels based on machine speed would be advantageous, especially for speeds exceeding 1000 rpm.

4.5 Stator Cooling

Effective cooling of the stator poses significant challenges due to the need to simultaneously manage the thermal loads of the lamination, copper conductors, and end windings. The presence of thermal resistances between the stator lamination, housing, and active conductors further reduces the efficiency of cooling. Moreover, achieving proper pressure and maintaining sufficient fluid velocity to ensure adequate cooling of the end windings through impingement adds to the complexity.

This chapter presents the design of a stator oil cooling system for the 200 kW EESM Prototype developed for truck applications. The system integrates an indirect cooling strategy via an oil jacket surrounding the active length of the stator, featuring axial ducts located at the interface between the stator and housing. In addition, the system incorporates direct oil cooling for the end windings by utilizing self-impinging oil from the axial ducts onto the hairpin end windings, eliminating the need for an external oil circuit.

The design was validated through a two-fold simulation approach. A Conjugate Heat Transfer model in ANSYS Fluent was employed to accurately simulate heat transfer within the active part of the stator. Meanwhile, Moving Particle Simulation in Particleworks was used to estimate the heat transfer coefficients at the end windings, ensuring comprehensive evaluation of the cooling performance.

Cooling Strategy

The cooling system comprises an aluminum housing, stator lamination, and a two 3D-printed sleeves at the terminal parts. To enhance heat dissipation from the conductors, the stator cooling system is designed to facilitate oil flow along specific channels, as illustrated in Fig. 4.27.

Firstly, oil is pressurized by a pump and introduced into the housing through an inlet. The oil then flows into the axial channels created at the interface between the stator lamination and the housing. This high-speed oil flow reduces the thermal contact resistance (TCR) between the lamination and the aluminum housing enhancing heat dissipation.

Next, the oil flows to the machine terminals, filling the wet chambers enclosed by the 3D-printed sleeve. The increased oil volume from the axial channels raises the pressure inside these wet chambers. Once the pressure

reaches a sufficient level, the oil is expelled at high velocity through the radial channels, effectively impinging the stator end windings at both machine terminals.

Fig. 4.28 illustrates the axial channels of the oil jacket formed at the interface between the housing and the stator. The figure highlights 36 axial channels, marked in yellow, designated for oil pressurization. In contrast, the remaining channels function submerged in non-pressurized oil, which collects at the bottom of the housing as a result of oil impingement from the end-winding. The bottom axial channels, therefore, are not connected to any wet chambers. Their primary purpose is to establish an oil pathway between the two terminal sections of the machine and to reduce the thermal contact resistance (TCR) between the housing and the lamination at the bottom. This design enables the use of a single oil inlet and facilitates cooling of the bottom end windings by submerging the conductors. The oil level is carefully maintained below the air gap height to prevent additional viscosity losses during rotor rotation.

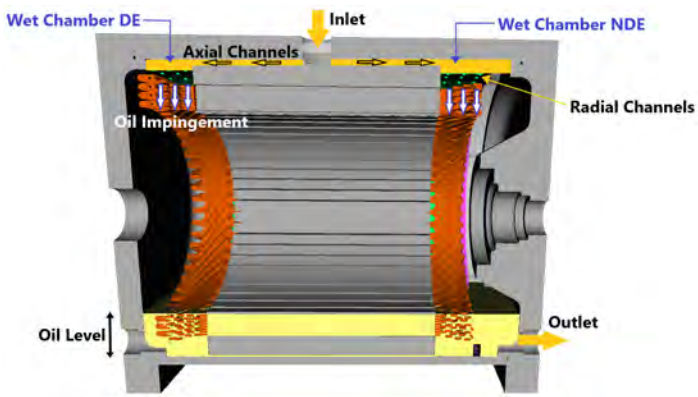

Figure 4.27: Oil is pumped into the housing through an inlet and subsequently flows into the axial channels (oil jacket) at the interface between the stator lamination and the housing. The oil then fills the wet chambers inside the 3D-printed sleeves at both terminals of the machine. Once pressurized, the oil travels through radial channels in the sleeves, providing cooling impingement to the hairpin end windings. Finally, the oil is collected at the bottom, filling the bottom axial channels and submerging the lower part of the end windings.

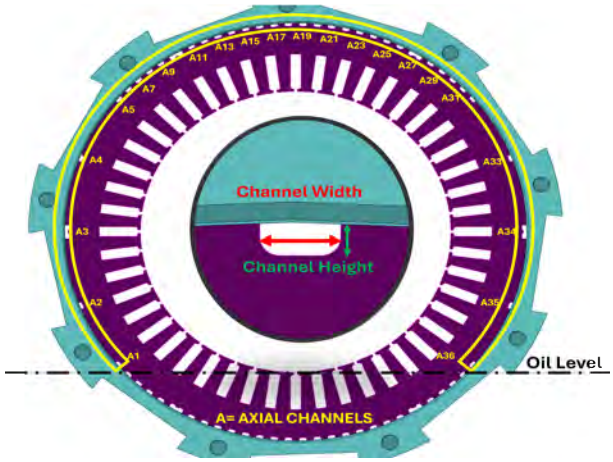

Figure 4.28: Axial channels of the oil jacket. The channels highlighted in yellow are connected to the pressurized wet chambers, while the lower channels are fully immersed in non-pressurized oil collected from the end winding impingement .

Cooling System Design

The oil jacket, positioned between the housing and stator lamination, features a manifold directly connected to an inlet that supplies oil to multiple axial channels. The design of the axial channels has been optimized to minimize the thermal resistance between the aluminum housing and the stator lamination. The thermal resistance is expressed as follows:

$$R_{th} = \frac{1}{h \cdot A} \tag{4.25}$$

where R_{th} is the thermal resistance (K/W), h is the heat transfer coefficient $\left(\mathrm{W}/\left(\mathrm{m}^2 \cdot \mathrm{K}\right)\right.$) and A is the surface area through which heat is being transferred $\left(\mathrm{m}^2\right)$. Thus, the thermal resistance can be reduced by increasing the heat transfer coefficient and the surface area. The surface area A is a function of:

$$A = f(N, w, h) \tag{4.26}$$

where N is the number of axial channels comprising the oil jacket between the stator and housing, and w and h are the width and height of each axial channel, respectively. Section III presents computational fluid dynamics (CFD) simulations performed to analyze the effects of varying the width and height of the axial channels. These variations enable the calculation of the total pressure drop and average fluid velocity, facilitating the generation of a dataset encompassing different width and height combinations for the axial channels. The inverse relationship between velocity maximization and pressure minimization necessitates a multi-objective optimization approach, where trade-offs between conflicting objectives are carefully considered. To address this trade-off, a Pareto Front is utilized to identify a set of optimal designs balancing these competing goals.

The objective functions chosen to delineate the Pareto Front are:

- The pressure drop along the stator cooling system (ΔP).
- The oil velocity at axial channels outlet (v_{out}).

The optimization goals are defined as follows:

$$\text{Minimize: } f_1 = \Delta P, \tag{4.27}$$

where ΔP is the pressure drop, representing energy losses in the cooling system.

$$\text{Maximize: } f_2 = v_{\text{out}}, \tag{4.28}$$

where v_{out} is the oil velocity at the outlet, ensuring effective cooling performance. The optimization can then be expressed as:

$$\text{Minimize: } \mathbf{f}(\mathbf{x}) = \{f_1(\mathbf{x}), -f_2(\mathbf{x})\}, \tag{4.29}$$

where x represents the design variables (channel height and width)

The solution to this problem is a Pareto Front, which highlights the trade-offs between minimizing pressure drop and maximizing outlet velocity, aiding in the selection of optimal designs.

Considering the equation (4.25) and the following definition of HTC for forced convection:

$$h = \frac{Nu\lambda}{D} \tag{4.30}$$

where Nu is the Nusselt number, λ the thermal conductivity of the fluid, D

the characteristic length (e.g. channel diameter), and taking into account the definition of Nusselt for a laminar flow:

$$Nu = 0.332\,\mathrm{Pr}^{1/3}\,Re^{1/2} \tag{4.31}$$

where Pr and Re are the Prandt l and Reynolds number respectively, it is evident that optimizing the Reynolds number will result in higher values of the heat transfer coefficient and a lower value of thermal resistance. For the above mentioned reasons, a third objective function equal to the Reynolds number is added to the optimization:

$$\text{Minimize:} \quad -f_3(x) = \text{Reynolds}. \tag{4.32}$$

After defining the objective functions and optimization criteria, the Non-Linear Programming by Quadratic Lagrangian (NLPQL) gradient-based algorithm is implemented to select the best designs. Upon completion of the algorithm, the 3D Pareto front is identified, and a set of potential design points is obtained.

Fluid-Dynamic and Thermal Model

To optimize oil flow through all channels and estimate heat dissipation from the stator hairpins, a CHT model using Finite Volume Method (FVM) is developed, incorporating both CFD and heat transfer analysis. The flowchart illustrating the creation process is shown in Fig. 4.29.

The 3D CAD geometry of the stator, housing, and winding is divided into two main sections: the end regions, which include the end windings, and the active region, which includes the conductor active length and the stator lamination. This division is necessary because in the active region of the machine, where fluid domains are well-defined, FVM in ANSYS Fluent can be effectively applied to compute the oil flow throughout the cooling system.

Conversely, transient CFD simulations are required to model oil impingement on the end windings in the terminal regions, as the fluid volume in these areas cannot be predefined. To reduce the computational time for these simulations, a meshless MPS method is preferred to the FVM. Whereas the CHT model can directly utilize the HTCs calculated by the CFD solver, the HTCs for the end windings self-impingement are computed separately using the MPS model. Once these HTCs are averaged over the selected surfaces and reach a steady-state condition, they can be imported into the CHT model for

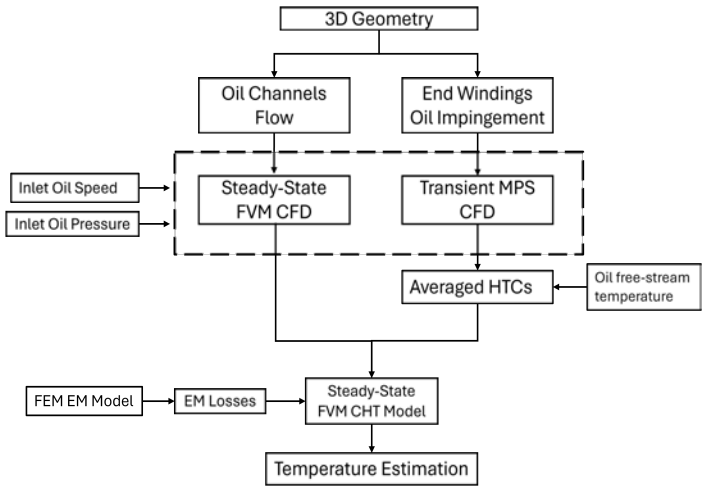

Figure 4.29: Flowchart of the Conjugate Heat Transfer model implementation of the stator cooling system.

temperature computation.

For both the FVM and MPS models, one of the key inputs is represented by the oil properties, including kinematic viscosity, dynamic viscosity, and density. The temperature-dependent variation of these oil properties is consid-

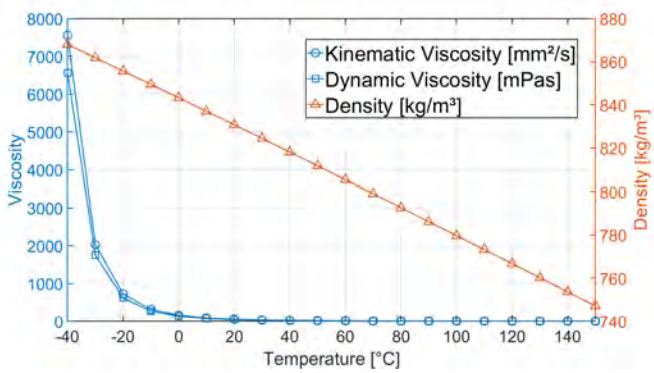

Figure 4.30: Properties of the oil as a function of the temperature.

ered, and the corresponding values as a function of temperature are presented in Fig. 4.30.

Oil Channels Flow

To optimize the cooling system channels and calculate the oil flow, a Computational Fluid Dynamics model was developed in ANSYS Fluent using the Finite Volume Method. The model employs polyhedral mesh elements, which effectively reduce the total number of cells while maintaining high mesh quality, with a maximum skewness of 0.7 and a minimum orthogonal quality of approximately 0.2. The solution method used for the simulations is a second order Pressure-Velocity Coupled method whereas the viscous model is the SST k-ω. The SST k-ω turbulence model [58] is a widely used two-equation eddy-viscosity model. It combines k-ω for accurate near-wall modeling without extra damping functions and transitions to k-ϵ in the free stream, reducing sensitivity to inlet turbulence properties. The model performs well in adverse pressure gradients and separating flows but slightly overpredicts turbulence in regions with large normal strain, such as stagnation zones, though less so than standard k-ϵ models.

The model used for the simulations and the results in terms of oil velocity are illustrated in Fig. 4.31 and Fig. 4.32.

Fig. 4.31 depicts the velocity contours of the oil, encompassing the inlet, the manifold at the middle of the active length, the axial channels, and the radial channels. A detailed view of the cross-sectional area at the outlet is provided for selected axial and radial channels. The results reveal significant variations in velocity magnitude across the axial channels, depending on their relative position to the inlet.

The axial channels located closest to the inlet (e.g., A17, A18, A19, and A20) exhibit the highest velocity magnitudes, highlighted by the red color in the contours, with peak velocities reaching approximately 2 m/s at the center of these channels. Moving further from the inlet, the maximum oil velocity decreases progressively, ranging between 1.0 m/s and 0.7 m/s. The axial channels furthest from the inlet experience a substantial velocity drop, with maximum velocities around 0.2 m/s.

In contrast, the radial channels demonstrate a maximum oil velocity that is largely independent of their distance from the inlet. The furthest radial channels (e.g., R1, R2, and R3) exhibit outlet velocities around 1 m/s, which

are comparable in both velocity field contours and peak values to those of the radial channels closest to the inlet. This behavior is also illustrated in the graph in Fig. 4.32, which shows the average outlet velocity of the fluid for all 36 axial channels and all 61 radial channels at the machine drive end. As previously observed, the axial channels exhibit significant variations in speed depending on their distance from the inlet. The channels around index 18, which are closest to the inlet, experience the highest average outlet velocity compared to those located at the far ends.

In contrast, the radial channels display a consistent average outlet velocity regardless of their position. This uniformity ensures an even oil impingement on the end-winding stator conductors, contributing to an effective and balanced cooling across the system.

One of the advantages of the FVM in ANSYS Fluent is that the HTCs are internally calculated by the CFD solver and directly imported into the CHT model when the *Energy* solver is activated.

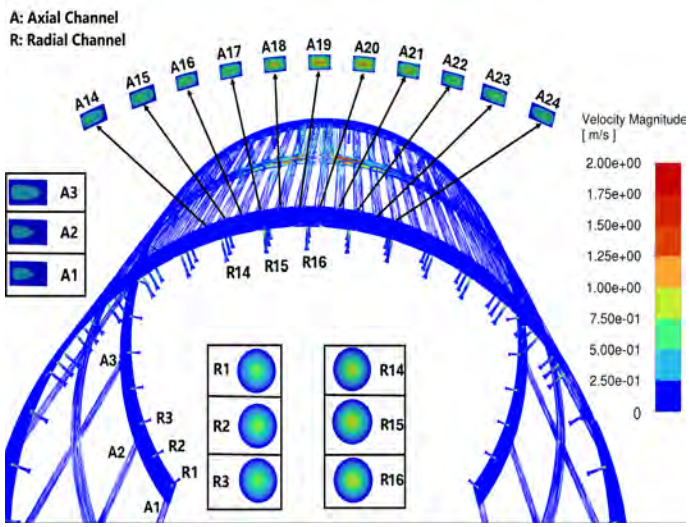

Figure 4.31: Velocity contours from CFD simulations of the fluid flow within the model. Enlarged views display the cross-sectional areas at the outlets of the axial (A) and radial (R) channels.

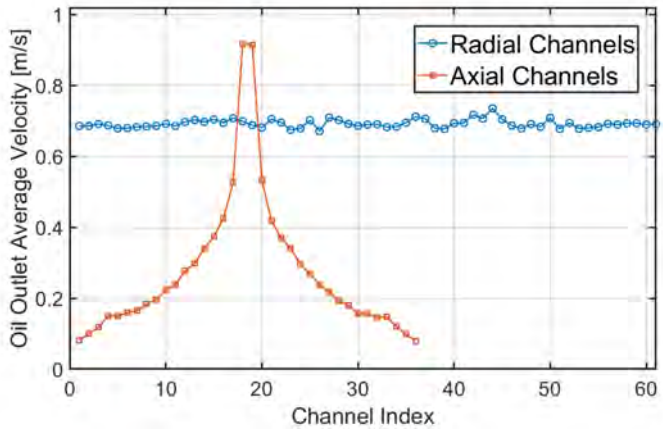

Figure 4.32: Outlet average velocity of the radial and axial channels.

End Windings Impingement

Transient CFD simulations are conducted using the MPS method in Particleworks to model the oil flow impingement from the radial channels onto the end-winding and to extract the surface HTCs. The Moving particle semi-implicit method, presented in [59], [60], is a particle-based numerical approach where the fluid volume is discretized into particles, each carrying physical properties like velocity, pressure, and mass. The particles interact within a defined *Kernel Radius*, representing the influence area for calculations.

Distance Functions are used to model the interaction between particles by defining the spatial relationships and enabling computation of gradients, such as pressure and velocity, without a mesh. These functions ensure continuity and smoothness in particle interactions, simulating fluid behavior accurately. The method solves the Navier-Stokes equations by approximating differential operators, ensuring mass conservation and handling complex free surfaces and interfaces effectively.

The model used for the simulations, along with the results in terms of oil flow and heat transfer coefficients (HTCs), is presented in Fig. 4.33 and Fig. 4.34. In Fig. 4.33, the surface defined by the fluid particles is highlighted in yellow, illustrating how the oil exiting the radial channels impinges on the end winding, collects at the bottom of the housing, and subsequently exits through

the outlet hose. The HTC contours are also displayed, demonstrating a relatively uniform cooling along the entire hairpin conductors. Predominantly, the HTCs fall within a range of 200 to 300 $W/(m^2K)$ with peak values reaching up to 600 $W/(m^2K)$

Fig. 4.34 consists of three subfigures that illustrate the surface average HTCs calculated across different layers of the hairpin winding. Fig. 4.34 provides a cross-sectional view of the analyzed geometry, highlighting the Upper Layers and Bottom Layers with their respective configurations. The layers are color-coded for clarity: red represents layers 1-2, blue represents layers 3-4, black represents layers 5-6, and green represents layers 7-8.

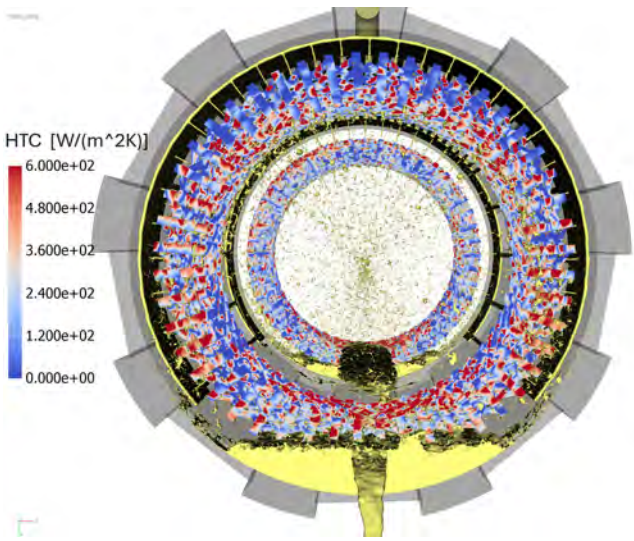

Figure 4.33: Surface heat transfer coefficient contours resulting from oil impingement on the end winding at the machine drive end. The yellow regions indicate oil flow as simulated by the MPS model after 3 seconds.

Fig. 4.34 (b) shows the evolution of the heat transfer coefficient (HTC) over time for the Upper Layers. The results reveal that layer 1-2 exhibits the highest HTC throughout the simulation, as these layers are closest to the radial channel outlets. The HTC progressively decreases for subsequent layers, with layers 5-6 and 7-8 showing the lowest values. The HTC stabilizes after approximately 2 seconds, corresponding to the point when the oil flow

from the radial channels reaches steady-state conditions.

Fig. 4.34 (c) presents the HTC evolution over time for the Bottom Layers. Unlike the upper layers, the bottom layers exhibit a significantly larger variation in HTC between the different layers.

Layer 7-8 achieves the highest HTC, indicating superior cooling performance due to the fact that these layers will benefit from the oil falling from the upper part of the machine. Conversely, layers 1-2 and 3-4 exhibit significantly lower HTC values, as no radial channels are present at the bottom of the machine to enhance cooling performance in these regions.

Conjugate Heat Transfer Model

The final CHT model is implemented in ANSYS Fluent by integrating the CFD FVM model and the three-dimensional mapping of the surface average HTCs computed from the MPS model once steady-state condition is achieved. The solids are meshed including the aluminum housing, the aluminum endplates, the stator core and the stator windings. In order to take into account the additive thermal resistances from the manufacturing process, further thermal resistances are inserted into the model in form of *Shell Conduction*. The model includes the insulation enamel for the stator conductors, with a thermal conductivity of $0.4\,\mathrm{W/(m \cdot K)}$, the slot liner, with a thermal conductivity of $0.18\,\mathrm{W/(m \cdot K)}$, and the interface air pockets between components caused by assembly imperfections. Notably, an effective air gap of 0.0026 mm is considered between the stator core and the housing, specifically between the aluminum and iron components, as derived in [61].

Fig. 4.35 illustrates the steady-state temperature distribution within the motor components from the final Conjugate Heat Transfer model. The results are presented as temperature contours in an axial cross-sectional view (top) and a radial cross-sectional view (bottom). The simulation encompasses key motor regions, including the stator, windings, housing, and end plates. Axial cooling channels are incorporated into the model, while the surface heat transfer coefficients at the end windings are imported from the MPS simulations.

In the axial view (top), the temperature distribution highlights the maximum temperatures occurring in the vicinity of the stator hairpin conductors in both the active part of the machine and the end windings. The end windings are prominently depicted in green and orange tones, indicating peak tempera-

tures in the range of 70–80°C, with localized hotspots approaching 90°C. The effectiveness of direct oil impingement cooling in this region is evident when

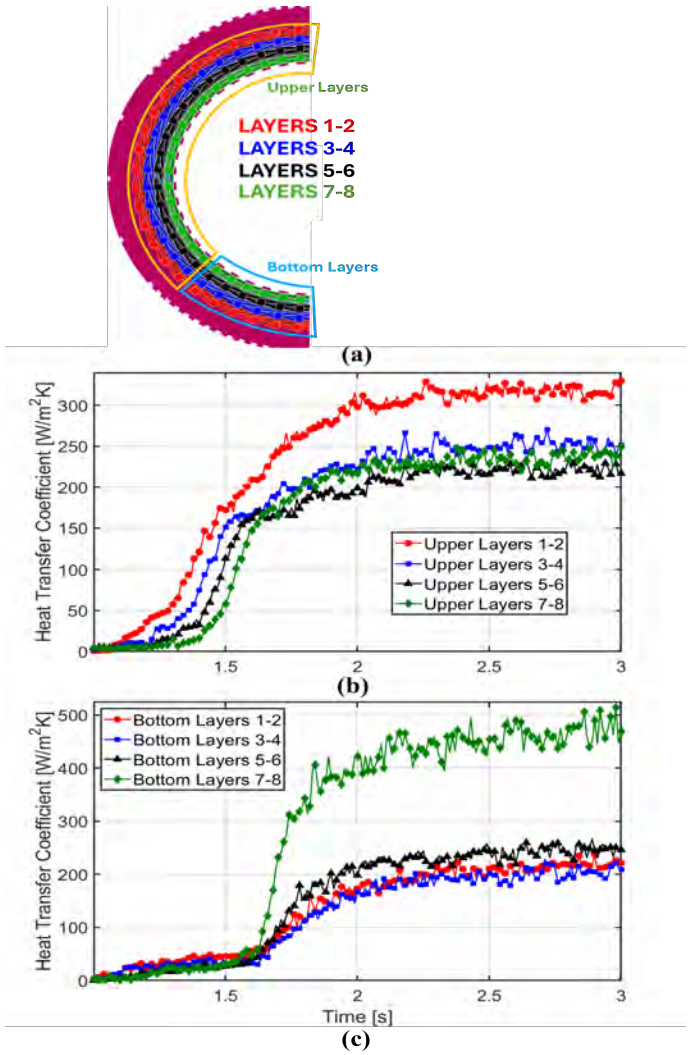

Figure 4.34: Average surface heat transfer coefficients calculated for different layers (a) of the end winding: (b) upper layers (b) bottom layers.

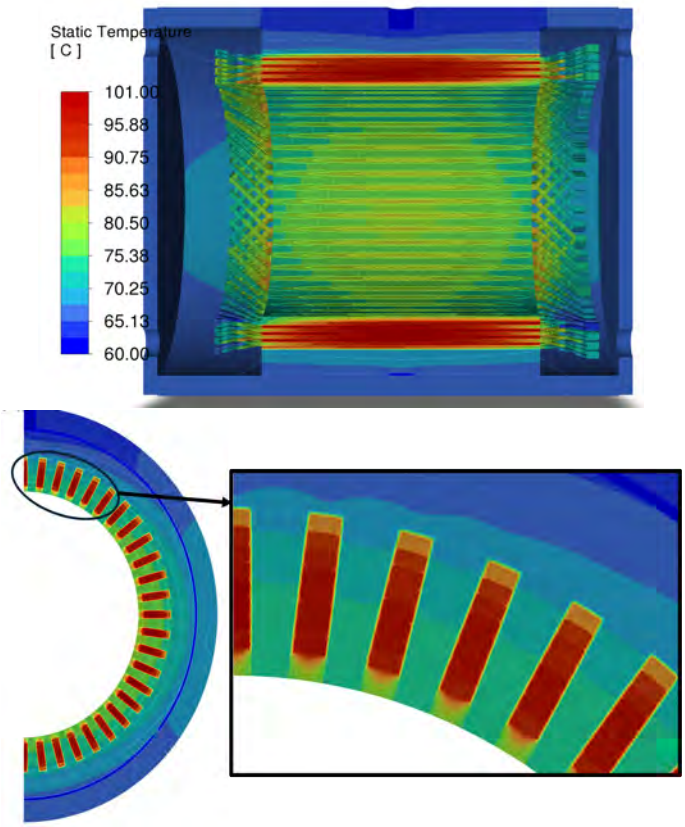

Figure 4.35: Cross-sectional view along the axial (top) and radial (bottom) direction showing the temperature contours resulting from the CHT complete model. The simulation reached steady-state with a stator current of 120 A and oil flow rate of 9 L/min.

comparing the end-winding temperatures to those of the conductors within the stator slots. The end-winding temperatures are significantly lower due to the beneficial effect of direct oil cooling, as opposed to the rest of the winding, where direct cooling is obstructed by multiple thermal resistances. These resistances are caused by the enamel insulation on the hairpin conductors, the slot liner, and air pockets within the stator slots. This disparity is further underscored by the substantial temperature gradient between the copper

conductors and the surrounding stator teeth and yoke. In the radial view (bottom), the focus shifts to the active part of the machine, where the temperature distribution of the conductors is prominently visible. The conductors within the stator slots exhibit the highest temperatures, predominantly in red (95–101°C), due to high current density and resistive losses. Moving outward from the conductors, the stator core displays a thermal gradient, transitioning from yellow (85°C) to green and blue (60–70°C) as heat is conducted outward and dissipated to the housing. The housing, consistently maintained in blue (60°C), demonstrates the efficiency of the cooling jacket surrounding the active region. Similarly, the surrounding areas, including the end plates and oil-cooled surfaces, are maintained at lower temperatures, closely aligned with the coolant temperature, represented by blue to green hues (60–75°C).

The simulation was conducted under a stator current of 120 A and an oil flow rate of 9 L/min, achieving steady-state conditions.

Experimental Verification

The experimental setup, depicted schematically in Fig. 4.36, is designed to evaluate the performance of the proposed cooling system against the simulation model. The stator, including the complete three-phase winding system and the housing, is incorporated into the test configuration. Two phases of the stator winding are connected in series and supplied with DC current using a power supply (SM 30-200) to emulate the stator copper losses.

The cooling circuit comprises two gear pumps, an oil reservoir, a heat exchanger, an oil filter, and power supplies for the pumps and field excitation. The first pump transfers oil from the reservoir to the cooling system inlet via a hose connected to the housing. The second pump draws oil through the oil filter and the heat exchanger. To thermally insulate the stator lamination from the surrounding environment, the stator and housing are enclosed within a plastic container and elevated on wooden supports.

During the thermal tests, the oil flow rate is maintained at 9.0 L/min, while the water flow rate used to cool the oil in the heat exchanger is set to 7.5 L/min. The water temperature is regulated at 60°C for the entire duration of the tests.

Multiple sensors are integrated into the setup: a pressure transducer is used to monitor the oil pressure drop across the cooling path, two Swissflow SF-800 flow rate sensors ensure accurate measurements of the oil and water flow rates, and temperature sensors are positioned at the inlet and outlet of both the heat exchanger and the stator inlet to verify that the target temperatures are achieved. Additionally, sixteen thermocouples are deployed to monitor temperatures at various locations on the end winding, as shown in in Fig. 4.37. The thermocouples indicated with an odd number and red label are positioned closed to the stator yoke, whereas the ones with even number and blue label are positioned closer to the airgap.

Experimental Results

Fig. 4.38 compares the measured and simulated pressure drop across the entire cooling system, as recorded by the pressure transducer located at the inlet of the hose mounted on the housing. The measurements are executed at room temperature of 21 °C and with no supplied power to the stator winding. The x-axis represents the flow rate, ranging from 4 to 11 L/min, while the y-axis

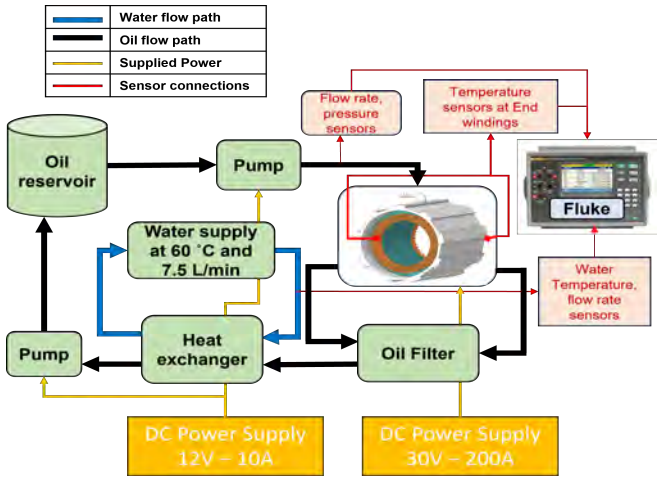

Figure 4.36: Schematic of the oil cooling setup used for experimental measurements.

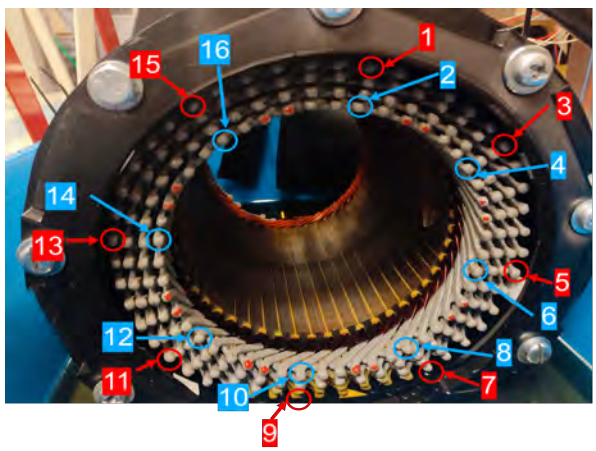

Figure 4.37: Sixteen thermocouples positioned at various locations on the end winding. Thermocouples labeled in red are located closer to the stator yoke, while those labeled in blue are positioned nearer to the airgap.

depicts the corresponding pressure drop, ranging from 4000 to 10000 Pa. The blue markers denote the measured pressure drop from experiments, while the red markers represent the simulated results from the cooling system simulations. Both datasets follow a similar trend, with the pressure drop increasing as the flow rate rises. The simulated values are consistently slightly higher than the measured ones across the range, likely due to model simplifications or potential uncertainties in the measurements and oil properties.

Fig. 4.39 compares the simulated and measured end-winding temperatures at 16 thermocouple positions, with the x-axis representing the sensor numbers (1 to 16) and the y-axis showing the temperature in degrees Celsius, ranging from 40°C to 160°C. The thermocouples are categorized into two groups based on their proximity: the red bands (odd numbers) indicate those positioned near the stator yoke, while the blue bands (even numbers) correspond to thermocouples located closer to the airgap.

The comparison evaluates the performance of the cooling system against the simulated results under two operating conditions: when the cooling system is active at a flow rate of 9 L/min and when the cooling system is deactivated. In both cases, the stator is supplied with a DC current of 130 A until

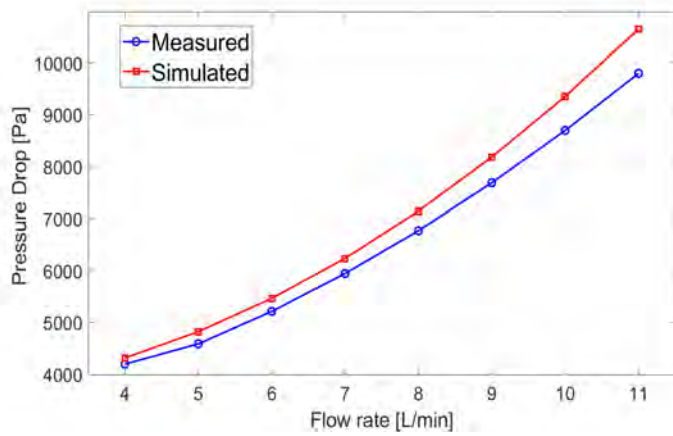

Figure 4.38: Comparison between the measured and simulated pressure drop of the whole cooling system for different values of inlet flow rates after reaching steady-state condition.

steady-state conditions are achieved. The solid curves for both the measured and simulated data show significantly lower temperatures compared to the dashed curves, which represent the condition with the cooling system turned off. The measured and simulated data exhibit similar trends in both scenarios, although minor discrepancies are observed when the cooling system is deactivated. In this case, the curves show a consistent trend with nearly constant offset in the discrepancies. This behavior can be attributed to the fact that, with the cooling system deactivated, the top and bottom layers of the hairpins heat up uniformly, reaching similar temperatures. In this condition, only the thermal resistances within the system influence the heat distribution, leading to the observed offset between the measured and simulated values. On the other hand, when the cooling system is activated, heat dissipation primarily depends primarily on the HTCs. As a result, the measured temperature is highly influenced by the sensor location and the extent of the oil impingement

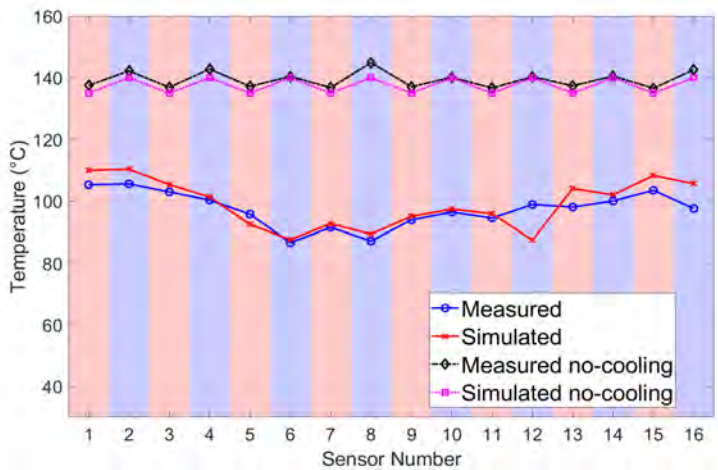

Figure 4.39: Comparison of simulated and measured end-winding temperatures under steady-state at various thermocouple positions. Red bands correspond to thermocouples located near the stator yoke, while blue bands represent thermocouples positioned closer to the airgap. The comparison includes two operating conditions: with the cooling system activated at a flow rate of 9 L/min (solid curves) and without the cooling system (dashed curves).

coverage. Despite this localized dependency, the end-winding temperatures remain relatively homogeneous due to the high thermal conductivity of copper, which efficiently distributes heat across the winding.

Stator Cooling Conclusion

This study presents a comprehensive cooling method for hairpin stators, integrating both indirect oil cooling via an oil jacket and direct oil impingement for the end windings. The proposed design was validated through experimental verification, demonstrating its effectiveness in maintaining temperatures below the thermal limits at a continuous current of 130 A RMS, corresponding to the machine maximum rated continuous operation. Additionally, a Conjugate Heat Transfer model was developed, utilizing a combination of the Finite Volume Method and the Moving Particles Simulation Method. The model predictions closely aligned with experimental data, accurately forecasting end-winding temperatures at various locations with a margin of error within 5–10%. This discrepancy is primarily attributed to factors such as the precise positioning of temperature sensors, the method of sensor attachment to the end windings, and the sensor relative position concerning the oil impingement coverage area.

CHAPTER 5

Conclusions and Future Work

This thesis has explored the design, analysis, and validation of high-power-density Electrically Excited Synchronous Machines for heavy-duty traction applications, addressing critical challenges in electromagnetic, mechanical, and thermal domains.

Chapter 2 provided a comprehensive comparison of EESMs and Permanent Magnet Synchronous Machines for truck drivetrains. Simulation results demonstrated the advantages of EESMs, including a higher power factor and better efficiency at high speeds and low torques region. The study highlighted EESM potential for reducing energy losses during driving cycles and improving overall performance in demanding vehicle drivetrains.

Chapter 3 focused on the design and experimental validation of a 60 kW concept EESM. This prototype was used to evaluate the mechanical integrity of a dovetail rotor design, addressing the challenges of conductor placement and stress under centrifugal forces. Electromagnetic performance and thermal behavior were analyzed in steady-state and transient conditions. The results confirmed the feasibility of the dovetail rotor structure and validated the machine electromagnetic models through experimental testing.

Chapter 4 expanded the study to a full-scale 200 kW EESM designed for

heavy-duty trucks. The chapter introduced advanced cooling solutions to address the significant heat generated in the rotor. Direct oil cooling and splash cooling strategies were extensively analyzed through simulations and experimental tests. The findings demonstrated effective temperature control across critical components, ensuring reliable operation under high-power conditions. These cooling methods minimized thermal hotspots and enhanced the machine operational limits, particularly during prolonged high-speed operation.

Overall, this thesis presents practical solutions to the key challenges of designing high-performance EESMs for traction applications. The findings establish EESMs as a competitive alternative to PMSMs, offering scalable designs with innovative mechanical and thermal solutions.

Future work could focus on the following areas:

- Further optimizing cooling strategies, enhancing rotor designs, and applying these methodologies to other industrial applications requiring high power density and reliability.
- Exploring additive manufacturing techniques for rotor conductor realization, with the aim of improving the fill factor and heat transfer efficiency.
- Experimentally verifying the rotor's dynamic behavior to validate both the electromagnetic and thermal analyses and their associated performance predictions.

References

[1] U.S. Environmental Protection Agency, *Fast facts on transportation greenhouse gas emissions*, 2023.

[2] European Environment Agency, *Transport and mobility*, Accessed: 2025-01-22, 2022.

[3] Statista Research Department, *Transportation emissions worldwide - statistics facts*, 2024.

[4] Our World in Data, *Cars, planes, trains: Where do co emissions from transport come from?* 2020.

[5] V. Balaram, "Rare earth elements: A review of applications, occurrence, exploration, analysis, recycling, and environmental impact," *Geoscience Frontiers*, vol. 10, no. 4, pp. 1285–1303, 2019, ISSN: 1674-9871.

[6] P. Zapp, A. Schreiber, J. Marx, and W. Kuckshinrichs, "Environmental impacts of rare earth production," *MRS Bulletin*, vol. 47, no. 4, pp. 1285–1303, 2022, ISSN: 3.

[7] L. Geslin, "Rare earth mining in myanmar: An extreme example of widespread destruction," *Le Monde*, May 2024.

[8] A. L. Steckel and I. Lange, *Rare earth elements pose environmental and economic risks for clean energy*, Podcast commentary, 2023.

[9] F. Times, "Canada opens new critical minerals hub in push to end china's dominance," *Financial Times*, 2024, Accessed: 2024-11-18.

[10] E. País, "Europa acelera en su carrera por diversificar los minerales críticos," *El País*, 2024, Accessed: 2024-11-18.

[11] W. S. Journal, "America's war machine runs on rare-earth magnets. china owns that market.," *Wall Street Journal*, 2024, Accessed: 2024-11-18.

[12] P.-K. Tse, "China's rare-earth industry," English, U.S. Geological Survey, Open-File Report 2011-1042, 2011, USGS Publications Warehouse.

[13] International Energy Agency (IEA), "The role of critical minerals in clean energy transitions," IEA, Paris, 2021, Licence: CC BY 4.0.

[14] US Geological Survey, *Distribution of rare earths production worldwide as of 2023, by country [graph]*, [Online; accessed November 18, 2024], Jan. 2024.

[15] Y. Shen, R. Moomy, and R. G. Eggert, "China's public policies toward rare earths, 1975–2018," *Mineral Economics*, vol. 33, no. 1, pp. 127–151, 2020, ISSN: 2191-2211.

[16] IEEE Spectrum, "General motors and stellantis partner with niron magnetics on rare earth-free permanent magnets," Nov. 2023, Accessed: 2024-11-18.

[17] F. Lambert, "Tesla is going back to ev motors with no rare earth elements," *Electrek*, Mar. 2023, Accessed: 2024-11-18.

[18] Electric Motor Engineering, "Synchronous reluctance motor: A rare earth-free solution for electric vehicles," 2023, Accessed: 2024-11-18.

[19] J. Doe, "Tesla's electric motor revolution," *Automotive Engineering*, vol. 45, no. 3, pp. 123–130, 2023.

[20] J. Smith, "Bmw's transition to electric powertrains," *Journal of Electric Vehicles*, vol. 12, no. 2, pp. 98–105, 2024.

[21] M. Brown, "General motors' electric motor strategy," *Electric Vehicle Technology*, vol. 8, no. 1, pp. 45–52, 2023.

[22] E. White, "Mercedes-benz's adoption of axial-flux motors," *Advanced Automotive Technology*, vol. 10, no. 4, pp. 200–207, 2024.

[23] D. Green, "Rivian's electric motor innovations," *Electric Mobility Review*, vol. 5, no. 3, pp. 150–157, 2023.

[24] S. Black, "Ford's electric motor development," *Automotive Powertrain Journal*, vol. 9, no. 2, pp. 75–82, 2024.

[25] R. Blue, "Hyundai's electric vehicle motor technology," *Journal of Sustainable Transportation*, vol. 7, no. 1, pp. 30–37, 2023.

[26] L. Red, "Nissan's electric motor advancements," *Electric Vehicle Research*, vol. 6, no. 4, pp. 110–117, 2024.

[27] P. Yellow, "Audi's electric motor technologies," *Automotive Innovation*, vol. 11, no. 2, pp. 60–67, 2023.

[28] N. Purple, "Jaguar's electric motor implementation," *Journal of Electric Mobility*, vol. 8, no. 3, pp. 140–147, 2024.

[29] K. Orange, "Volkswagen's electric motor strategy," *Electric Vehicle Systems*, vol. 9, no. 1, pp. 50–57, 2023.

[30] O. Pink, "Volvo's electric motor development," *Sustainable Automotive Engineering*, vol. 6, no. 2, pp. 90–97, 2024.

[31] P. AG, "Technical feature: The porsche taycan's electric powertrain," *Porsche Newsroom*, 2021, Accessed: 2024-11-18.

[32] L. Motors, "Lucid motors' proprietary electric drivetrain technology powers record-setting performance and industry-leading efficiency in the lucid air," 2020, Accessed: 2024-11-18.

[33] Team-BHP, "2024 byd seal: Our observations after a day of driving," 2024, Accessed: 2024-11-18.

[34] L. S. Francisco. "Lamborghini revuelto: The first super sports v12 hybrid hpev." Accessed: 2024-11-18. (2024), [Online]. Available: `https://www.lamborghinisf.com/revuelto.htm?srsltid=AfmBOop7C_dWhSgnyXuYsB2y0gXx9Ez5IRm_BASoZPwnipSLKQfeYte5`.

[35] Y. Ltd. "Ferrari selects yasa axial-flux motor for sf90 stradale." Accessed: 2024-11-18. (2019), [Online]. Available: `https://yasa.com/news/ferrari-selects-yasa-for-sf90-stradale/`.

[36] HotCars. "Incredible facts gearheads should know about the new mclaren artura." Accessed: 2024-11-18. (2023), [Online]. Available: `https://www.hotcars.com/incredible-facts-gearheads-should-know-about-the-new-mclaren-artura/`.

[37] H. Stenvall, *Driving resistance analysis of long haulage trucks at Volvo: Test methods evaluation*. Chalmers University of Technology, 2010.

[38] E. A. Grunditz, *Design and assessment of battery electric vehicle powertrain, with respect to performance, energy consumption and electric motor thermal capability*. Chalmers Tekniska Hogskola (Sweden), 2016.

[39] K. Ma, M. Liserre, F. Blaabjerg, and T. Kerekes, "Thermal loading and lifetime estimation for power device considering mission profiles in wind power converter," *IEEE Transactions on Power Electronics*, vol. 30, no. 2, pp. 590–602, 2015.

[40] J. Tang and Y. Liu, "Comparison of copper loss minimization and field current minimization for electrically excited synchronous motor in mild hybrid drives," in *2017 19th European Conference on Power Electronics and Applications (EPE'17 ECCE Europe)*, 2017, P.1–P.10.

[41] J. Tang, "Synchronous machines with high-frequency brushless excitation for vehicle applications," Ph.D. dissertation, Chalmers University of Technology, Sweden, 2019.

[42] J. Tang and Y. Liu, "Design of electrically excited synchronous machines to achieve unity power factor in field weakening for long-haul electric trucks," in *2020 International Conference on Electrical Machines (ICEM)*, vol. 1, 2020, pp. 422–428.

[43] L. Boscaglia, A. Boglietti, S. Nategh, F. Bonsanto, and C. Scema, "Numerically based reduced-order thermal modeling of traction motors," *IEEE Transactions on Industry Applications*, vol. 57, no. 4, pp. 4118–4129, 2021.

[44] D. Staton, A. Boglietti, and A. Cavagnino, "Solving the more difficult aspects of electric motor thermal analysis in small and medium size industrial induction motors," *IEEE Transactions on Energy Conversion*, vol. 20, no. 3, pp. 620–628, 2005.

[45] T. Davin, J. Pellé, S. Harmand, and R. Yu, "Experimental study of oil cooling systems for electric motors," *Applied Thermal Engineering*, vol. 75, pp. 1–13, 2015.

[46] B. Jiang, X. Huang, Y. Liu, and S. Nategh, "Accelerated destructive experiment design of motor stator winding insulation systems," in *2021 IEEE Workshop on Electrical Machines Design, Control and Diagnosis (WEMDCD)*, 2021, pp. 225–230.

[47] H. Toliyat and G. Kliman, *Handbook of Electric Motors*. Boca Raton, FL: CRC Press, 2004.

[48] S. Sugimoto and D. Kori, "Cooling performance and loss evaluation for water- and oil-cooled without pump for oil," in *2018 XIII International Conference on Electrical Machines (ICEM)*, 2018, pp. 1136–1141.

[49] L. Boscaglia, F. Bonsanto, A. Boglietti, S. Nategh, and C. Scema, "Conjugate heat transfer and cfd modeling of self-ventilated traction motors," in *2019 IEEE Energy Conversion Congress and Exposition (ECCE)*, 2019, pp. 3103–3109.

[50] L. Boscaglia, A. Boglietti, S. Nategh, F. Bonsanto, and C. Scema, "Numerically based reduced-order thermal modeling of traction motors," *IEEE Transactions on Industry Applications*, vol. 57, no. 4, pp. 4118–4129, 2021.

[51] G. Venturini, G. Volpe, and M. Popescu, "Slot water jacket cooling system for traction electrical machines with hairpin windings: Analysis and comparison," in *2021 IEEE International Electric Machines and Drives Conference (IEMDC)*, 2021, pp. 1–6.

[52] L. Ye, F. Tao, W. Xuhui, and L. Qi, "Experimental investigation of heat transfer and resistance characteristics of the motor water jackets," in *2014 IEEE Conference and Expo Transportation Electrification Asia-Pacific (ITEC Asia-Pacific)*, 2014, pp. 1–3.

[53] L. Ye, F. Tao, L. Qi, and W. Xuhui, "Experimental investigation on heat transfer of directly-oil-cooled permanent magnet motor," in *2016 19th International Conference on Electrical Machines and Systems (ICEMS)*, 2016, pp. 1–4.

[54] K.-H. Lee, H.-R. Cha, and Y.-B. Kim, "Development of an interior permanent magnet motor through rotor cooling for electric vehicles," *Applied Thermal Engineering*, vol. 95, pp. 348–356, 2016.

[55] Z. ZI-CHAO, S. QIANG, and B. AHMED, "Innovative design of the cooling topologies for electric vehicle motors," *IOP Conference Series: Materials Science and Engineering*, vol. 533, no. 1, p. 012 021, May 2019.

[56] F. Wirth, T. Kirgör, J. Hofmann, and J. Fleischer, "Fe-based simulation of hairpin shaping processes for traction drives," in *2018 8th International Electric Drives Production Conference (EDPC)*, 2018, pp. 1–5.

[57] R. Pechanek and L. Bouzek, "Analyzing of two types water cooling electric motors using computational fluid dynamics," in *15th International Power Electronics and Motion Control Conference and Exposition (EPE-PEMC 2012 ECCE Europe)*, Sep. 2012, LS2e.4–1, ISBN: 978-1-4673-1970-6.

[58] F. R. Menter, "Zonal two equation k-ω turbulence models for aerodynamic flows," *AIAA Journal*, vol. 93, pp. 90–96, 1993.

[59] S. Koshizuka, K. Shibata, M. Kondo, and T. Matsunaga, *Moving Particle Semi-implicit Method: A Meshfree Particle Method for Fluid Dynamics*. Elsevier Science, 2018, ISBN: 9780128127797.

[60] L. Boscaglia, Y. Liu, H. Avsar, J. Tang, and M. Galbiati, "Convective heat transfer coefficients and mechanical loss evaluation of oil splashing in direct cooled electrically excited hairpin motors," in *2022 International Conference on Electrical Machines (ICEM)*, 2022, pp. 496–503.

[61] D. Staton, A. Boglietti, and A. Cavagnino, "Solving the more difficult aspects of electric motor thermal analysis in small and medium size industrial induction motors," *IEEE Transactions on Energy Conversion*, vol. 20, no. 3, pp. 620–628, 2005.